Bacterial motion in confinement

Tommaso Pietrangeli

Université Claude Bernard Lyon 1

THESE de DOCTORAT DE

L'UNIVERSITE CLAUDE BERNARD LYON 1

Ecole Doctorale N°52

Ecole Doctorale de Physique et Astrophysique

Discipline : **Physique**

Soutenue publiquement le 12/12/2024, par :

Tommaso PIETRANGELI

Bacterial Motion in Confinement

Devant le jury composé de :

Peyla, Philippe	Professeur - Université Grenoble Alpes	Président
Taute, Katja	Professeure - Université Leipzig	Rapporteure
Peruani, Fernando	Professeur - CY Cergy Paris Université	Rapporteur
Delanoë-Ayari, Hélène	Professeure - Institut Lumière Matière	Examinatrice
Cottin-Bizonne, Cécile	Professeure - Institut Lumière Matière	Directrice de thèse
Detcheverry, François	Professeur - Institut Lumière Matière	Co-directeur de thèse

N° National de Thèse : XXX

THESIS

en vue de l'obtention du grade de

Docteur de l'Université Claude Bernard Lyon 1

Discipline : **Physics**

Institut Lumière Matière

Equipe Liquides et Interfaces

École Doctorale n°52 PHAST

Présentée et soutenue publiquement le 12/12/2024
par **Tommaso Pietrangeli**

Bacterial Motion in Confinement:

Optimal Strategies, Universal Dispersal and Magnetotactic Bacteria

---

PIs : Cécile Cottin-Bizonne, Christophe Ybert, François Detcheverry

Devant la commission d'examen formée de :

Mme.	Cécile Cottin-Bizonne	*Institut Lumière Matière*	Directrice
M.	François Detcheverry	*Institut Lumière Matière*	Co-Directeur
Mme.	Katja Taute	*Leipzig University*	Rapportrice
M.	Fernando Peruani	*CY Cergy Paris Université*	Rapporteur
M.	Philippe Peyla	*Université Grenoble Alpes*	Examinateur
Mme.	Hélène Delanoe-Ayari	*Institut Lumière Matière*	Examinatrice

Institut Lumière Matière
16, rue Enrico Fermi
69622 Villeurbanne CEDEX (FR)

École doctorale PHAST
4, rue Enrico Fermi
69622 Villeurbanne CEDEX (FR)

Acknowledgements

I would like to thank everyone who takes the time to read about my work, with special thanks to Professors Katja Taute and Fernando Peruani for accepting to review and evaluate my thesis as *rapporteurs*.

A heartfelt thank you to my supervisors, Cécile, François, and Christophe. Their guidance and support over the past three years, both scientifically and personally, made this thesis possible, but also helped me enjoy the journey and overcome many challenges along the way.

To my colleagues[1], who helped me through the tough days when nothing was working; to all the people in my life[2], old and new, whose presence and support mean everything to me; and to my family[3], who has always supported me and taught me how to think critically—I am truly grateful.

Finally, I want to thank the EU and the academic community for the amazing opportunities that were given to me. I have met, and can now call friends, people from all over the world, which has taught me how to see things from beyond the culture I grew up in. While my future in academia remains uncertain, these new perspectives will stay with me as I navigate whatever paths lie ahead.

Grazie!

This project has received funding from the European Union's Horizon 2020 research and innovation programme under the Marie Skłodowska-Curie grant agreement No 955910.

[1] Valentin, Changwoo, Mojahed, Mohammed, Julie, Riccardo, Luc, and everyone at iLM and Phymot.
[2] Balle, Giuffri, Francesco, Robin, Cecilie, Flavia, at least three different Giulia, and so many more.
[3] Mom and Dad, Zia Bri and Mauro, Andrea and Bernadette, Otto, the new baby, and everybody else.

Contents

Introduction

Bacteria are among the most diverse and widespread life forms on Earth, inhabiting environmental niches that range from the ocean depths to the human body [1]. Their motility, or ability to move, is crucial for survival, enabling them to navigate complex surroundings, locate nutrients, and avoid threats [2]. Understanding bacterial motility is essential in fields such as microbial ecology, where it influences population dynamics in diverse environments [3]; medicine, as it plays a role in the spread of infections [4]; or bio-inspired technologies, enabling the design of microrobots for targeted drug delivery [5]. Over the past fifty years, experimental and theoretical approaches have significantly advanced knowledge of bacterial motility [6]. Nevertheless, challenges remain, primarily due to the diversity of bacterial species, the variety of environments they inhabit, and the complexity of their behaviors.

A major research focus has been predicting transport properties, such as bacterial dispersal. Stochastic models of active matter, including run-and-tumble particles and active Brownian particles, have played a key role in this context, finding broad applications for both biological and artificial microswimmers [7,8]. Bacterial dispersal in natural environments, such as soil, sediments, and porous rocks, presents additional challenges [9, 10]. These environments can involve diverse forms of confinement, which result in complex dynamics, such as trapping, hopping, or sliding [11–13]. While stochastic models have been increasingly applied to these systems [14–19], a unified framework capable of addressing the wide variety of environmental and motion parameters is still lacking. Moreover, an interest topic in the study of confined motion is the question of optimality: "What is the best strategy for maximizing exploration within a specific confined environment?". Addressing this question is important for understanding biological swimming strategies and designing artificial systems that require efficient navigation. Although promising trends have been identified [20–22], many questions remain.

Another aspect of bacterial motility involves driven or guided motion, where external fields influence movement of the microorganism, with applications in areas such as targeted drug delivery and environmental sensing [23]. In this context, magnetotactic bacteria—microorganisms that change their direction of motion in response to magnetic fields [24]—are an ideal biological system to study this type of guided motility. Several potential applications are being explored in relation to this family of bacteria, particularly

in medical fields involving cancer treatment [25]. However, research on their motility is still limited to a few species [26], and understanding how they move under various conditions, especially near solid interfaces or in confined environments, is a new research direction that has recently attracted attention [27].

Scope of the Thesis The work presented in the thesis includes theoretical, numerical, and experimental approaches. First, it combines simulations and theory to investigate the transport properties of confined bacterial motion, with the primary objective of developing predictive models for dispersal that can account for a broad range of motion and environmental parameters. The study also addresses optimality, to determine which motion strategies can maximise dispersal. On the experimental side instead, the work addresses the limited knowledge across different species of Magnetotactic Bacteria, by investigating the motility of a novel strain with promising potential for further studies.

Structure of the Thesis The thesis is organized into four main chapters:

- The first chapter, *Background and State of the Art*, summarizes foundational studies on bacterial motility, introducing key concepts from literature and identifying gaps that will be addressed in the following chapters.
- The second chapter, *Optimal Run-and-Tumble in Slit-like Confinement*, presents theoretical and simulation-based studies of run-and-tumble particles moving between two parallel walls. This chapter develops and validates a model to predict bacterial dispersion in this simple geometry, while also addressing the question of optimal motion strategies for exploring slit-like environments.
- The third chapter, *Universal Dispersal of Motile Microorganisms in Porous Media*, first explores bacterial motion in porous environments through simulations, identifying a universal dependence of dispersal. Then it rationalises the numerical results with a model linking dispersal to Cauchy universality. The model accurately predicts dispersal across a wide range of environments and motion parameters, and provide insight on previous results in literature.
- The fourth chapter, *Motion Under Constraint: Novel Magnetotactic Bacteria*, presents experimental work. It characterizes the magnetic response of a novel strain of Magnetotactic Bacteria and presents preliminary findings on its motion near solid interfaces, laying the groundwork for future research on this topic.

Overall, the work presented in this thesis advances the understanding of bacterial motility, with a specific focus on dispersal in confined settings, optimality, and the case of magnetotactic bacteria.

CHAPTER 1

Background and State of the Art

Contents of this Chapter

This first chapter will establish the foundation for understanding the physics of bacterial motility. It starts with a thorough introduction to bacterial motion, explaining the essential physical concepts relevant to this thesis. Next, the chapter will review existing literature, focusing on bacterial behavior in complex and confined environments. By summarizing the state of the art, it aims to identify the key findings and the limitations in current research. Lastly, it will define the main objectives of the thesis.

1.1 Bacteria and the Physics of Motility

Bacteria are among the most ubiquitous forms of life on Earth, inhabiting diverse environments such as soil [9], lake and sea sediments [1, 28], porous rocks [10], and marshes [29].

They are also found in extreme habitats, such as pore waters in gold mines [30], the guts of deep-sea marine animals [31], and fluid bubbles trapped in ice for thousands of years [32]. The remarkable ability of bacteria to colonize and survive in these environments is the result of four billion years of evolution, occurring at a faster pace than in multicellular organisms [33]. This evolution process has resulted in bacterial species with extraordinary abilities. For example, *Acidithiobacillus ferrooxidans* thrives in acid lakes contaminated by mining waste, enduring pH levels ranging from 0 to 12.5 [34]. *Deinococcus radiodurans*, initially discovered in spoiled canned meats, is instead tolerant to strong radiation and vacuum, and it is currently used in astrobiology to test the limits of survival in space [35]. In-between these very extreme examples, lies a vast diversity of largely unknown bacterial species that occupy all available environmental niches.

Motility is a key characteristic of bacteria, with about 80% of known species capable of movement [36]. This ability provides numerous evolutionary advantages, such as improved nutrient acquisition and escape from hostile environments [37]. The mechanisms behind bacterial motility involve complex interactions between biological and physical elements. Physics, along with other sciences, has been crucial in unraveling these intricate processes. From early advances in microscopy and hydrodynamics in the mid-20th century [38, 39], to the development of mathematical models in the following decades [40], foundational research has significantly advanced our understanding of bacterial motility. In the past decades specifically, physics studies on bacterial motility has surged, driven by the ever-growing field of active matter [7, 41, 42]. The multi-scale and interdisciplinary nature of these studies creates a vast and diverse field, all aimed at understanding the complexity of bacterial motion.

1.1.1 The Fundamentals of Bacterial Motion

Foundational studies in the physics of bacterial motility have primarily focused on the motion of *Escherichia coli*, a gut bacterium that has played a central role in the history of bacteriological research [43]. The seminal work initiated by Brown and Berg in the 1970s [40, 44], along with all subsequent research up to the present, has made *E. coli* the most thoroughly understood example of bacterial motility.

The Paradigmatic Run-and-Tumble of *E. coli* *E. coli* cells are rod-shaped, typically measuring $0.5 - 1$ µm in diameter and $2 - 4$ µm in length [46]. They move using flagella: long and thin helical filaments attached to the exterior of the cell body. Flagella are driven by motor proteins, nano-scale engines embedded in the cell wall, capable of rotating either clockwise or counterclockwise with nearly perfect energy efficiency [47]. *E. coli* are *peritrichous*, meaning they possess multiple flagella and motors, and motion occurs by alternating motor states. Simultaneous counter-clockwise rotation causes the flagella to bundle and propel the cell forward in a quasi-straight ballistic trajectory, at velocities that range between $20 - 50$ µm s^{-1} [45]. A clockwise rotation of one or more flagella instead disperses the bundle, causing the bacterium to change the orientation of the cell body. The resulting pattern of motion takes the name of *run-and-tumble*, and can be seen in the real tracks of *E. coli* shown in Fig. 1.1A. The strategy consists of alternating persistent motion with sudden changes in direction. Despite the complex biological

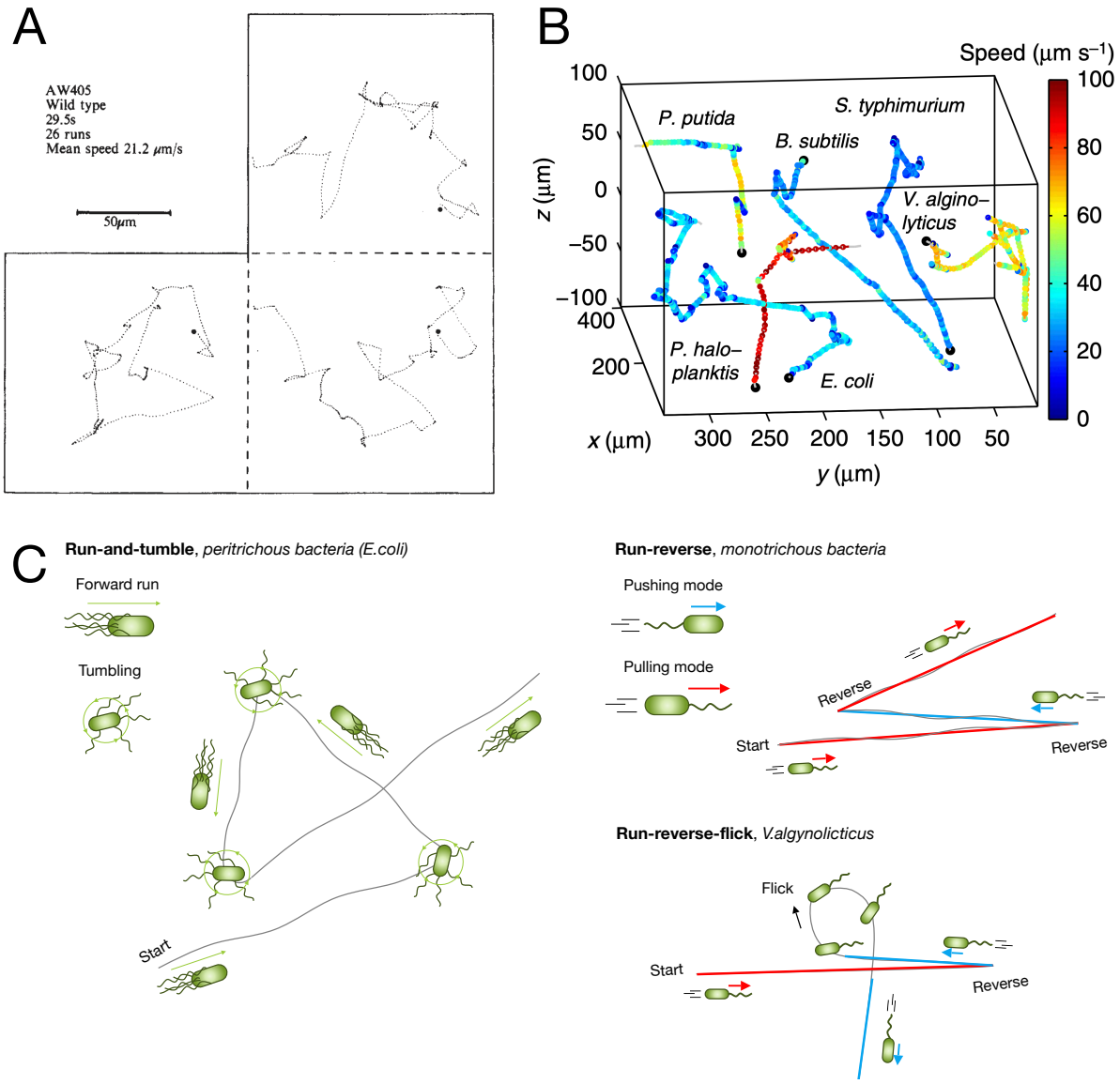

Figure 1.1: **Swimming patterns of bacteria.** A) Two-dimensional projection of *E. coli* tracks published by Brown and Berg in 1972, showing an alternation of ballistic "runs" and localised re-orientations [38]. B) 3D tracks of various bacterial species characterised by persistent ballistic motion and re-orientation events, adapted from Taute *et. al* [45]. C) Schematics of different bacterial swimming patterns.

and hydrodynamic factors influencing its movement, the overall motion of *E. coli* can be described by dynamics similar to those seen in various types of random walks. This observation is, and has been, a central point of research that delves with bacterial transport, as it establishes a link between bacterial movement and purely theoretical stochastic processes [6].

Repertoire of Swimming Patterns While research on *E. coli* has successfully connected various aspects of motion at multiple scales, from swimming properties to motility patterns, such a comprehensive picture is not yet available for most other bacteria. However, flagella and motor proteins are conserved genetic traits among a vast diversity of species [48, 49]. This conservation is evident as many motile bacteria exhibit *run-and-turn*-like swimming patterns [50–53], as seen in the experimental tracks in Fig. 1.1B. Additionally, swimming patterns are not limited to run-and-tumble; instead, they can exhibit different variations. A simple example is the *run-stop* pattern of *Rhodobacter sphaeroides*, a bacterium with a single unidirectional motor that periodically pauses [54]. During each motor stop, the flagellum transitions from a helical to a coiled state, causing the cell to actively reorient itself [55]. Another instance is the case of marine bacteria which possess only one flagellum. These *monotrichous* bacteria lack the ability to tumble, but can still reverse their flagellar motor, which can propel the cell body either forward or backward [56, 57]. This mechanism results in a swimming pattern known as *run-reverse*, which alternates between pushing and pulling modes, featuring sharp reversals of the direction of motion [50, 51]. Furthermore, a distinct swimming pattern is also exhibited by *V. alginolyticus*, a marine bacteria that employs a dual reorientation mechanism. This bacterium combines *reverse* events, similar to those of marine bacteria, with *tumble*-like orientation changes, resulting in a *bimodal* swimming strategy termed *run-reverse-flick* [58, 59].

All the presented examples of bacterial motility rely on flagellar propulsion, resulting in random-walk-like trajectories. Different swimming patterns emerge, each with specific variations, as summarized schematically in Fig. 1.1C. The central focus of this thesis will be on these aspects typical of swimming bacteria. However, it is important to acknowledge the existence of various other kinds of bacterial movement, such as twitching or gliding on surfaces [2].

1.1.2 Motility Responses to External Cues

The previous section presented bacterial motion in the absence of external interactions. However, bacteria have evolved various internal mechanisms to alter their movement patterns in response to their environments. The ability to sense and move in response to environmental cues is generically known as *taxis*.

Active and "Biological" Taxis An early example of motility response is *chemotaxis*, observed first in the motion of *E. coli* in the 1970s [38, 60]. *E. coli* that navigate through a concentration gradient of nutrients can detect if they are moving towards higher concentration zones. In response, the bacteria alter their motility pattern, biasing their random walk: runs become longer when moving in favorable directions, resulting in a drift up

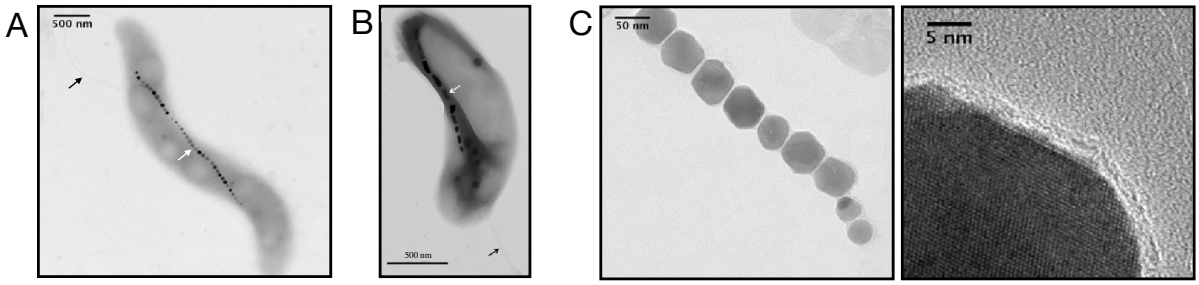

Figure 1.2: **Magnetotactic bacteria and magnetosomes**. Transmission electron microscopy images. A) AMB-1 strain [72]. B) HSMV-1 strain [73]. White arrows indicate the *magnetosome* chain, black arrows point at flagella. C) Progressive zoom on a *magnetosomes* chain [72].

the nutrient gradient [61]. The ability to sense and react to environmental signals is crucial for bacterial survival and adaptation, leading to extensive research in this area. This research field encompasses aspects such as spatial and temporal sensing [62], signal transduction pathways [63], and motility pattern modulation [64]. In this line of research, various forms of *taxis* have been identified and characterized across bacterial species. In the case of *aerotaxis*—a motility response to oxygen concentrations—the response can be positive, where bacteria move towards higher oxygen concentrations, or negative, where they move towards lower oxygen concentrations [65]. Furthermore, some bacteria exhibit *microaerotaxis*, meaning their motility allows them to seek and accumulate at specific oxygen levels [66]. Lastly, *taxis*-like motility adaptations can be observed in response to other types of signals, such as mechanical stimuli [67], light [68], or pH levels [69].

Physical Drivers of Motility: Gravitaxis and Magnetotaxis The previous examples of taxis are "biological", in the sense that they involve an active internal response that induces a motility skewing upon specific cues. Other forms of taxis are "physical", for which the stochastic aspects of swimming are skewed by a physical passive response to an external "potential". For instance, bottom-heavy swimmers align and swim against gravity thanks to localized high-density regions within the cell body, passively performing *gravitaxis* [70]. Another example, particularly relevant to this thesis, is *magnetotaxis*. It is a motility response characteristic of magnetotactic bacteria (MTB) [71], a diverse family of motile bacteria known for their unique ability to orient and navigate along geological magnetic field lines. This ability results from structures within their cell bodies called *magnetosomes*: nanometric and ferromagnetic crystals with remarkably precise geometries [72]. *Magnetosomes* are aligned forming a chain that is fixed within the cell body, as shown in Fig. 1.2. These structures are responsible for coupling the flagellar propulsion with a magnetic alignment effect, resulting in a unique type of navigation among bacterial species. Moreover, most MTB also perform *aerotaxis*, combining both passive and active taxis in the same microorganism [24]. The coupling of motility with different types of responses is a fascinating aspect of their motion, as the evolutionary advantages of the magnetosomes chain are not fully understood. Additionally, ongoing studies have documented a remarkable diversity in the family of MTB, encompassing species with radically different morphologies and ecological niches [26, 73].

1.2 Stochastic Active Particles

This section transitions from real-world bacteria to the theory of active matter: systems out of equilibrium that consume energy to move [74]. Specifically, the emphasis is on active models used in physics to study bacterial motion, particularly Run-and-Tumble Particles and Active Brownian Particles. The goal is to provide a theoretical foundation for understanding the physics of self-propelled agents, explore their connection to microswimmer dynamics, and discuss their fundamental transport properties, which play a central role for the work presented in this thesis.

Bottom-Up Description of Motion A complete and natural model of bacterial transport should originate from a description of the microscopic underlying mechanisms of motility. This relies on connecting motion properties to complex features at the cellular and molecular levels. Along these lines, studies have characterised the hydrodynamical interactions of rotating flagella with the surrounding fluid [6, 75], progressively building up to comprehensive models that include the cell body [75], self-propulsion [76], and biological responses like tumbling events [77]. More coarse-grained approaches have considered simplified cell structures or effective hydrodynamic interactions [78, 79]. Overall, these hydrodynamics-based approaches can replicate various levels of real cell behaviors and have been successfully employed to address issues such as interactions with solid surfaces [80,81] or coupling with external flow fields [13]. However, these methods pose significant challenges due to their highly nonlinear and multiscale complexity. These limitations generally require computationally intensive numerical solutions, which are not suited for characterizing properties like long-term transport. Additionally, these approaches rely on detailed knowledge of biological characteristics, thus quickly becoming specific to the case under study.

Higher-Level Modelling: Stochastic Approaches Many issues relevant to bacterial transport can be addressed at a higher-level description, where only the key features of motion are considered. As suggested by the examples in Section 1.1, bacteria can be seen as motile objects whose trajectories result from a combination of self-propulsion, stochastic reorientation, and responses to external cues. This perspective has led to modeling motility using purely stochastic models. These methods can disregard both hydrodynamics and biological processes by employing specific assumptions, simplifying motility into tailored stochastic processes. Although this approach moves away from the exact dynamics of real agents, it makes the problem mathematically manageable and, in some cases, fully solvable [82]. The inherently theoretical nature of these methods results in general models where only quantitative parameters are specific to the system. Consequently, the resulting models can encompass different bacterial species and find applications beyond bacterial motility [67, 83–86].

The field of stochastic active matter, in application to bacterial motility, is central to the work presented in this thesis. The remaining part of this section will introduce the key frameworks of the domain.

1.2.1 Active Brownian Particles

Active Brownian Particles (ABPs) are a pivotal model of active matter theory, serving as a foundational frameworks to describe self-propelled particles, including biological agents like bacteria [87] or artificial swimmers like Janus particles [88]. ABPs are, in origins, the active extension of the concept of passive Brownian particles: inert particles that move solely due to thermal fluctuations. Unlike the passive case, Active Brownian Particles (ABPs) exhibit self-propulsion and are therefore oriented. A key feature of the model is that the particle's orientation changes over time due to diffusion.

Dynamics The dynamics of ABPs are described by Langevin equations, which account for both deterministic propulsion forces and random thermal fluctuations. In two dimensions, the dynamics of an ABP's position $\mathbf{r}(t)$ and orientation $\theta(t)$ can be written as two coupled equations:

$$\frac{d\mathbf{r}(t)}{dt} = v_0\mathbf{e}(t) + \sqrt{2D_\mathrm{t}}\eta(t)\,, \quad \frac{d\theta(t)}{dt} = \sqrt{2D_\mathrm{r}}\xi(t)\,, \tag{1.1}$$

where v_o is the propulsion speed, $\mathbf{e}(t) = (\cos\theta(t), \sin\theta(t))$ is an orientation versor, D_t and D_r the translational and rotational diffusion coefficients, and $\xi(t)$ and $\eta(t)$ are Gaussian white noise terms.
These equations of motions contain various implications. First, inertial terms are neglected. This overdamped limit is typical for systems at low Reynolds numbers, such as microswimmers and bacteria, where viscous forces dominate over inertial forces [39]. Second, they assume that self-propulsion results in a constant velocity level, another typical assumption in applications to bacteria [7]. Third, the rotational diffusion D_r is linked to complex interaction related to propulsion mechanisms and biological processes, rather than solely temperature. Nonetheless, the white noise model of fluctuations has been succesfully applied to microswimmer behaviors *via* the introduction of effective temperatures that represent complex sources of noise [87]. Lastly, a relevant quantity to introduce is the Péclet number: a dimensionless parameter that characterizes the relative importance of advective to diffusive transports. For ABPs, and all models introduced hereafter, the Péclet number is defined as:

$$Pe \equiv \frac{v_\mathrm{o}L}{D_\mathrm{t}}\,, \tag{1.2}$$

where L is a characteristic length scale of the system, such as the particle size. A high Péclet number indicates that advective transport (driven by self-propulsion) dominates over diffusive transport (thermal motion). The high Pe limit is a typical scenario for active systems like bacteria, resulting in models that neglect thermal diffusive transport. This limit will be considered in all following considerations.

1.2.2 The Run-and-Tumble Particle

While pivotal for the physics of active systems, ABPs are characterized by an orientation randomization that occurs over time through a constant diffusive rotation. This differs from the features pointed out for many bacteria, where strong re-orientations are localised and occur at discrete times. To better capture these distinct behaviors, a second active model is introduced: the Run-and-Tumble Particle (RTP) model.

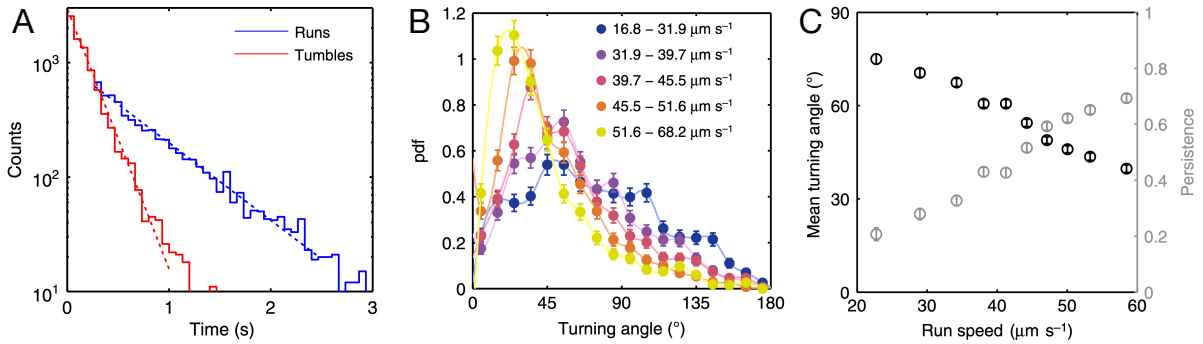

Figure 1.3: **Run-and-Tumble properties of *E. coli*.** Experimental measures adapted from Taute *et al.* [45]. A) Distribution of run and tumble times, with exponential fits (dotted). B) Distribution of turning angles for different run speeds. C) Mean turning angle and mean cosine of turning angle (persistence), as a function of different run speeds.

Definition of the Model The basic definition of RTP consists of a point-like active particle, characterized by constant velocity, persistent motion and stochastic re-orientations. This model is defined by the following parameter space: the propulsion velocity v_o, the time distribution of run times $\psi(t)$ and tumble duration $\Psi(t)$, and the distribution of turning angles due to tumbling $h(\theta)$. These parameters can be tailored to reproduce many different types of motion.

An *E. coli*-based Formulation In applications of RTPs to bacteria, the model has found extensive use in reproducing the persistent random walks of *E. coli*. The adaptation of the RTP framework to the case of *E. coli* can leverage the many experimental results for these bacteria available in literature. Specifically, modelling can rely on key statistical distributions sampled from experimental tracks, which are reported in Fig 1.3. Starting from the distribution of run and tumble times of real cells, shown in Fig. 1.3A, two considerations can be made. First, both distributions follow an exponential trend, suggesting we can approximate both $\psi(t)$ and $\Psi(t)$ as Poissonian processes. Second, tumbling times are much shorter than run times, suggesting that the static tumbling periods can be neglected. These considerations lead to a key assumption that is often adopted in RTP models: tumbling events can be considered as instantaneous processes, while run-times are Poisson-distributed. Consequently, a commonly used run-time distribution is:

$$\psi(t) = \frac{e^{-t/\tau}}{\tau}\,, \tag{1.3}$$

where τ indicates the mean run time. Notably, this model also assumes that successive run time are independent from each other.
Focusing instead on the distribution of turning angles, the reference experimental measurements are shown in Fig. 1.3B. The trend is generally more complex than the run time distribution. A functional form has been proposed for the experimental $h(\theta)$ of *E. coli*, using a model of strong rotational noise during the tumbling time, but it results in a non-trivial expression [89]. Nonetheless, it has been been shown that various transport properties of interest do not depend on the full turning angle distribution, but rather only

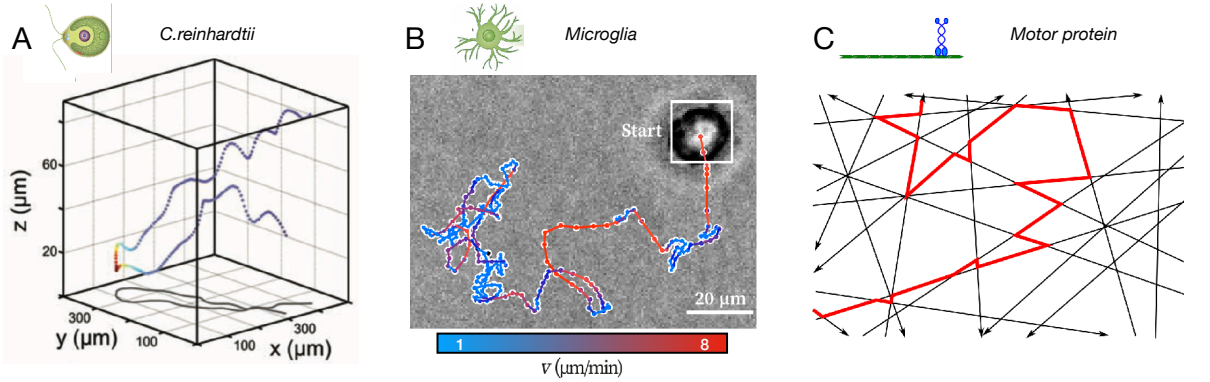

Figure 1.4: **Variety of Run-and-tumble motion**. A) 3D trajectory of microalgae *Chlamydomonas reinhardtii*, showcasing persistent motion (blue) and a localised re-orientation (red) [83]. B) 2D trajectory of a microglia, alternating slow phases where orientation is significantly changed and fast persistent stretches [67]. C) Sample trajectory of a motor protein on a cytoskeleton network [86].

on its first moment [82, 90], often expressed as the mean cosine of the turning angle:

$$\alpha \equiv \langle \cos h(\theta) \rangle \,. \tag{1.4}$$

The parameter α quantifies the directional persistence of tumbling events, and for *E. coli* it varies roughly from 0.2 to 0.7 depending on the run speed (see Fig. 1.3C).

Generalisation to Different Swimming Patterns Moving forward from the instructive case of an *E. coli*-inspired model, the RTP framework can be extended to other species, even for cases in which the full picture of experimental distributions is not readily available. For instance, choosing a $h(\theta)$ so that $\alpha = -1$ allows to reproduce sharp reversals of the direction of motion, typical of the *run-reverse* swimming pattern [51]. Another possible approach, which has become the standard version of RTP, is to assume a flat distribution for $h(\theta)$, resulting in isotropic re-orientations [6]. In general, many different forms of $h(\theta)$ and $\psi(t)$ have been proposed and studied. Additionally, the model can also be further extended, including for instance alternating velocity levels [91], or alternating re-orientation distributions to reproduce bimodal swimming strategies [82].

Generalisation Beyond Bacteria Over decades of research, RTP models have evolved from the motion of *E. coli* into the fundamental stochastic model of random persistent motion. Statistical mechanics research has characterised many fundamental properties of RTPs, like probability distributions [92], survival probabilities [93, 94] or first passage times [95, 96]. Other lines of research focused on thermodynamic quantities, such as entropy production [97], as well as scenarios involving various confining potentials [17, 98]. The model has also found applications in various biological systems beyond bacteria. For example, eukaryotic cell *Chlamydomonas reinhardtii* demonstrates run-and-tumble dynamics (Fig. 1.4A) through alternating synchronous and asynchronous flagellar beating [83, 99]. Similarly, macrophages like *Microglia* exhibit motion that alternates between runs and sharp re-orientations (Fig. 1.4B), with exponential tumbling distributions that

resemble bacterial dynamics [67]. Furthermore, the movement of motor proteins along cytoskeletal filaments is also characterized by active runs and stationary turns (Fig. 1.4C), and has been effectively modeled using RTP dynamics [85, 86].

Take-home Messages In summary, the RTP framework is a versatile stochastic model for random persistent motion with broad applications. Various versions and interpretations have been extensively studied in the literature. This thesis will focus specifically on RTPs applied to bacteria and microswimmers. In doing so, it will maintain key assumptions that were introduced in this section, such as the Poisson distribution for run-times and instantaneous tumbling.

1.2.3 Active Transport and Diffusive Regime

So far, stochastic active models have been introduced as tools for studying transport, without detailing the specific transport properties of interest and their relevance. This section will address these aspects.

Mean-squared Displacement A crucial metric in understanding the transport of particle motion is the mean-square displacement $M(t)$. This quantity is a measure of the average distance squared that a particle travels from its initial position over time. For a particle moving in d-dimensional space, the MSD is defined as:

$$M(t) \equiv \langle (\mathbf{r}(t) - \mathbf{r}(0))^2 \rangle \,, \tag{1.5}$$

where $\mathbf{r}(t)$ is the position of the particle at time t, and $\langle \cdot \rangle$ denotes an ensemble average over multiple realisation of the system. If we consider motion in the bulk—an idealized homogeneous environment with no obstacles and no taxis effects—the dynamics of a model combining both run-and-tumble dynamics and Brownian noise can be fully solved [82]. In the high Pe limit, the analytical solution for the mean-squared displacement, in d-dimensional space, is given by:

$$M(t) = \frac{2v_{\mathrm{o}}}{\lambda_{\mathrm{eff}}}(\lambda_{\mathrm{eff}} t - 1 + e^{-\lambda_{\mathrm{eff}} t}), \;\; \lambda_{\mathrm{eff}} \equiv (1-\alpha)\lambda + (d-1)D_{\mathrm{r}} \,, \tag{1.6}$$

where λ is the tumbling rate, i.e., the inverse of the mean run-time τ. λ_{eff} is known as effective tumbling rate, combining the reorientation effects of actual tumbling events and additional rotational "thermal" noise. As previously noted, the mean-square displacement in this scenario depends only on the first moment of the turning angle distribution $h(\theta)$, denoted α, rather than the full distribution [82,90]. Some example mean-squared displacement curves are shown in Fig. 1.5, including predictions for *run-reverse-flick* which can be obtained via an extended version of Eq. 1.6 to bimodal swimming patterns [91]. Across all mean-squared displacement curves, two regimes are identifiable: a ballistic regime at short times, showing a quadratic dependence on time, and a diffusive regime at long times, showing a linear dependence on time. The onset of the diffusive regime generally occurs at times greater than the persistence time of motion. This asymptotic diffusive limit is a characteristic shared across various types of stochastic motion, because, over long enough timescales, the random nature dominates over the specific dynamics, whether it is active, passive, or run-and-tumble-like.

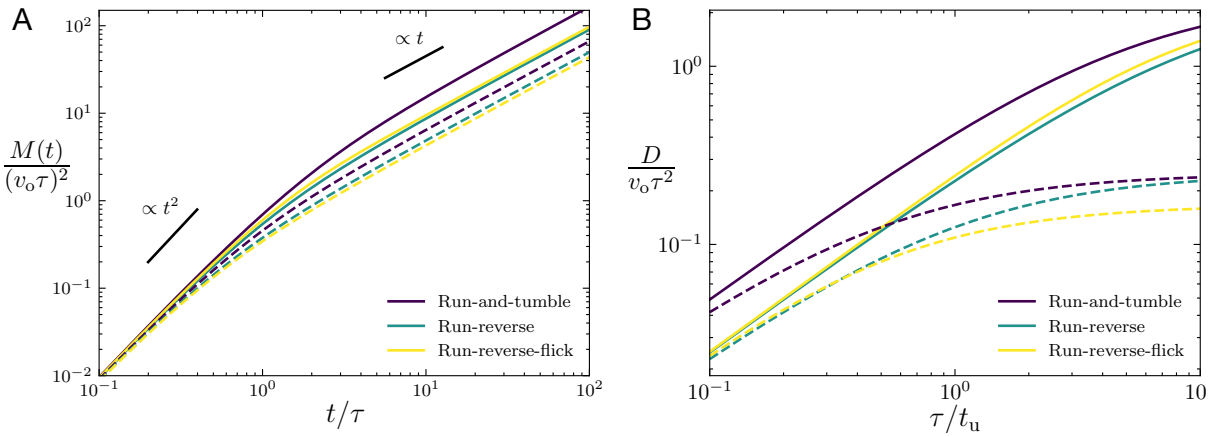

Figure 1.5: **Transport properties in bulk of active run-and-tumble particles subject to rotational noise.** A) Re-scaled mean-squared displacement versus time, rescaled by the mean run time, for different values of rotational noise and swimming patterns. Continuous lines represent low rotational noise ($D_r = 0.1\tau^{-1}$), while dotted lines represent high rotational noise ($D_r = 10\tau^{-1}$). B) Re-scaled diffusivity versus tumbling rate, for the different cases shown in the left plot. t_u denotes a generic time unit.

Diffusive Regime The key quantity that describes the diffusive regime is the traslational diffusion coefficient, defined as the asymptotic limit of the mean-squared displacement over time:

$$D \equiv \frac{1}{2d} \lim_{t\to\infty} \frac{M(t)}{t} \,. \tag{1.7}$$

This quantity is originally defined to quantify the rate at which a particle diffuses due to thermal noise. It has since been generalized to stochastic active motion, which often exhibits larger diffusion coefficients than the thermal case. In the generalisation to active matter, D is often re-named to *effective diffusion coefficient*, or in some cases *diffusivity*. In this work, these terms will be used interchangeably, all referring to the original definition of Eq. 1.7. For motion in bulk, analytical solutions can be derived from the previous mean-squared displacement formula, yielding:

$$D = \frac{v_o}{d\lambda_{\text{eff}}} = \frac{v_o}{\lambda d(1-\alpha) + D_r d(d-1)} \,, \tag{1.8}$$

which corresponds to the bulk diffusivity of a particle that is subject to rotational noise, instantaneous tumbling and Poissonian run-times. Examples of diffusivity as a function of mean run-time are shown in Fig. 1.5B, for different swimming patterns and levels of rotational noise. The general trend indicates a monotonic relationship between diffusivity and run-time, highlighting that particles with higher persistence exhibit a greater dispersion. This consideration also explains why increased rotational noise generally reduces diffusivity (comparing solid and dotted lines). Additionally, motility patterns with higher orientational persistence (run-and-tumble), result in higher diffusivity trends when compared to the other cases (run-reverse and run-reverse-flick).

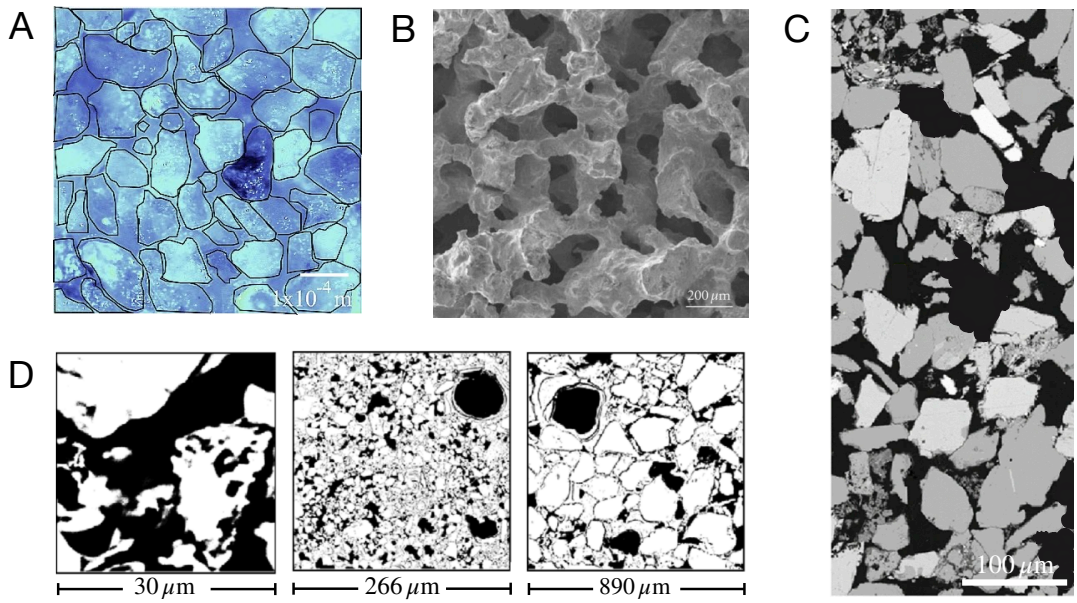

Figure 1.6: **Microscopic snapshots of bacterial habitats**. A) Typical optical image of a sand sediment, with solid interfaces outlined in black [100]. B) Microscopic structure of an alloy foam used in biomedical applications [102]. C) Cross-section of porous rock: pores in black and grey regions indicating solid obstacles such as clay, rock fragments, and eroded debris [104]. D) Binary images of thin soil layers, at different scales. Solid objects in white, pores in black [101].

1.3 Motion in Complex Environments

In the previous discussion, bacterial motion was first analyzed from real observations of bacteria, and then in terms of stochastic models that reproduce active motion. In both scenarios, motion has been considered to take place in a theoretical void, in which the environment is unobstructed and homogeneous. Moving forward, the aim is to broaden the focus to motion within more realistic and complex environments, that include obstacles and confinement. Additionally, the generality of active particle models is leveraged to shift the focus from bacteria to the broader concept of microswimmers, encompassing both biological and non-biological agents.

Why Complex Environments? The need to study complex environments arises from the observation that typical habitats of microorganisms include sand and soil sediments [100, 101], porous rocks [10], or foams [102]. From example shown in Fig. 1.6, it is clear that these environments present various types of interfaces. Despite the presence of confinement, large numbers of bacteria have colonised these complex spaces. For instance, the typical number of bacterial cells that can be found in a single gram of soil is around 10^8, with an estimated diversity of 10^4 species [3, 103]. Another striking example comes from estimates that place approximately 70% of the total bacterial biomass, encompassing an estimate of 10^{29} cells, within deep terrestrial and oceanic subsurface sediments [1, 28]. Microorganisms that live in such complex substrates, and that are motile, need to be able to navigate amid solid interfaces to survive.

Relevance and Potential Applications Building models for transport in these environments is essential for understanding and controlling the dynamics of these processes, and is relevant for different applications. For instance, bioremediation schemes use bacterial agents for the cleanup of groundwater, and their design relies on effective models for bacterial transport under various physical, biological, and geochemical conditions [105]. The ability to navigate confined environments can also determine the spread of infections due to pathogenic bacteria [4, 106]. This issue is pertinent not only to biological microswimmers but also extends to non-biological systems. For example, it connects to the advancement of engineered microrobots that mimic bacterial movement patterns, enabling them to navigate intricate structures for drug delivery purposes [5, 107]. Additionally, this research is relevant to targeted delivery methods, like developing magnetically driven microrobots that target hard-to-reach tissues [23] and localized drug delivery to cancer cells [108].

The primary goal of this section is to present how the existing stochastic active particle models can be extended to study confinement. With this objective in mind, this section will first explore the experimental results available in literature, to establish an overview of what are the possible dynamics of bacteria, or microswimmers, in the presence of solid obstacles and confinement.

1.3.1 Microswimmer Dynamics at Solid Interfaces

A critical aspect of modeling microswimmer transport near solid interfaces is understanding the dynamics of swimming upon collision with solid boundaries. Given the complex and varied nature of interactions that real microswimmers exhibit with surfaces [109], there is no universal behavior for different specie and/or different surfaces. In general terms, the influence of solid boundaries on the dynamics of motile cells involves both hydrodynamic and steric forces [110], and in some cases it may also involve biological responses that change cell behaviour as a reaction to mechanical stimuli [111].

Hydrodynamics: Pushers and Pullers A first instructive example of surface behavior is the case of microalga *Chlamydomonas reinhardtii*, which is classified as a puller [112] — meaning its propulsion is generated in front of the cell body. These microalgae are hydrodynamically repelled by flat solid surfaces [113], and exhibit scattering from flat walls due to the contact of their flagella with the surface, leading to billiard-like motion within polygonal geometries [114]. Conversely, pusher-type microswimmers, which generate thrust behind the cell body, display a propensity to approach flat walls, driven by long-range hydrodynamic interactions. This behavior, documented in species such as flagellated bacteria, spermatozoa, and Janus particles, results in their entrapment near planar surfaces, and is due to a combination of hydrodynamic and steric forces [115].

Pushers on Flat Walls For the sake of the work presented later, it is necessary to focus on pusher-wall interactions, starting with the case of motion in the presence flat walls. In these scenarios, it has been observed that pusher-type microswimmers, such as bacteria or chemically-propelled micro-rods, can continue move on the surface for extended periods after impact [119, 120]. Fig. 1.7A illustrates an example of this motion, showing a 3D

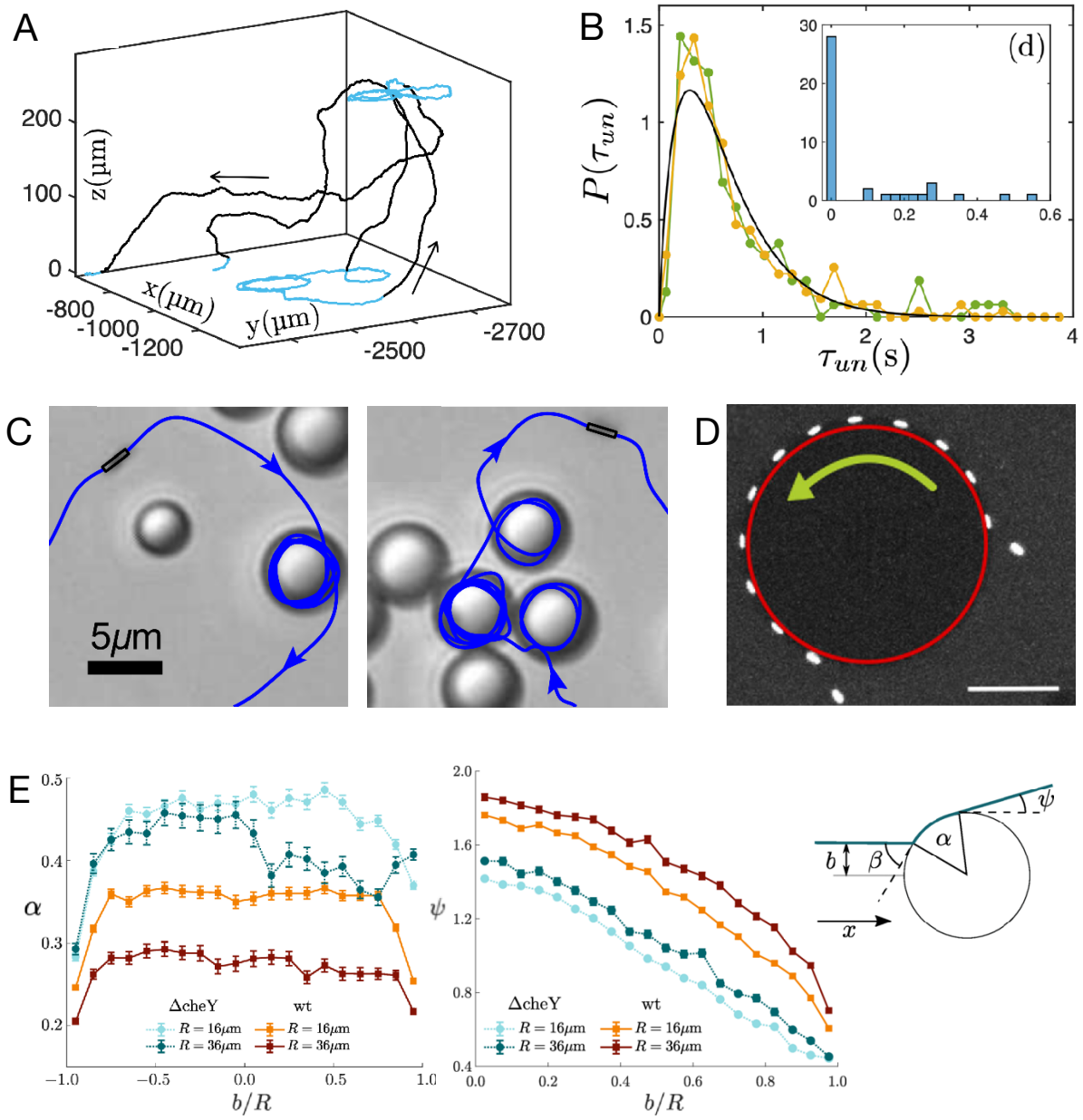

Figure 1.7: **Microswimmer dynamics on solid interfaces**. A) 3D track of *E. coli* within a planar slit, showing bulk motion (black) and surface persistence (blue). B) Distribution of tumbling time on the surface (orange) and in bulk (green). Inset: distribution of time delay between surface detachment and tumbling events [11]. C) Sample trajectories of self-propelled rods orbiting passive spheres [116]. D) Image sequence of a fluorescent bacterium following a micropillar surface [117]. E) Surface dynamics of smooth-swimming mutant (ΔcheY) and wild-type (wt) *E. coli* on on pillars of different radii. Traversed polar angle (left) and detachment angle (right), as a function of impact parameter. Adapted from Jakuszeit *et al.* [118].

track of *E. coli* in a flat channel alternating between bulk and surface movement. At the boundary, the motion involves aligning the travel direction parallel to the boundary after impact. This is typically followed by circular paths, which result from the interplay of chiral flagellar propulsion and frictional forces between the counterrotating cell body and the surface [110, 121]. Junot *et al.* [11] have extensively studied the dynamics of this surface behaviour for the case of *E. coli*. The study shows that tumbling at the surface occurs at the same rate as in bulk (see Fig. 1.7B), and that tumbling is the primary mechanism by which bacteria detach from surfaces (inset of Fig. 1.7B).

Pushers on Circular Obstacles The geometry of the solid interface has been found to alter surface dynamics. For example, when considering circular obstacles like solid spheres, active micro-rods can enter short-range orbits that follow the obstacle's surface, as illustrated in Fig.1.7C. These orbits occur with minimal change in speed and display randomized escape patterns [116]. Similarly, *E. coli* can swim for extended periods along convex walls with sufficiently low curvature [117], tracing orbits around large enough pillars, as shown in Fig. 1.7D. The capture of pusher-type microswimmers on circular boundaries has been explained using models that combine hydrodynamic interactions and hard-core repulsion [122], with the trapping aspects being the same as the case of flat boundaries. However, residence times and escape mechanisms appear to differ when consider circular obstacles rather than flat surfaces, with evidence suggesting that convex walls decrease trapping duration [123,124]. A recent work by Jakuszeit *et al.* [118] studied the surface dynamics of *E. coli* in the presence of cylindrical pillars. Results show that surface residence times on convex walls depend on both surface curvature and impact angles (Fig. 1.7E). Moreover, by replicating the study for wild-type and non-tumbling mutants, they show that, similarly to flat walls, tumbling plays a significant role in surface detachment from surfaces.

Take-home Messages Microswimmer transport near solid surfaces involves complex interactions, including hydrodynamic and steric forces. These interactions vary based on the swimmer's propulsion type and surface shape. Pushers are attracted by surfaces, leading to surface residence and surface motion. On circular obstacles, pushers can orbit by moving along convex surfaces, resulting in complex dynamics. Although the mechanisms of surface residence is not fully understood, various studies suggest tumbling plays a crucial role in detachment from the surface.

1.3.2 Motion in Confinement: a Vast Parameter Space

The central topics explored in the thesis involve defining a model for motion in confinement, which extends active particle models to include interactions with solid interfaces. With this objective, this section provides an overview of the extensive parameter space that must be considered when modeling motion in confinement. Variability arises from several sources, including the large diversity of natural environments [1, 28, 100, 101], the variability in swimming and movement patterns [58, 59, 83], and, as discussed in the previous section, the lack of universal behavior for microswimmers on solid surfaces [11, 117, 119]. Therefore, it is useful to break down each of these variabilities to have clear picture of the parameter space.

Variability of Confining Environments The first and most straightforward variable is the confining environment. That is, the geometry and distribution of solid boundaries in space. Various studies have focused on simple slit or channel-like structure [19, 125]. More complex environments have also been studied, with the aim of reproducing natural or artificial porous environments [20–22, 126–131]. Porous media models in literature generally include solid obstacles that can be distributed in space in diverse ways. Common approaches include obstacles that vary in placement (ordered on a lattice or randomly distributed), shape (typically circular geometries like disks, spheres, or pillars) or size distribution (mono-disperse or poly-disperse).

Variability of Swimmer Models The second source of variability is the wide range of microswimmer dynamics and movement patterns. Studies in literature have adopted hydrodynamic models [80, 81, 117], RTPs [22, 129], ABPs [19, 87, 126], or approaches combining the previous models [21, 128, 132]. For the stochastic cases, there are many variations stemming from basic RTP and ABP definitions, such as varying swimming patterns, which could have non-trivial effects on transport properties when coupled with confinement. Moreover, a defining modeling choice is whether to consider interacting or non-interacting particles, which results in either a single-body or multi-body problem. In general, the two cases have different levels of complexity, with the non-interacting case allowing for easier analytical formulations, while representing the dilute limit of the interacting model.

Variability of Particle-Surface Interactions The third and possibly most open-ended source of variability is the particle-surface interactions. Typical behaviors include residence on walls [11], where agents either become trapped or motionless after a collision [133], or microswimmers that attach to and slide along walls or obstacles [116, 119]. In models of surface persistence, a crucial aspect is also understanding how particles detach from surfaces. The mechanism of escape is not fully understood [127], and there might not be a universal behavior valid across different swimmers and/or surface types. An emerging trend for bacteria is that detachment from surfaces is linked to tumbling events [11, 127]. Additionally, surface behaviors different than residence could be considered, such as surface scattering for puller-type swimmers [83], or surface crawling by twitching [2].

Take-home Messages Various studies in literature have extended active particle models to include motion in confinement [19–22, 125–132]. These models require defining stochastic interactions that mimic the complex microswimmer dynamics on solid boundaries, for which a comprehensive understanding is currently lacking. Consequently, many different confining environments and particle-surface interactions have been considered, resulting in a varied and mostly unexplored parameter space. The different approaches presented in this section will be useful to better define and compare the models in literature presented in the next section.

1.4 State of the Art

This section presents the state of the art for active diffusivity in confinement, particularly focusing on key analytical and numerical studies. Other than summarizing the main findings, the aim is also to highlight limitations and gaps in current research. This will help outline the objectives of this thesis, which intend to address the presented research gaps. To organize the results presented in the state of the art, the presented studies are divided into two categories based on the considered environment geometry. First, the focus is on active particles moving within slit and channel-like environments. Then, the focus shifts to active diffusivity in porous media.

1.4.1 Active Particles in Channels

Active Accumulation on Flat Interfaces Regarding motion in the presence of flat solid interfaces, a central topic of research has focused on accumulation: the phenomenon where particles gather or build up near surfaces or boundaries. This generic behavior is a result of either the particles' persistent motion or interactions with the walls. The general mechanism that leads to accumulation is straightforward: as an active particle approaches a wall, it needs to reorient to move away, causing it to spend more time near the wall and leading to an increased concentration of particles at the boundary. This active accumulation connects to the numerous experimental studies on microswimmer capture on solid boundaries [11,117,118,120] presented in Section 1.3.1. However, providing an exact theoretical description of swimmer accumulation near flat walls remains challenging, and can be further complicated by accounting for specific wall trapping behaviours of pusher-like swimmers. Various approaches and approximations have been employed to explore particle distributions near flat interfaces.

Distribution Profiles Within Channels An extensively studied topic in relation to accumulation processes is the distribution of particles within slit-like structures. These structures consist of empty channels where particles move between two infinitely long, parallel walls. For instance, the steady-state distribution of non-interacting ABPs between two confining walls has been characterized through theoretical and numerical methods [19]. These results predict accumulation on flat walls and quantify the distribution profile, including the fraction of particles at the wall as a function of slit width (see Fig. 1.8A). Related studies focus on the interacting ABP case in similar confinement, resulting in complex dynamics that also involve accumulation near boundaries [125]. Research has also extended these findings to RTPs. Like ABPs, RTPs exhibit accumulation near walls, but persistence leads to distinctive features such as sharp peaks in density profiles adjacent to walls [18]. The one-dimensional case is fully tractable [134–136], and analytical solutions exist for higher dimensions in some limits [18]. It has been shown that the fraction of particles at the wall and the steady density profile depend on run-and-tumble characteristics, such as mean run-time and run-time distribution, as shown in Fig. 1.8B. Additionally, complementary studies have modeled other phenomena linked with accumulation, such as pressure exerted on flat interfaces, for both the ABP [137] and RTP case [138].

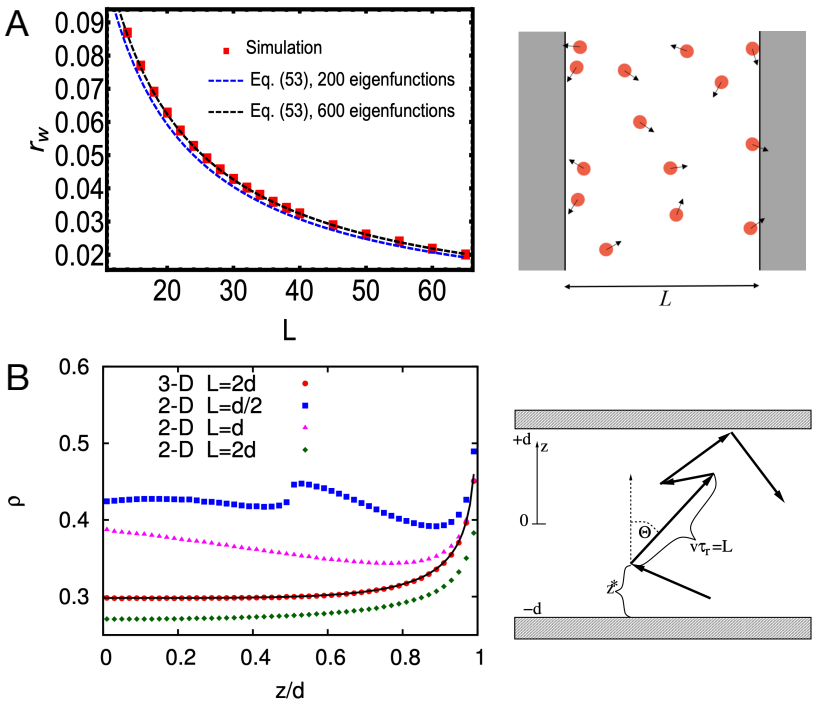

Figure 1.8: **Distribution of active particles in slit-like structures**. A) Fraction of particles that accumulates on the wall as a function of channel width, for non-interacting ABPs in channel confinement [19]. B) Distribution profile within a slit, for RTPs with different run length distributions, in two or three dimensional channels. [18].

Limitations and Research Gaps Despite extensive research on the distribution and accumulation of active agents within slit-like structures, much less attention has been given to transport along boundaries. This process is nonetheless very relevant, as it determines whether microorganisms or motile cells can invade, escape, or travel through interstitial spaces. The simple geometry of a planar slit, characterized by a single length scale, provides also a fundamental understanding to deal with more complex media. By excluding structural disorder, it allows a focus solely on the effects of confinement. Additionally, the impact of swimming strategy and rotational noise on RTP motion has been minimally explored in relation to this type of confinement. Overall, a comprehensive diffusivity model for RTPs in slit-like confinement is currently lacking in literature, while other properties, such as accumulation and distribution profiles, have been extensively studied.

1.4.2 Active Diffusivity in Porous Environments

Differently from the case of slit-like structures, there are numerous studies on the dispersion of active particles within porous media, reflecting also the larger diversity of possible porous environments. Transport of generalized RTP models in porous media is typically predicted to exhibit asymptotic diffusive behavior [139,140], similarly to bulk motion. As a general trend, if surface behaviours can trap particles, the porous structures is expected to hinder transport by causing collisions with obstacles, reducing diffusivity in comparison

to bulk motion [16,133,141]. Conversely, if particles can instead move along surfaces, the porous structure might instead facilitate dispersion, possibly enhancing diffusivity compared to bulk motion [126,127]. In this section, the objective is to map out key predictions in literature for diffusivity predictions. Overall, different scenarios are considered, ranging from ordered to disordered porous media, for ABPs, RTPs, or other comparable active particle models.

Motion within Ordered Arrays of Obstacles A primary line of research focuses on rdered porous media, such as solid spheres or pillars placed on a regular lattice. A key initial study explored the possible transport dynamics in these environments. It used an ABP model combined with hydrodynamic surface interactions that mimic various swimming modes, ranging from pushers to pullers [132]. The study predicts that diffusive motion is observed for both strong and weak pushers, and across a large range of obstacle densities. However, it did not characterize or predict the actual diffusion coefficients. Indeed, direct analytical approaches for diffusivity are not straightforward, even for circular obstacles ordered on lattices [7, 142]. Consequently, diffusivity prediction in porous media often resorts to a combination of numerical approaches and/or simplifying assumptions [87, 126].

Diffusivity Predictions under Simplifying Assumptions An emerging approach for simplified diffusivity predictions starts from the bulk results (See Eq.1.8), extending the formula under specific approximations. A first example of this method was introduced by Licata *et al.* [20], who developed a simple formula for diffusivity in a generic porous environment characterized solely by pore size, without specifying a particular geometric structure. In a similar manner, a more recent study modified the bulk RTP diffusivity to predict the dispersion of ABPs moving through an ordered array of obstacles [127]. This study successfully approximates the long-term effects of particle-surface interactions as if they were effective tumbling events. Lastly, a re-adaptation of the bulk solution was also applied successfully to experimental tracks, for the case of *E. coli* moving through ordered arrays of pillars [118].
Beyond reworking the bulk predictions, there are various attempts in literature to predict diffusivity through direct theoretical models. These models typically rely on simplifying assumptions to achieve solutions. For instance, Bertrand *et al.* [22] studied RTP-like tracers with motion restricted on a regular lattice, in the presence of fixed or motile obstacles. Despite this simplifying assumption, the resulting diffusivity predictions are non-trivial and fully explicit only in the limits of static obstacles at low density [129].

The Emergence of Optimality The development of diffusivity models for confined environments opens the door to addressing other pertinent questions. A key area of growing interest is optimality, which involves determining the optimal swimming parameters, relative to the environment, to maximize diffusivity. From an artificial systems perspective, this is relevant for developing optimal navigation strategies. On the biological side, it can offer insights into how bacterial characteristics and environmental properties correlate and correspond to evolutionary advantages. In regards to optimality, initial trends emerge from diffusivity models under simplified assumptions. Both Licata *et al.* and Bertrand *et al.* predict a maximum in diffusivity as a function of tumbling rate (See Fig. 1.9 A and B).

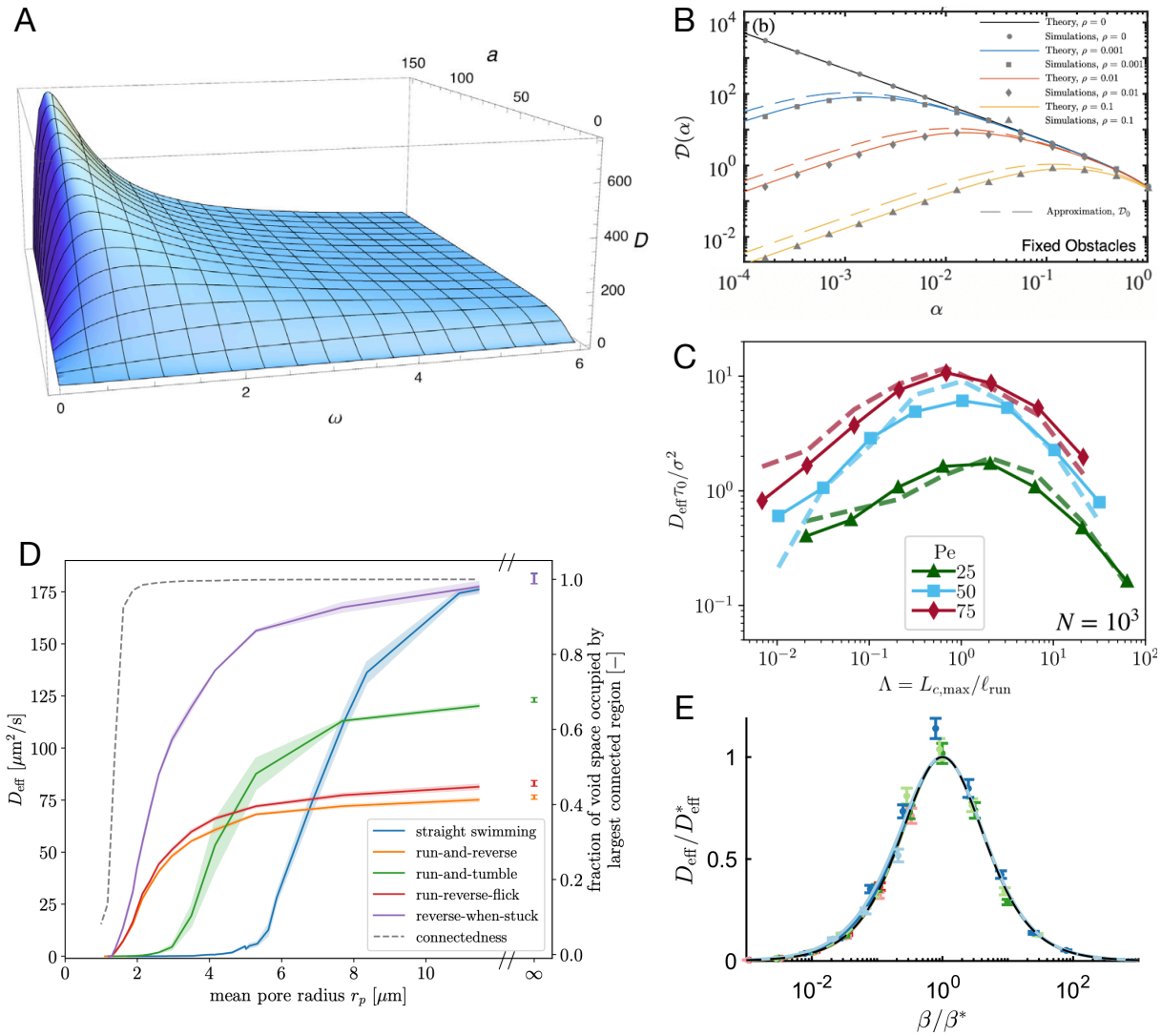

Figure 1.9: **Active diffusivity in porous environments** A) Diffusivity prediction map for non-explicit porous geometry, as a function tumbling rate (ω) and pore size (a) [20]. B) Diffusivity as a function of run-length for stiff RTP-like polymers with different Peclet numbers, in disordered media [21]. C) Numerical estimates of diffusivity for RTP-like stiff polymers for different swimming patterns, as a function of pore size [128]. D) Diffusivity predictions of a simplified RTP model in idealised porous media [22]. E) Rescaled diffusivity as a function of rescaled tumbling rate, comparing simulations and a non-explicit geometry model [131].

These models suggest that optimal run lengths, comparable to the mean pore size, result in diffusivity maxima. Building on these initial findings, further studies have investigated this optimality. A significant work by Kurtzhaler *et al.* numerically assessed the diffusivity of stiff polymers, elongated swimmers of finite size performing RTP-like motion, navigating through a three-dimensional, disordered porous medium. This research characterized the impact of varying tumbling rates and obstacle densities on diffusivity [21]. The study identifies an optimal tumbling rate for dispersion, explained by a criterion predicting maximum diffusivity when mean-run lengths are comparable to the porous structure's largest free-space chord (See Fig. 1.9C).

Recent and Ongoing Advancements Interest in this topic has grown significantly in recent years, with notable results emerging throughout the course of the PhD period. A paper published at the end of 2023 focused on identifying optimal swimming patterns for dispersion in disordered porous media [128]. This work examined RTP-like stiff polymers and how diffusivity depends on obstacle density for different swimming strategies. The findings revealed that certain movement patterns can be more advantageous for diffusivity (see Fig. 1.9D). While most studies focus on surface residence models, where particles remain motionless at walls and escape by reorienting, recent works have begun exploring RTP models that include both residence and sliding behavior along obstacle surfaces. This trend follows from recent advances in understanding bacterial dynamics on surfaces (see Section 1.3.1). In this area, a first work published in 2023 considers RTPs that can slide along circular pillars in a disordered environment, investigating the dependence of diffusivity on tumbling rate and obstacle density. The study provides explicit solutions valid in some limits, but did not report any diffusivity maximum [130]. A second study by H. Mattingly, available as a preprint at the time of writing, presents numerical data for another RTP model that can slide along circular obstacles. This work proposes an analytical prediction based on simplified assumptions, which leads to a model valid for non-explicit porous media [131]. This approach, similar to that of Licata *et al.*, also predicts a diffusivity maximum as a function of tumbling rate, suggesting that optimal run lengths can be observed for motion that includes surface sliding (see Fig. 1.9E).

Limitations and Research Gaps Research on active diffusivity in porous environments has grown significantly in recent years. Current understanding involves numerical and theoretical approaches using different swimmer models in both ordered and disordered environments, considering different surface behaviors. A key issue remains whether results obtained for specific conditions are applicable to other scenarios. Despite some emerging common trends, a unifying picture is lacking. The reliance on numerical results and models with simplifying assumptions results in a lack of comprehensive understanding, raising the question: Is it necessary to explore the vast parameter space, considering all possible combinations, to achieve a general understanding?
At least four studies [20–22, 131] have reported a maximum in diffusivity for optimal persistence lengths, a relevant finding for applications. However, the generality of this maximum is not yet understood. Additionally, the issue of optimality has been minimally addressed concerning other parameters, such as swimming patterns or rotational noise.

1.5 Objectives of the Thesis

This final section of the chapter provides an outline for the structure and objectives of the thesis, linking the discussion to the state of the art and the research gaps identified earlier.

Second Chapter The second chapter presents a theoretical and numerical study on effective run-and-tumble models in slit-like confinement. It focuses on transport along the confining direction, specifically lateral diffusivity. This chapter aims to complement the extensive research on accumulation within channel-like structures (See Sec. 1.4.1), by bridging the current research gap for a complete model of diffusivity in slit confinements. To do so, it will develop a simplified formulation for transport of non-interacting RTPs, which is extensively checked and extended *via* simulations. The aim is to develop practical expressions for diffusivity, able to encompass diverse types of motion. Additionally, the focus is also on optimality, using the model to identify the swimming parameters that maximize transport.

Third Chapter The third chapter continues the theoretical and numerical approach, being a natural continuation of Chapter 2. It moves from the simple setting of a slit-like environment, to a more generic and disordered porous structure. As highlighted by Sec. 1.4.2, various studies have already addressed diffusivity in porous environments. Therefore the aim of the chapter aims to create a comprehensive model, able to encompass different geometries, swimming strategies, and surface behaviors. It addresses the lack of a unified picture in the current research, proposing a framework that applies to a large diversity of scenarios, as demonstrated through the extensive numerical investigation presented. This chapter also explores the concept of optimality, specifically the existence of optimal run-lengths that maximize diffusivity. Through modeling and simulations, the goal is to clarify the mechanisms behind this phenomenon, which has been observed and reported in the literature but is not yet fully understood.

Fourth Chapter The fourth chapter shifts focus from theory and simulation to experiments. Its aim is to characterize a novel strain of Magnetotactic bacteria, which has gained significant attention in recent years. The study begins by examining the magnetic response and basic transport properties of this new strain, for which detailed motion characterization is still lacking. Additionally, it presents early findings on the interaction between magnetically driven motion and solid boundaries, revealing complex and unexpected behaviors. While this chapter is less directly connected to the previous two and remains more open-ended, it offers experimental insights that complement the theoretical work and addresses unresolved issues related to the movement of Magnetotactic bacteria.

Each chapter aims to bridge gaps in current research and provides a clearer understanding, from many different points of view, of bacterial motility in complex and confined environments.

CHAPTER 2

Optimal Run-and-tumble in Slit-like Confinement

Contents of this Chapter

This work is largely inspired by the published article Pietrangeli *et al.*, Physical Review Research 2024 [143], where the results presented here have been first introduced.

2.1 Introduction

This chapter builds upon the state of the art presented in Chapter 1, specifically addressing the gaps in predicting dispersal within channel-like structures, as outlined in Sec. 1.4.1. The study examines motion within a slit, modeled as two infinitely long parallel and flat boundaries. Particles move confined within the two surfaces, alternating between bulk motion and residence at the boundary. The focus is on developing a model able to predict the longitudinal diffusion coefficient, a key indicator of long-time exploration in

the direction parallel to the confinement. The primary outcome of the work will be a fully solvable theoretical model, which is then validated and extended through extensive numerical analysis. These results enable accurate predictions of diffusivity, accounting for run-and-tumble characteristics, surface interactions, and confinement size. Finally, the model is then used to identify conditions under which dispersal can be maximized by optimizing the mean run time. The finding suggests that, for specific scenarios relevant to both bacteria and cells, long-time exploration is most efficient when the mean run length matches the confinement size. Given the model's adaptability, this optimality criterion could apply to a wide range of microorganisms, broadening the understanding of optimal diffusivity in confined environments [20–22, 131].

Outline of the Chapter This chapter is organized as follows. Section 2.2 formally defines the problem and introduces a discrete-direction model, from which a simple yet exact formula for the diffusivity is derived. In Section 2.3, the validity of this diffusivity predictions is tested and extended through simulations of a "continuous-directions" model, demonstrating that the analytical results provide a good approximation when effective parameters are properly defined. Section 2.4 then uses the validated model to explore optimality, identifying the conditions under which dispersal is maximized. Finally, Section 2.5 provides a summary and offers perspectives for future work.

2.2 Analytical Approach: the Four-direction Model

The objective of this study is to characterize the longitudinal spreading of an run-and-tumble particle (RTP) confined within a slit *i.e.* two parallel infinite walls spaced W (Fig. 2.1a). Throughout, the focus will be exclusively on the single-particle problem, valid for either a dilute limit or an ensemble of non-interacting particles. A complete description of the motion within the slit involves tumbling events, rotational diffusion, and wall-bound motion, the combination of which presents significant analytical challenges. As discussed in Sec. 1.4.1, even the simpler task of determining the density profile across the slit is already complex for the case of ABPs, as highlighted in previous works [19, 125, 137, 138, 144–147].

To maintain analytical tractability, a simplified description is first adopted: the "Four-direction Model" depicted in Fig. 2.1b. As detailed in following sections, this minimal model is exactly solvable. The relevance of this approximation for realistic more run-and-tumble dynamics will be then tested in Sec. 2.3.

Model Description Consider an RTP confined to two-dimensional motion, whose motion is restricted to a discrete set of directions—a simplifying approximation already employed in various studies [22, 144, 148–150]. As shown in Fig. 2.1b, the particle's runs occur along the four cardinal directions: left, right, up, and down (R, L, U, D). Within the slit of width W, the particle moves with velocity v_o and tumbles according to a Poisson process with rate λ, in a manner that is not necessarily isotropic. Upon reaching the wall, the particle randomly selects a new direction—left $\bar{L}$ or right $\bar{R}$—with equal probability and proceeds along the surface in a one-dimensional run-and-tumble process with veloc-

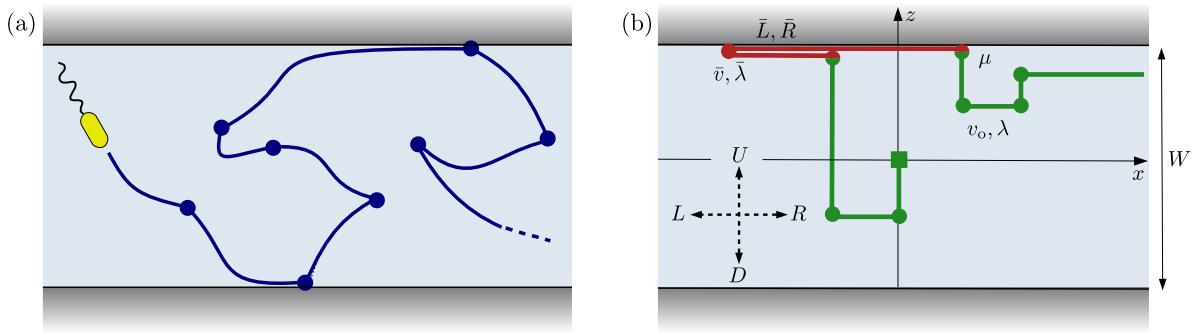

Figure 2.1: **Run-and-tumble particle confined in a slit.** (a) The basic scenario that inspires this work: a swimming bacterium moving in a slit-like structure: two flat, infinite, parallel walls. (b) Schematic description of the four-direction model: a run-and-tumble particle constrained to four directions. Parameters are described in Sec. 2.2.

ity $\bar{v}$ and tumbling rate $\bar{\lambda}$. Finally, a particle on the surface may escape back into the slit with rate μ. Motion can be modeled as a combination of Telegraph processes [151–153], a framework originally introduced to describe signal propagation along a telegraph wire.

2.2.1 Method of Resolution

The model is fully solvable analytically. Before detailing the derivation, the general approach is outlined. Given the finite number of motion directions, the evolution equation for particles moving in each direction can be written in a manner similar to the classical Telegraph process [151–153]. By applying Fourier transforms to the spatial variables ($x \to q$ and $z \to k$) and a Laplace transform to the time variable ($t \to s$), the coupled equations are converted into a linear system, which can then be solved within the slit's inner region. The next step involves determining the appropriate boundary condition that links the surface distribution to the slit distribution near the walls. The final outcome is a set of explicit expressions for the probability distributions at the surface and within the slit, ultimately yielding the diffusion coefficient.

For clarity, the method is initially described in the simplest scenario, where *(i)* tumbles are isotropic, and *(ii)* the particle is motionless at the surface, i.e., $\bar{v} = 0$. The calculation is subsequently extended to more general cases. Readers interested only in the final result may skip directly to Sec. 2.2.3. For conciseness, quantities are made dimensionless by using v_o as the unit velocity and the slit half-width $w \equiv W/2$ as the unit length[1]. The slit spans the interval $[-1, 1]$. Even though $z = 1$ and -1 represent the upper and lower surfaces, $z = \pm w$ is used here to emphasize that these positions correspond to the walls.

Evolution Equation within the Slit Let's start by introducing $R(x, z, t)$, the distribution of particle located at position (x, z) at time t and moving rightward. A similar definition applies for distributions L, U and D. In terms of (x, z, t) variables, the four

[1]Since the unit time is w/v_o, rates such as λ are made dimensionless using v_o/w.

distributions evolve according to the governing equations

$$\partial_t R = -\partial_x R - \lambda R + \lambda' P, \tag{2.1a}$$
$$\partial_t L = +\partial_x L - \lambda L + \lambda' P, \tag{2.1b}$$
$$\partial_t U = -\partial_z U - \lambda U + \lambda' P, \tag{2.1c}$$
$$\partial_t D = +\partial_z D - \lambda D + \lambda' P, \tag{2.1d}$$

where $P \equiv R+L+U+D$ is the total density within the slit and $\lambda' = \lambda/4$ is the tumbling rate toward motion in a particular direction. Switching to (q, k, s) variables by using Fourier transforms for x and z, and Laplace transform for t, and denoting as X_{in} the initial value of distribution X, one gets

$$\begin{bmatrix} s+3\lambda'-iq & -\lambda' & -\lambda' & -\lambda' \\ -\lambda' & s+3\lambda'+iq & -\lambda' & -\lambda' \\ -\lambda' & -\lambda' & s+3\lambda'-ik & -\lambda' \\ -\lambda' & -\lambda' & -\lambda' & s+3\lambda'+ik \end{bmatrix} \begin{bmatrix} R(q,k,s) \\ L(q,k,s) \\ U(q,k,s) \\ D(q,k,s) \end{bmatrix} = \begin{bmatrix} R_{\text{in}}(q,k) \\ L_{\text{in}}(q,k) \\ U_{\text{in}}(q,k) \\ D_{\text{in}}(q,k) \end{bmatrix}. \tag{2.2}$$

Such a linear system is readily solved. The solution describes the particle distribution within the slit only, since loss and source terms associated with the surface are not taken into account at this point. From now on, it is assumed that particles are released at the origin with isotropically distributed initial direction. This choice of initial condition is for simplicity and has no influence on the long-time diffusion coefficient. This gives $R_{\text{in}} = L_{\text{in}} = U_{\text{in}} = D_{\text{in}}$ and $R_{\text{in}}(x, z) = \delta(x)\delta(z)/4$. Given these initial conditions and the slit symmetry, the distributions of particle on the upper and lower surfaces are identical at all time, and denoted as $\mathcal{W}(x, t)$.

Boundary Conditions The discussion turns to the boundary condition applied at the surfaces, for $z = \pm w$. Though a solution may be sought for each of the individual R, L, U and D distribution, it is actually sufficient for our purpose to focus on the group of vertically-moving particle, whose distribution is $V \equiv U + D$. Proceeding as in aprevious work on confined Telegraph process [134], we first combine Eqs. (2.1c) and (2.1d) to get

$$\partial_t[U-D](x, z, t) = -\partial_z V - \lambda[U-D], \tag{2.3}$$

an equation that holds anywhere within the slit. Now, for a position approaching the upper surface ($z \to w$), one has

$$U(x, w, t) = \mu\mathcal{W}(x, t) + \partial_t\mathcal{W}(x, t), \tag{2.4a}$$
$$D(x, w, t) = \mu\mathcal{W}(x, t). \tag{2.4b}$$

The first equality is an evolution equation for the surface distribution $\mathcal{W}(x, t)$, with a flux $\mu\mathcal{W}$ of particles leaving the surface and a flux $U(x, w, t)$ coming from the slit. The second equality requires that in the immediate vicinity of the upper wall, downward-moving particles originate from the surface. Switching to transformed variables and using

$\mathcal{W}_{\text{in}}(x) = 0$ gives

$$(s+\mu)\mathcal{W}(q,s) = U(q,w,s), \tag{2.5a}$$
$$\mu\mathcal{W}(q,s) = D(q,w,s). \tag{2.5b}$$

Exploiting Eq. (2.3) finally gives for $V(q,z,s)$ the Robin boundary condition [154]

$$\partial_z V|_{z=w} = -\frac{s(s+\lambda)}{s+2\mu} V|_{z=w}. \tag{2.6}$$

The boundary condition at the lower surface $z = -w$ is obtained by symmetry.

Resolution An explicit solution for the distribution of vertically-moving particle $V(q,k,s)$ can now be found. With $f(z) \equiv V(q,z,s)$ for conciseness, the solution of Eq. (2.2) gives $f(k) = c_1/(c^2+k^2)$ and[2]

$$c^2 f(z) - f''(z) = c_1 \delta(z), \tag{2.7}$$

where the positive constants c and c_1 are independent of z and read as

$$c^2 = \frac{(s+\lambda)\left[q^2(2s+\lambda) + 2s(s+\lambda)^2\right]}{2q^2+2s^2+3\lambda s+\lambda^2}, \tag{2.8a}$$
$$c_1 = \frac{(s+\lambda)\left[q^2+(s+\lambda)^2\right]}{2q^2+2s^2+3\lambda s+\lambda^2}. \tag{2.8b}$$

Given the boundary conditions, the solution is

$$V(q,k,s) = \frac{c_1}{2c}\frac{c s_{2\mu}\cosh(c\tilde{z}) + s s_\lambda \sinh(c\tilde{z})}{s s_\lambda \cosh(c) + c s_{2\mu}\sinh(c)}, \tag{2.9}$$

where for brevity the notation $s_\kappa \equiv s+\kappa$ and $\tilde{z} \equiv 1-|z|$ is used. The distribution of horizontally-moving particle $H \equiv R+L$ follows from the solution to Eq. (2.2), giving

$$H(q,k,s) = \frac{k^2+(s+\lambda)^2}{q^2+(s+\lambda)^2} V(q,k,s), \tag{2.10}$$

from which $H(q,z,s)$ can be deduced explicitly. Note that $H(q,z,s)$ satisfies a boundary condition similar to Eq. (2.6), presumably because the only source of horizontally-moving particle is the population of vertically-moving particle. Finally, the distribution of particle within the slit, whatever their direction of motion, is $P(q,z,s)$, with $P = H+V$ and the distribution at the surface $\mathcal{W}(x,t)$ derived from Eqs. (2.5a)-(2.5b) is

$$\mathcal{W}(q,s) = \frac{V(q,w,s)}{s+2\mu}. \tag{2.11}$$

With $P(q,z,s)$ and $\mathcal{W}(q,s)$ known explicitly, one can check the conservation of particle number

$$\int_{-\infty}^{\infty}\mathrm{d}x \int_{-w}^{w}\mathrm{d}z\, P(x,z,t) + 2\int_{-\infty}^{\infty}\mathrm{d}x\, \mathcal{W}(x,t) = 1, \tag{2.12}$$

or in a equivalent manner $\lim_{q\to 0}\left[P(q,s) + 2\mathcal{W}(q,s)\right] = 1/s$, where $P(x,t)$ denotes the density integrated over the slit height.

[2] First, a symbolic computation software is used to solve the matricial system with the chosen initial conditions ($R_{\text{in}}(q,k) = 1/4$ and a similar result for L_{in}, U_{in} and D_{in}). Second, the equation of $f(k)$ is converted to a differential equation for $f(z)$ by using the properties of the Fourier transform.

Longitudinal Diffusion Coefficient If the long-time and large scale spreading behavior is diffusive, the expansion at small s and q has the form $P(q,s) \sim 1/(s+Dq^2)$. This is satisfied for P, $\mathcal{W}$ and the total distribution $T \equiv P + \mathcal{W}$ with the same coefficient D. An alternative route to the diffusion coefficient is to consider the second moment $M(t) = \int_{-\infty}^{\infty} \mathrm{d}x\, x^2 T(x,t)$. Its Laplace transform is $M(s) = -\lim_{q\to 0} \partial_{qq}^2 T(q,s)$ and the diffusion coefficient is $D = \lim_{s\to 0} s^2 M(s)/2$. Once all calculations are done, the final result for the longitudinal diffusion coefficient in dimensionless form is $D = 2\mu/\lambda(1+4\mu)$.

2.2.2 Extensions of the Model

Anisotropic Tumbling In contrast to the simplest version of RTP, real instances of motion in micro-organisms and cells exhibit reorientation events that are generally not anisotropic [45, 51, 56, 58, 59]. Accordingly, an extension of the model is considered, by introducing λ_f, λ_r and λ_s, the rate of tumbling in respectively forward, reverse and side direction. As an example, the evolution equation for the distribution of upward-moving bacteria $U(x,z,t)$ is now

$$\partial_t U = -\partial_z U - \lambda U + \lambda_\mathrm{f} U + \lambda_\mathrm{r} D + \lambda_\mathrm{s}(R+L). \tag{2.13}$$

Denoting as λ the total rate of tumbling and assuming no chirality in motion, one has $\lambda_\mathrm{s} = (\lambda - \lambda_\mathrm{f} - \lambda_\mathrm{r})/2$. The steps taken afterwards are similar to those described above for the isotropic case.

Motion at the Surface It has been assumed thus far that, until a successful escape occurs, the particle remains stationary at the wall. In this scenario, the surface behaviour is defined solely by the escape mechanism[3], which depends only on the escape rate μ. For bacteria, as discussed in Sec. 1.3.1, this escape rate may be linked to tumbling [11, 155] or other complex dynamics [117, 156, 157]. This assumption serves as a basic approximation for scenarios where microorganism-wall interactions result in residence, including trapping [110, 133], transient adhesion events [119], or surface-bound states [158]. However, if particles move on the solid boundary rather than being trapped, motion at the surface must be described explicitly to be accounted in the model. Displacement along the surface may also be relevant to a wide range of observed behaviors that include motion at solid interfaces [117, 118, 120, 122] (see Sec. 1.3.1). The four-direction model is not intended to capture the complex physics of these system-specific behaviors, but rather to account for simpler limiting cases. In this context, a natural and flexible assumption is that the particle at the wall move along the surface according to a one-dimensional run-and-tumble process, with parameters that may differ from those inside the slit. The following paragraph presents an analytical formulation of this surface motion within the framework of the four-direction model.

Let $\bar{v}$ and $\bar{\lambda}$ represent the velocity and tumbling rate at the surface. The evolution equations for the left-moving and right-moving surface particle distributions ($\bar{L}$ and $\bar{R}$

[3] In the four-direction model, detachment can only occur if particles move away in the direction normal to the surface, therefore there is only one possible direction in which particles can be oriented after detachment.

respectively) near the upper surface ($z = \omega$) are:

$$\partial_t \bar{R} = -\bar{v}\,\partial_x \bar{R} - (\bar{\lambda}' + \mu)\bar{R} + \bar{\lambda}'\bar{L} + S(x,t), \tag{2.14a}$$

$$\partial_t \bar{L} = +\bar{v}\,\partial_x \bar{L} - (\bar{\lambda}' + \mu)\bar{L} + \bar{\lambda}'\bar{R} + S(x,t), \tag{2.14b}$$

where $\bar{\lambda}' = \bar{\lambda}/2$. The source term $S(x,t) = U(x,w,t)/2$ represents the arrivals to the surface population from particles moving upward near the surface. The factor $1/2$ accounts for the equal probability of a particle choosing to move left or right along the surface upon impact. Switching to Fourier-Laplace variables, using the initial conditions $\bar{R}_{\text{in}} = \bar{L}_{\text{in}} = 0$, and solving the linear system yield a kernel $K(q,s)$ that relates the surface density to the incoming flux of particles:

$$K(q,s) \equiv \frac{U(q,w,s)}{\mathcal{W}(q,s)} = s + \mu + \frac{\bar{v}^2 q^2}{s + \bar{\lambda} + \mu}. \tag{2.15}$$

Following the steps outlined in Sec. 2.2.1, the generalized boundary condition for the vertically-moving particle distribution $V(q,z,s)$ is found to be:

$$\partial_z V\Big|_{z=w} = (s + \lambda - \lambda_{\text{f}} + \lambda_{\text{r}})\frac{\mu - K(q,s)}{\mu + K(q,s)} V\Big|_{z=w}, \tag{2.16}$$

while the surface distribution is given by:

$$\mathcal{W}(q,s) = \frac{V(q,w,s)}{\mu + K(q,s)}. \tag{2.17}$$

The resulting longitudinal diffusion coefficient in dimensionless form is:

$$D = \frac{2\mu}{\lambda(1-\alpha)(1+4\mu)} + \frac{\bar{v}^2}{(1+4\mu)(\mu+\bar{\lambda})}, \tag{2.18}$$

where $\alpha = (\lambda_{\text{f}} - \lambda_{\text{r}})/\lambda$ is the mean cosine of the turning angle.

Effective Rotational Diffusion The previous description assumes that directional changes arise solely from tumbling and surface collisions, and that runs in bulk, regardless of length, remain perfectly ballistic. However, for bacteria, cells, or artificial microswimmers, the persistence length is always finite due to thermal fluctuations and active noise from the surrounding medium and propulsion process. This results in a non-zero rotational diffusion, a feature that must be then incorporated within the model.

Although rotational diffusion is a gradual process, its impact at large length and time scales can be effectively included in the four-direction model by introducing instantaneous isotropic reorientation events that occur alongside tumbling events. These isotropic reorientations ensure a finite persistence length, even in the absence of tumbles. The rate of these instantaneous reorientations is given by $\tau_{\text{r}}^{-1} = D_{\text{r}}$, where D_{r} is an anlogous to the rotational diffusion coefficient, chosen such that the decay time of the orientational correlation function is consistent with the classical "continuous" Brownian noise. Since tumbling and effective rotational diffusion events are independent Poisson processes, they

can be seamlessly integrated into the four-direction model.
The only modification required is to adjust the rates λ_f, λ_r, and λ_s, which describe anisotropic tumbling. Specifically, for a run-and-tumble process with parameters λ and α, the modified values in the presence of effective rotational diffusion with rate τ_r^{-1} are[4]:

$$\lambda_\mathrm{mod} = \lambda + \tau_\mathrm{r}^{-1}, \qquad \alpha_\mathrm{mod} = \alpha \frac{\lambda}{\lambda + \tau_\mathrm{r}^{-1}}. \tag{2.19}$$

These relations will be useful in Sec. 2.3 and Sec. 2.4.

2.2.3 Main Result: Longitudinal Diffusion Coefficient

By combining the previous calculations, an exact solution for the longitudinal diffusion coefficient D is obtained, characterizing the long-time asymptotic dispersal along the slit direction (i.e., parallel to the slit walls). Despite being exact, the result is remarkably simple and can be expressed as:

$$D = \phi D_\mathrm{b} + \frac{\bar{\phi}\bar{D}}{1 + \mu/\bar{\lambda}}. \tag{2.20}$$

Here, D_b and $\bar{D}$ are the diffusivities in the case of bulk-only and surface-only motion, respectively. Specifically, $D_\mathrm{b} = v_\mathrm{o}^2/2\lambda(1-\alpha)$ represents the contribution from motion within the slit, while $\bar{D} = \bar{v}^2/\bar{\lambda}$ is the diffusion coefficient for one-dimensional motion at the surface (see Eq. 1.8). The terms ϕ and $\bar{\phi} \equiv 1 - \phi$ denote the fraction of particles in the slit and at the surface, respectively, when steady-state values are reached, with:

$$\phi = \frac{1}{1 + v_\mathrm{o}/2\mu W}. \tag{2.21}$$

Limiting Behaviors Several limiting cases can be checked from Eq. (2.20). For an infinitely wide slit ($W \to \infty$) or a reflecting surface ($\mu \to \infty$), the particle remains mostly within the slit, and the diffusion coefficient approaches its bulk value D_b, as expected. Conversely, for a quasi-absorbing boundary ($\mu \to 0$), the particle predominantly resides at the wall, and D converges to the surface value $\bar{D}$. To ultimately validate Eq. (2.20), motion according to four-direction model was reproduced numerically, as detailed in App. A.2.1. Diffusivity was measured across a wide range of motion parameter combinations, resulting in an excellent agreement between numerical data and the prediction of Eq. (2.20), with relative deviations typically below one percent.

While the focus is primarily on the longitudinal diffusion coefficient D, it is also of interest to examine the density profile $P(z,t)$ across the slit, disregarding the longitudinal position x of the particles. From $P(q,z,s)$ derived earlier, the expression $P(z,s) = \lim_{q\to 0} P(q,z,s)$ can be obtained. In the steady state, this yields:

$$P_\mathrm{st}(z) = \lim_{t\to\infty} P(z,t) = \lim_{s\to 0} sP(z,s) = \frac{2\mu}{1+4\mu}, \tag{2.22}$$

in dimensionless form. Similar to the confined Telegraph process, the density profile is flat. The fraction of particles in the slit is $\int_{-w}^{w} P_\mathrm{st}(z)\mathrm{d}z = 4\mu/(1+4\mu)$, which is the dimensionless form of Eq. (2.21).

[4] In particular, $\alpha_\mathrm{mod} = (\lambda_\mathrm{f,mod} - \lambda_\mathrm{r,mod})/\lambda_\mathrm{mod}$, with $\lambda_\mathrm{f,mod} = \lambda_\mathrm{f} + \tau_\mathrm{r}^{-1}/4$ and $\lambda_\mathrm{r,mod} = \lambda_\mathrm{r} + \tau_\mathrm{r}^{-1}/4$.

Beyond the Weighted Average Assumption A simple expectation for the diffusion coefficient of confined RTPs might be a weighted average of the bulk and surface diffusion coefficients, based on the fraction of particles in each region. However, Eq. (2.20) shows that this is not exactly the case. The discrepancy arises from the correction factor $(1 + \mu/\bar{\lambda})^{-1}$ in the second term of Eq. (2.20). This contrasts with other scenarios, such as Poissonian bimodal motions with alternating displacement types, where diffusion coefficients can be additive [159].

The additional factor reduces to unity only in the trivial cases where particles never leave the wall ($\mu \to 0$) or when surface motion becomes negligible due to frequent surface tumbling ($\bar{\lambda} \to \infty$). The deviation between Eq. (2.20) and a simple weighted average can be understood as a correction arising from the interplay between the escape process and the persistence of surface motion, particularly in the limit of a narrow slit. Notably, when $W \to 0$, the diffusion coefficient does not reduce to $\bar{D}$ but instead becomes $\bar{v}^2/(\bar{\lambda}+\mu)$, due to the influence of the additional factor. In a narrow slit, surface motion dominates, as particles spend most of their time at the wall. However, when an escape event occurs, it is effectively equivalent to a surface tumble[5], resulting in an effective surface tumble rate of $\bar{\lambda} + \mu$. Thus, the correction factor in Eq. (2.20) can be interpreted as an adjustment required in the case of extreme confinement.

2.3 Extension to a Continuous-Direction Model

Before exploring the implications of Eq. (2.20), it is essential to first evaluate its broader applicability. Given the simplifying assumption of constraining motion to only four directions, it is natural to question whether the results of the four-direction model can effectively describe more realistic RTP motions, which do not impose restrictions on the direction of motion and reintroduce classical rotational diffusion. This section addresses the issue by numerically studying the run-and-tumble motion within a slit for particles with continuous, rather than discretized, directions. The results will demonstrate that the diffusion coefficient predicted by the discrete model provides a good approximation for the continuous model, provided that effective parameters are appropriately chosen.

2.3.1 Simulations and Parameters

The "Continuous" Model A model of RTP motion without restrictions on the direction of movement is considered, referred to as the "continuous model" (see examples in Fig. 2.2). Its definition and parameters largely mirror those of the four-direction model, with two key differences. First, particle orientation is now governed by standard rotational diffusion, so its direction evolves continuously during a run, similar to an ABP. Second, when a particle escapes from the surface, its initial direction is randomly chosen from a uniform distribution of directions pointing inside the slit, regardless of the swimming strategy. Lastly, when a particle hits the wall, its subsequent direction of motion along the wall is chosen at random. While this behavior is not typically expected for bacteria on a smooth surface, it remains the simplest assumption for a generic model. These as-

[5] In the limit $W \to 0$, the particle encounters the opposite wall immediately after escaping. Since the direction of motion is randomized upon hitting the wall, the effect is equivalent to a surface tumble.

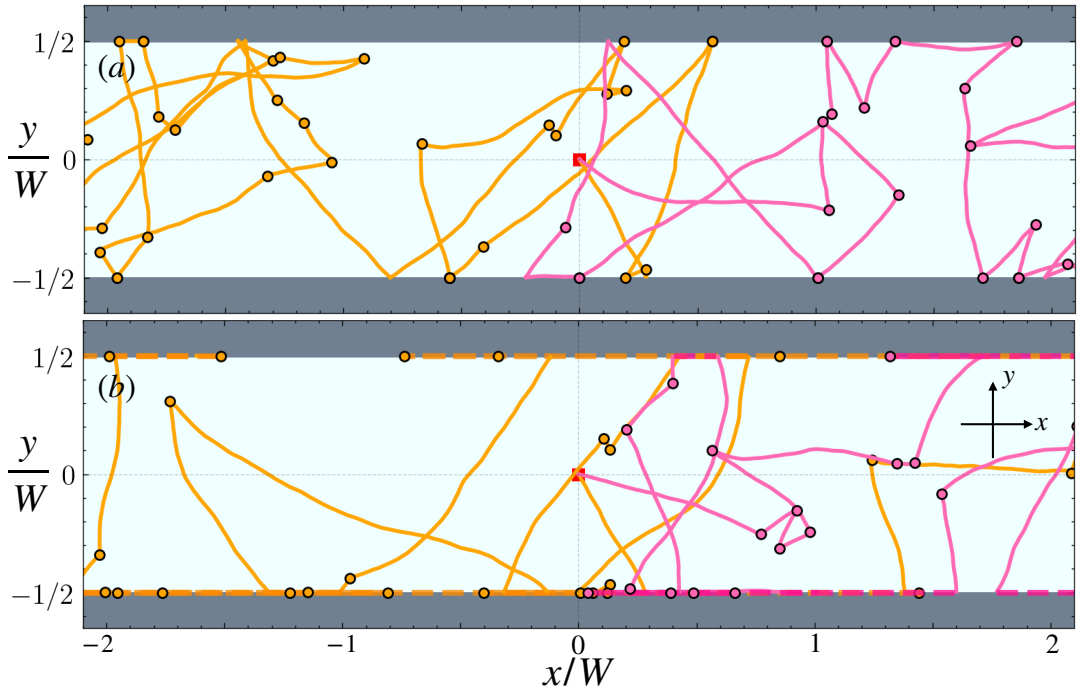

Figure 2.2: **Simulated motion within a slit.** (a) Two numerical tracks of "continuous" run-and-tumble motion occurring at speed v_o within a slit of width W, with no motion at the surface. Dots represent tumbles and escapes from the wall. Tumbling and escape rates are $\lambda = T_s^{-1}$ and $\mu = 0.5T_s^{-1}$, respectively, while rotational noise is $D_r = 0.1T_s^{-1}$. (b) Two trajectories with surface motion included, where dotted lines indicate movement occurring at the surface. Same parameters as in (a), with added surface velocity $\bar{v} = v_o$ and surface tumbling rate $\bar{\lambda} = 0.5T_s^{-1}$. The time unit is $T_s = W/v_o$.

sumption maintains consistency with the four-direction model and serves as the simplest choice for a generic model.

Simulation Methods To characterize the transport of a continuous RTP in confinement, simulations were performed. The particle's equation of motion were integrated numerically using an Euler-Maruyama algorithm with a time step of $10^{-2}\,T_s$, to produce trajectories that typically last $10^5\,T_s$. Here, $T_s \equiv W/v_o$ is defined as the characteristic time to cross the slit and is used as the unit of time, with the slit width W serving as the unit of length. No additional units are required as the description is purely kinematic. Sample trajectories are shown in Fig. 2.2, for cases both with and without surface motion. The longitudinal diffusion coefficient D (i.e., the diffusion coefficient along the x direction, parallel to the confining walls) is obtained by fitting the asymptotic slope of the x-component of the mean-squared displacement, following the procedure outlined in Annex A.1.3. For each set of parameters, the reported diffusion coefficient is the average over 10 independent trajectories. A comprehensive error analysis and numerical validation of the simulation procedure is provided in Appendix A.

Numerical Exploration A systematic exploration of the parameter space was performed. With W, T_s, and v_o normalized to one by the choice of units, the model still

Parameter	Symbol	Unit	Min.	Max.	n
Bulk tumbling rate	$\hat{\lambda}$	T_s^{-1}	0.05	50	8
Surface tumbling rate	$\hat{\hat{\lambda}}$	T_s^{-1}	0.05	50	8
Escape rate	$\hat{\mu}$	T_s^{-1}	0.05	50	8
Rotational diffusion coefficient	$\hat{D}_\mathrm{r}$	T_s^{-1}	1/3	3	5
Surface velocity	$\hat{\hat{v}}$	v_o	0	1.5	4
Mean cosine of turning angle	$\hat{\alpha}$	-	-1	0.375	3

Table 2.1: Parameters of the continuous model and range explored in simulations. Indicated are the minimum and maximum values, as well as the total number n of values considered. Values for $\hat{\lambda}$, $\hat{\hat{\lambda}}$, $\hat{\mu}$ and $\hat{D}_\mathrm{r}$ are equally spaced on a logaritmic scale, whereas values for $\hat{\hat{v}}$ are equally spaced in linear scale.

involves six parameters: the tumbling rates in the slit and at the wall ($\hat{\lambda}$ and $\hat{\hat{\lambda}}$), the escape rate $\hat{\mu}$, the rotational diffusion coefficient $\hat{D}_\mathrm{r}$, the velocity at the wall $\hat{\hat{v}}$, and the swimming pattern, represented by the parameter $\hat{\alpha}$. For clarity and future reference, all parameters of the continuous model are indicated with a circumflex symbol. As shown in Tab. 2.1, each parameter was varied over a wide range, covering up to three orders of magnitude. The three swimming patterns considered are based on bacterial behavior [62]: run-reverse, isotropic run-and-tumble, and run-and-tumble with reorientation events that replicate *E. coli*'s turning angle distribution[6]. The corresponding α parameters are -1, 0, and 0.375, respectively.

The simulation data is divided into two subsets. The first subset assumes no motion at the wall and includes 960 parameter combinations, all of which were simulated. The second subset incorporates motion at the wall, which adds two additional parameters, leading to a total of 23,040 possible cases. To maintain computational feasibility, only 1,040 cases were sampled at random from the parameter space. In total, the data set for diffusion coefficients includes 2,000 parameter combinations.

2.3.2 Effective Parameters

After simulating motion across a wide range of parameter combinations and measuring diffusivity, the next step is to compare the simulation data with the predictions obtained using the minimalistic approach of the four-direction model. Initially, when equating the parameters of the discrete model to those of the continuous model and applying Eq. 2.20, the agreement is poor, with relative deviations between predictions and simulations typically around 25% and reaching up to 40% (not shown). However, as will be demonstrated, a small adjustment in how the parameters are linked between the two models significantly improves the accuracy of the predictions.

Effective Escape Rate First, consider the fraction of particles moving within the slit. According to the four-direction model and Eq. (2.21), this quantity depends solely on the escape rate μ. As shown in Fig. 2.3, the numerical results for $\hat{\phi}$ in the continuous

[6]Specifically, turning angles are sampled for a distribution following Eq. [2] of Ref. [89], with parameters taken from Fig. 3 of the paper.

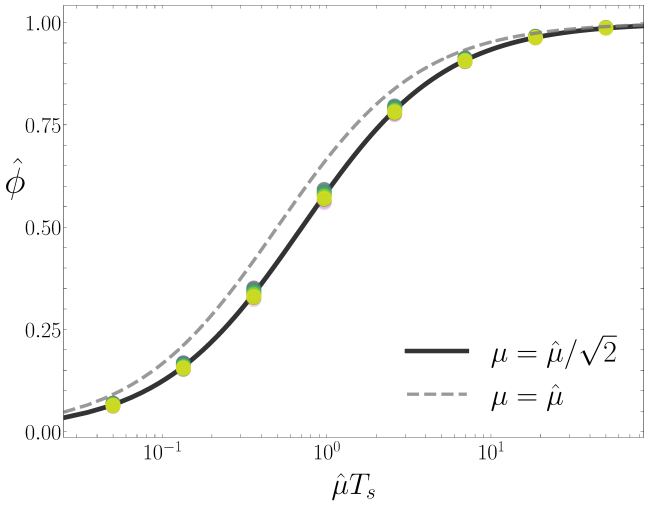

Figure 2.3: **Effective escape rate.** Fraction of particles within the slit as a function of surface escape rate. Dots show the simulation data for all parameter combinations considered. Curves show the four-direction model predictions of Eq. (2.21), with an escape rate that is uncorrected (dashed line) or effective (continuous line). Time unit is $T_s = W/v_o$.

model, across all parameter considered, are consistent with this prediction: they show a strong dependence on the escape rate $\hat{\mu}$ and little to no dependence on other parameters. However, significant deviations between simulation and prediction occur when keeping the identity $\mu = \hat{\mu}$ (dashed line). A quantitative match can be achieved by introducing a correction, $\mu = \hat{\mu}/a$. A fit to the numerical data yields $a \simeq 1.4$ (solid line), and as detailed in App. A.2.2, a heuristic argument suggests $a = \sqrt{2}$, a value adopted hereafter.

Effective Rotational Noise Consider now the longitudinal diffusion coefficient. Simulation results, shown in Fig. 2.4a, present rescaled numerical estimates of diffusivity as a function of the tumbling rate λ, for fixed values of D_r and μ. Despite the correction to the escape rate, the agreement between simulations and theoretical predictions remains unsatisfactory, especially at low tumbling rates (dotted lines). This suggests that the issue could be rotational noise, which becomes dominant when the tumbling rate is low. Additionally, given the different models of rotational diffusion in the continuous and discrete models (one following classical Brownian motion, the other based on effective isotropic tumbling), the equality of D_r and $\hat{D}_r$ is called into question. Consequently, D_r is treated as a free parameter, and Eq. (2.20) is fitted to all numerical diffusion estimates[7]. The fitting results for the effective rotational diffusion coefficient D_r are shown in Fig. 2.4b as a function of $\hat{D}_r$, across all tested data[8]. The relationship is remarkably simple, involving only a constant shift: $D_r = \hat{D}_r + c$, with $c \simeq 0.4$ in units of T_s^{-1}. This correction results in accurate agreement, as illustrated in Fig. 2.4a (continuous line), where theoretical predictions align with numerical data over the entire range of λ. Although shown here only for two curves, this agreement holds across all the parameters tested.

Why is a Correction Needed? The origin of the additive correction to rotational diffusion can be qualitatively understood. In the four-direction model, a particle arriving at or escaping from the wall moves perpendicular to it, retaining perfect memory of

[7]Specifically, for fixed values of α and μ, the numerical data for $D(\lambda)$ is fitted with D_r as a free parameter.

[8]Here, 960 parameter combinations are considered where the particle is motionless at the wall. The case with wall motion cannot be similarly treated due to random parameter sampling. However, the correction applies since it is independent of wall motion.

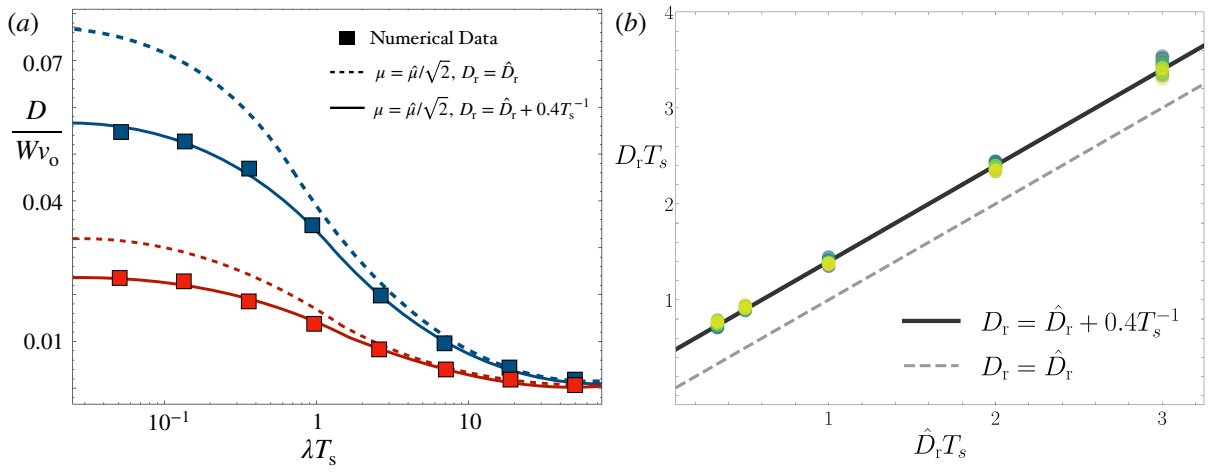

Figure 2.4: **Effective rotational noise.** (a) Numerical estimates of diffusivity (squares) vs. bulk tumbling rate λ. Here, $\hat{D}_\mathrm{r} = T_\mathrm{s}^{-1}$ and $\hat{\bar{v}} = 0$ are fixed, while $\hat{\mu} = 0.1$ and 0.5 for the red and blue data, respectively. Continuous and dotted lines represent predictions of the four-direction model, with and without the correction for rotational noise. (b) Effective rotational diffusion coefficient D_r as a function of bare coefficient $\hat{D}_\mathrm{r}$. Dots show values of D_r obtained by fitting simulation data of the continuous model with the analytical prediction of the discrete model. The particle is motionless at the wall. Lines correspond to linear regression.

its direction of motion, except during reversals. In the continuous model, however, the direction chosen upon escape is randomized, leading to a loss of directional memory. This loss acts as a localized source of rotational diffusion, governed by the inverse crossing time $T_\mathrm{s}^{-1} = v_\mathrm{o}/W$, and disappears in the case of an infinitely wide slit. The constant $c = 0.4$ is intriguingly close to $4/\pi^2$, a value adopted for convenience, though a clear justification for this choice remains elusive[9].

Effective Parameters In light of the data analysis, it is proposed that the diffusion coefficient of the continuous model can be described by the discrete model prediction from Eq. (2.20), combined with the following effective parameters:

$$\mu = \hat{\mu}/\sqrt{2}, \tag{2.23a}$$

$$D_\mathrm{r} = \hat{D}_\mathrm{r} + c v_\mathrm{o}/W, \qquad c \equiv 4/\pi^2. \tag{2.23b}$$

No corrections are necessary for other parameters. To evaluate the predictive accuracy of this approximation, it was tested on the entire simulation data set. Figure 2.5 shows the distribution of relative deviations δ between the prediction and the simulation data. Across all parameter combinations, the relative deviation never exceeds 10% and remains below 5% in 95% of cases. This result holds both with and without motion at the wall. It is concluded that, with the use of effective parameters, the analytical approach of

[9]The factor $2/\pi$ recurs throughout this problem, as discussed in App. A.2.2. For instance, consider a particle arriving at the wall with angle θ and leaving with angle θ', as illustrated in Fig. A.5. Assuming both angles are isotropically distributed, the orientation correlation, given by the average of $\cos(\theta' - \theta)$, results in $4/\pi^2$.

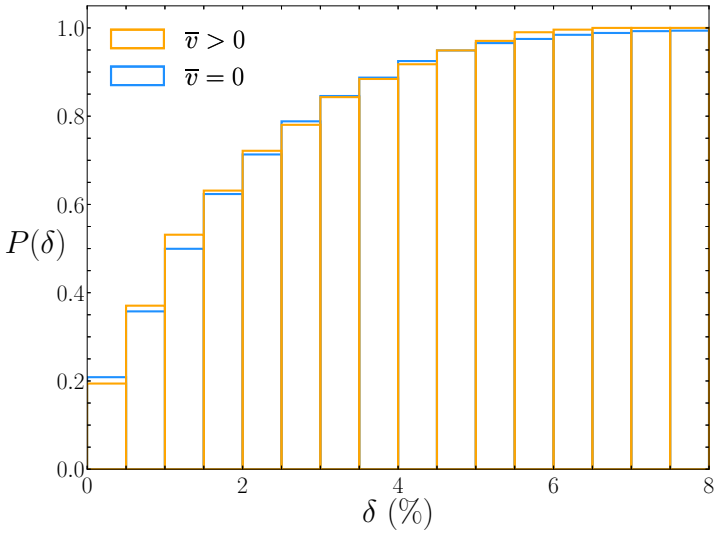

Figure 2.5: **Accuracy of predicting the continuous-direction results.** Cumulative distribution of relative deviation δ between the diffusion coefficient from prediction (four-direction model) and simulations (continuous-directions). Shown are the cases without and with surface motion ($\bar{v} = 0$ and $\bar{v} > 0$ respectively). Predictions are made including the parameter corrections (Eqs. 2.23a-2.23b).

the four-direction model provides an approximate yet reliable prediction for the diffusion coefficient of a continuous run-and-tumble particle in confinement.

2.4 Maximizing the Diffusion Coefficient

This section builds on the model developed in Sec. 2.2, which was validated and extended by the results in Sec. 2.3. Here, the model will be used to identify and understand the conditions under which long-time exploration is most efficient. For simplicity, the four-direction model is used to provide analytical insight, and implications for the continuous model can be deduced by transitioning from bare to effective parameters.

2.4.1 Optimal Mean Run-Time

This section examines whether dispersal along the slit can be maximized through an appropriate choice of run time τ. This question is relevant for microorganisms whose run-and-tumble dynamics may be influenced by environmental conditions [160], as well as for artificial micro-swimmers, or for micro-robots whose navigation strategies have to be optimized. Throughout Sec. 2.4.1, the mean run time τ is treated as the variable parameter, while the slit width W and swimming velocity v_o remain fixed. For simplicity, W and v_o are taken as the unit of length and unit of velocity, respectively, making the crossing time $T_s \equiv W/v_o$ the unit of time.

Without Surface Motion

The analysis begins with the simplest case, where the particle remains stationary when at the surface ($\bar{v} = 0$). The tumbling rate is $\lambda = \tau^{-1}$. For the escape rate μ, a value inspired by the behavior of real microorganisms is selected. A natural assumption is that escape occurs only through tumbling, leading to $\mu = (\eta\tau)^{-1}$, where the prefactor $\eta \geqslant 1$ represents the average number of tumbles required for a successful escape. The longitudinal diffusion

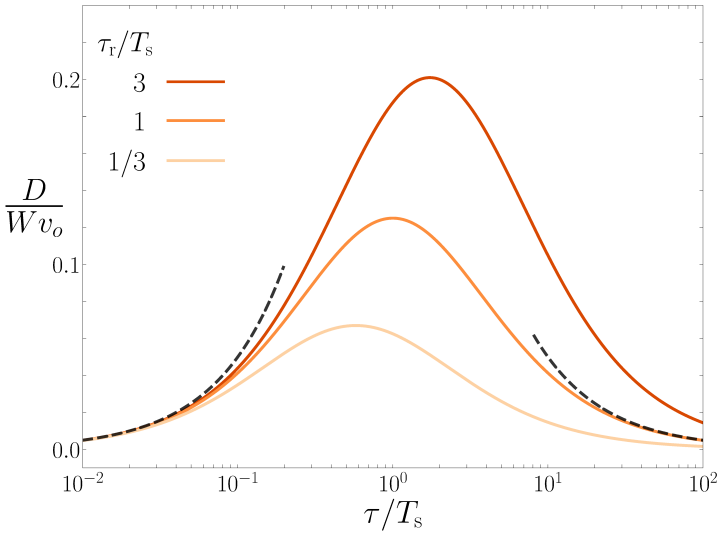

Figure 2.6: **Diffusivity vs. mean run-time.** Shown for different rotational diffusion times. Particles are motionless at the wall ($\bar{v} = 0$), $\eta = 2$ and $\alpha = 0$. Unit time is $T_s \equiv W/v_o$. The dashed lines show the lowest order limiting behavior predicted from Eq. (2.25) for small and large τ.

coefficient in dimensionless form is then given by:

$$D = \frac{\tau}{\alpha'(\eta\tau + 2)}, \tag{2.24}$$

where $\alpha' \equiv 1 - \alpha$ is introduced for brevity. The function $D(\tau)$ increases monotonically and reaches a plateau at large τ. This behavior can be understood as follows: as $\tau \to \infty$, the fraction ϕ of particles within the slit decreases as $\phi \sim \tau^{-1}$, while the bulk diffusion coefficient increases as $D_b \sim \tau$, resulting in a limiting constant value for D. Therefore, transport is most efficient for a vanishing tumbling rate, assuming perfectly ballistic motion during runs.

Including Rotational Noise However, for any micro-organism, pure ballistic motion is unrealistic, and as discussed in Sec. 2.2.2, rotational diffusion can be considered in the model to have a more realistic description. Therefore, unless otherwise stated, a finite rotational diffusion with characteristic time $\tau_r = D_r^{-1}$ is assumed from this point onward. Using the modified parameters from Eq. (2.19) in conjunction with Eq. (2.20) results in the following expression for the diffusion coefficient:

$$D = \frac{\tau\tau_r}{(\tau + \alpha'\tau_r)(\eta\tau + 2)}. \tag{2.25}$$

As shown in Fig. 2.6, the diffusion coefficient now exhibits non-monotonic behavior with respect to the mean run time τ. A maximum D_m is reached at an optimal mean run time τ_m, given by:

$$\tau_m = \sqrt{2\alpha'\tau_r/\eta}, \quad D_m = \frac{\tau_r}{2 + 2\sqrt{2\alpha'\eta\tau_r} + \alpha'\eta\tau_r}. \tag{2.26}$$

Interpretation and Limiting Cases The rationale for this maximum is as follows: In the limit of frequent tumbling ($\tau \to 0$), the particle primarily remains within the slit, and the diffusion coefficient approaches its bulk value, $D \simeq \tau/2\alpha' \sim \tau$, which increases with τ. Conversely, in the limit of rare tumbling ($\tau \to \infty$), the particle mostly stays at the wall, and infrequent excursions into the slit result in limited displacement due to

rotational diffusion, leading to $D \simeq \tau_r/\eta\tau \sim \tau^{-1}$, which decreases with τ. These two limiting behaviors are separated by a maximum in the diffusion coefficient. For the maximum value D_m, two regimes emerge, separated by a rotational time $\tau_r^* \equiv 2/\alpha'\eta$. When $\tau_r \ll \tau_r^*$, the maximum $D_m \simeq \tau_r/2$ is controlled by rotational diffusion. When $\tau_r \gg \tau_r^*$, the maximum $D_m \simeq 1/\alpha'\eta$ is governed by the escape process at the wall. Finally, in the limit of high rotational persistence ($\tau_r \to \infty$), the maximum becomes less pronounced and shifts towards longer run times, approaching the plateau behavior predicted by Eq. (2.25) for pure ballistic motion.

In conclusion, this analysis shows that long-time dispersal in a slit, without surface motion, is maximized by selecting a finite mean run time that depends not only on the slit crossing time but also on the rotational diffusion, the swimming pattern, and the wall escape efficiency.

With Surface Motion

When the particle remains mobile at the slit boundary, the maximum in diffusion coefficient reached at a finite τ_m may disappear. Keeping λ and μ as above, we fix $\bar{\lambda} = \lambda - \mu$. With such a choice, reorientation events occur at surfaces with the same frequency as in the slit and may result in escape, with rate μ, or in surface tumble, with rate $\bar{\lambda}$. The diffusion coefficient in dimensionless form is

$$D = \frac{\tau\tau_r\left[\tau + \tau_r + \eta\bar{v}^2\tau(\tau + \alpha'\tau_r)\right]}{(\tau + \tau_r)(\tau + \alpha'\tau_r)(\eta\tau + 2)}. \tag{2.27}$$

It turns out that there is a critical velocity $\bar{v}_c$ which separates two regimes, illustrated in Fig. 2.7. For $\bar{v} < \bar{v}_c$, there is a maximum at finite τ_m whereas for $\bar{v} > \bar{v}_c$, the highest value is reached for an infinite run time[10]. In other words, for slow wall motion, optimal transport requires a finite run time whereas for fast wall motion, it is advantageous to eliminate tumbling entirely.

Evolution of the Maximum The dependence of τ_m near the critical velocity $\bar{v}_c$ may follow two distinct scenarios. In the first scenario, visible in Fig. 2.7(a), there is an absolute maximum whose location continuously shifts to higher τ_m, leading to a function $\tau_m(\bar{v})$ that diverges at $\bar{v}_c$. In the second scenario, illustrated in Fig. 2.7(b), there is at the critical velocity a local maximum whose height equates the plateau reached for $\tau_m \to \infty$. In this case, $\tau_m(\bar{v})$ remains finite for $\bar{v} < \bar{v}_c$, before jumping discontinuously at $\bar{v}_c$ to an infinite value. Note that if one defines τ_m^{-1} as an order parameter, the first and second scenarii are reminiscent of second and first-order transition respectively. Because the optimal mean run time τ_m obeys a fourth-order equation, it can not be written explicitly in the general case. Appendix A.2.3 presents a few cases where approximations are possible.

2.4.2 Monotonous Dependence on Slit Width

This section examines how exploration in a confined environment is affected by the slit width for a particle with a fixed motility strategy. Unlike the mean run time, the diffusion

[10] In the limit $\tau_m = \infty$, the diffusion coefficient is $D = \tau_r\bar{v}^2$, a value controlled by the rotational diffusion and surface velocity.

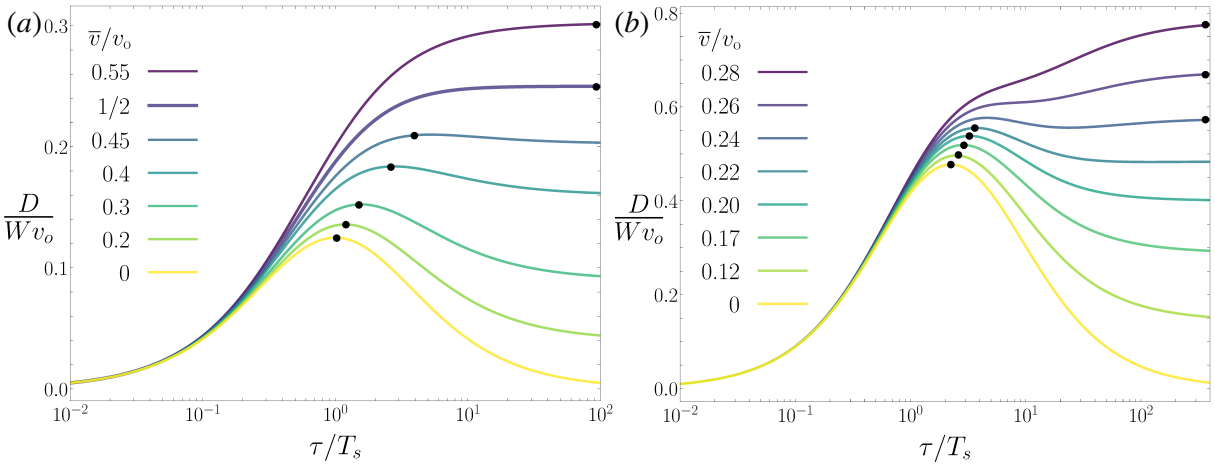

Figure 2.7: **Diffusivity vs. mean run-time, including surface motion.** In both panels, black dots indicate the position of the maximum (the dot on the right edge signifies that the maximum occurs at infinity). (a) First scenario: The critical value at which the maximum disappears is $\bar{v}_c = v_o/2$, as given by Eq. (A.10). Parameters are $\eta = 2$, $\tau_r = 1$, and $\alpha = 0$. (b) Second scenario: For $\bar{v} < \bar{v}_c \simeq 0.24\, v_o$, the maximum is reached at a finite τ. For $\bar{v} > \bar{v}_c$, the highest value is attained in the limit $\tau \to \infty$. Parameters are $\eta = 2$, $\tau_r = 10$, and $\alpha = 1/2$.

coefficient's dependence on slit width is always monotonous, ruling out the possibility of a maximum. However, the slope of the $D(W)$ function can change sign at a critical value $\bar{v}^*$, given by:

$$\frac{\bar{v}^*}{v_o} \equiv \sqrt{\frac{\tau + \tau_r}{2(\tau + \alpha'\tau_r)}}. \tag{2.28}$$

When $\bar{v} = \bar{v}^*$, the slit width has no effect on the longitudinal diffusion. For $\bar{v} < \bar{v}^*$, diffusion reaches its maximum when $W \to \infty$, with $D = D_b$. Conversely, for $\bar{v} > \bar{v}^*$, the highest diffusion occurs when $W \to 0$, with $D = \bar{v}^2/(\tau^{-1} + \tau_r^{-1})$. These two regimes are illustrated in Fig. 2.8. Somewhat counterintuitively, even though surface displacement is slower than in the interstitial space, spreading may be enhanced in a narrow slit. This is because motion along the surface is one-dimensional, leading to more efficient exploration along the slit.

2.4.3 Optimal Transport for Real Microswimmers

This section focuses on how the previous results can be applied to develop an optimality criterion, relevant for real-world scenarios. To examine the conditions required for maximal transport, it is assumed that there is no motion at the wall, a choice justified by several factors. First, the maximum diffusion is known explicitly in this case, simplifying the analysis. More importantly, while perfectly flat and smooth walls are often used in laboratory experiments, such surfaces may be less common in natural settings. As explained in earlier sections (See for instance Fig. 1.6), natural porous environments often have irregular, rough, or fuzzy boundaries, which are likely to impede surface motion.

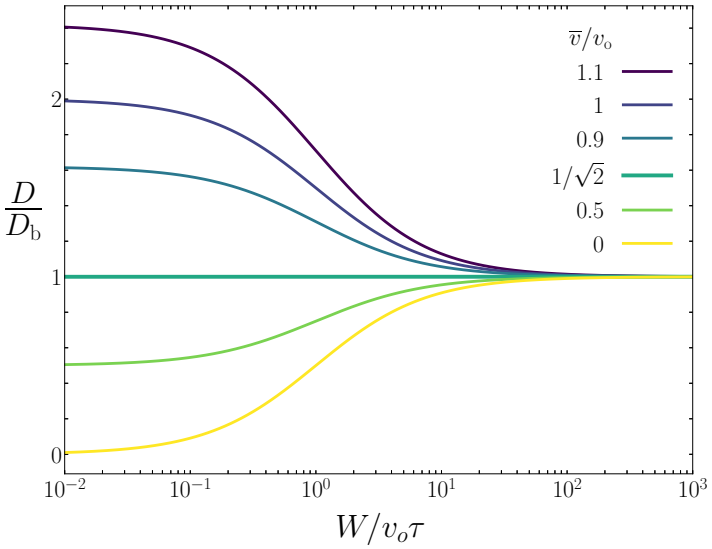

Figure 2.8: **Diffusivity vs. confinement size.** Diffusivity curves are shown for several surface velocities. The particular velocity where diffusion is independent of width is $\bar{v}^*/v_o = 1/\sqrt{2}$. Parameters are $\alpha = 0$, $\tau_r = 1$ and $\eta = 2$.

Given these assumptions, the optimal mean run time τ_m in a slit of width W is:

$$\tau_m^2 = \frac{\sqrt{2}(1-\alpha)}{\eta}\left[1 + c\frac{\tau_r v_o}{W}\right]^{-1}\frac{\tau_r W}{v_o}, \tag{2.29}$$

which is derived from Eq. (2.26) and the effective parameters from Eqs. (2.23a)-(2.23b). Depending on the ratio between τ_r and the crossing time $T_s \equiv W/v_o$, two limiting cases arise. For $\tau_r \ll T_s$, where orientation is lost before the particle can cross the slit, $\tau_m \sim \sqrt{\tau_r T_s}$ is the geometric average of the rotational and crossing times. For $\tau_r \gg T_s$, indicating quasi-ballistic motion at the slit scale, τ_m is proportional to the crossing time, and the optimal mean run length $l_m \equiv v_o\tau_m$ is given by:

$$\frac{l_m}{W} = \sqrt{\frac{\sqrt{2}(1-\alpha)}{c\eta}}. \tag{2.30}$$

Unless escape by tumbling is highly inefficient and η very large, the l_m/W ratio is typically of order unity. When rotational diffusion is negligible, the optimal longitudinal transport occurs when the mean run length is comparable to the confinement size. Intuitively, runs should be long enough to efficiently explore the slit but short enough to avoid excessive time spent near the wall.

Though the four-direction model captures only general features, its predictions are interesting to evaluate in real systems. Since the motility strategies of microorganisms are typically fixed, the question becomes: in what confined environment would these motions be optimal for bacteria and cells?

Bacteria For *E. coli*, typical parameters are $\tau_m = 1\,\mathrm{s}$, $\tau_r = 2.5\,\mathrm{s}$[11], $\alpha = 1/3$, $v_o = 30\,\mu\mathrm{m\,s^{-1}}$, and $\eta = 3$, giving $l_m/W \simeq 0.5$. More generally, a range of values representative of bacterial motion can be considered: $\tau_m = 0.3-1\,\mathrm{s}$, $\eta = 2-4$ [11,82], $v_o = 20-40\,\mu\mathrm{m\,s^{-1}}$, and α between -1 and $1/2$. The l_m/W ratio spans a range of $0.3-1.7$, remaining on the

[11]Here, $\tau_r = 1/2D_r$ for three-dimensional systems, with $D_r = 0.2\,\mathrm{s^{-1}}$ [82].

order of unity, consistent with the prediction from Eq. (2.30). The corresponding slit size ranges from $W = 3 - 120\,\mu\text{m}$, which is relevant to several bacterial habitats. Micropores in mature biofilms [161], fibronectin and collagen gels [133,162], and sandstone, sand, and soil aggregates [100] often fall within the $1 - 100\,\mu\text{m}$ range.

Cells Though less commonly used, the RTP model offers a general framework to describe cell movement. A common motility strategy among eukaryotic cells is amoeboid crawling, where cells extend pseudopodia, which can be modeled as effective tumble events [8, 163, 164]. Although more challenging to characterize than bacterial motion, the $\tau_\text{m}/\tau_\text{r}$ ratio for cells appears to be higher, and for simplicity, is set to unity here. With $\eta = 2 - 4$, $\alpha = 0$, a velocity of $v_\text{o} = 1 - 5\,\mu\text{m}\,\text{mn}^{-1}$, and $\tau_\text{m} = 5 - 20\,\text{min}$ [165, 166], the l_m/W ratio is below unity, falling in the range $0.3 - 0.6$. The optimal confinement size for such motion is $8 - 300\,\mu\text{m}$, relevant to bodily environments such as interstitial spaces and ducts.

Comparison with Earlier Results in Literature

The optimal transport criterion can also be compared with earlier findings in related contexts. Kurzthaler *et al.* [21], discussed in Sec. 1.4.2, examined the diffusivity of active polymers moving in disordered porous media made of randomly placed overlapping spheres. The study found that the diffusion coefficient is maximized when the mean run length satisfies $l_\text{m} = \mathcal{O}(1)L_\text{c,max}$, where $L_\text{c,max}$ is the maximum chord length of free space, typically six times the average pore size (see Fig. 1.9b). Unlike the prediction in Eq. (2.30), the optimal mean run length is several times larger than the characteristic pore size. This difference could be expected, given the distinct systems considered. Kurzthaler *et al.* examined active polymers with sizes comparable to the pores, moving through highly disordered media. In contrast, the current study focuses on point particles in a simpler geometry.

Beyond bacteria-inspired motility, a recent study introduced the "reverse-when-stuck" strategy [128], where reversal occurs when movement is blocked by an obstacle, requiring the ability to sense velocity. Simulations suggest that this strategy outperforms others (see Fig. 1.4.2c). Is the reverse-when-stuck strategy also effective in a slit? The answer is yes, as shown by analytical considerations. Up until now, the escape rate μ has been governed by the tumbling rate, but within this framework, it can be treated as a free parameter. Focusing again on the case without surface motion, Eq. (2.20) indicates that the diffusion coefficient increases with μ, reaching its maximum when $\mu \to \infty$. This conclusion holds for the continuous model as well[12]. Physically, this limit corresponds to a particle escaping the wall immediately after contact, striking an optimal balance by avoiding tumbles while minimizing time spent at the wall.

[12] In our model, the escape direction is isotropically distributed, which differs from the specific reversal event considered in Ref. [128].

2.5 Conclusion and Perspectives

Summary In summary, this chapter presented a coarse but generic model capable of capturing the long-time diffusive spreading of run-and-tumble motion confined within a two-dimensional planar slit. By first simplifying the motion to discrete directions, an exact solution for the diffusion coefficient was derived. This prediction was then tested and shown to be relevant even for motions without directional constraints when effective parameters were used. This result was confirmed through simulations across a wide range of conditions. Furthermore, the validated model was used to identify optimal motion properties that maximize transport. When surface motion is negligible, the optimal mean run time is often comparable to the confinement size, suggesting that the motility patterns of bacteria and cells may be particularly efficient in some natural porous environments.

Perspectives

The proposed optimality criterion was derived under several simplifying assumptions. However, the model has broader applicability and could yield different criteria under other conditions. For example, parameters such as wall velocity [167] could depend on channel width. Additionally, it was assumed throughout most of the discussion that wall escape occurs via tumbling, a reasonable assumption for idealized bacterial motion. However, certain bacteria and other microorganisms or cells may employ distinct escape mechanisms. Given the generic nature of the model, the effects of these mechanisms can still be explored by appropriately adjusting the escape rate.

Several aspects of confined run-and-tumble motion were excluded from this description but warrant further investigation. First, both tumbling and escape events were modeled as Poissonian processes. As shown by power-law distributions in run and trapping times [12], non-Poissonian processes are also relevant, though they generally make theoretical treatment more complex [90]. Second, specific surface behaviors, such as hydrodynamics-induced circling trajectories, might also need to be considered. Including these effects would make the model more realistic, though applicable to a narrower class of systems. Finally, in contrast to the simple geometry considered here, many natural porous environments are disordered. The influence of disorder on the optimality criterion remains to be fully characterized, but this issue will be a main point of investigation in the following Chapter of the thesis.

From a broader perspective, run-and-tumble motion in confined media belongs to the class of coupled bulk-surface transports. Even in purely diffusive systems [168], such phenomena can exhibit unexpected properties [169] and offer significant opportunities for optimization, such as minimizing reaction time [170]. Unlike Brownian motion, which is characterized by a single quantity—the diffusion coefficient—motility strategies of microorganisms involve many parameters and exhibit a wide range of behaviors. Understanding how this flexibility can be leveraged to ensure optimal transport in various environments remains an open question.

CHAPTER 3

Universal Dispersal of Motile Microorganisms in Porous Media

Contents of this Chapter

This chapter presents work submitted on October 10, 2024, which is currently under review. The research results from a collaboration supported by the European Training Network "Phymot", in partnership with Riccardo Foffi and Roman Stocker at Institute of Environmental Engineering of ETH Zurich.

3.1 Introduction

Motivation and Scope In Chapter 2, the focus has been on the dispersal of microswimmers within slit-like microstructures, modeled as run-and-tumble motion within two parallel infinite walls. As previously discussed, the slit is arguably the simplest form of confinement, defined only by a single parameter: the distance between the walls.

Nevertheless, Chapter 2 demonstrated that even this relatively simplified scenario poses significant analytical complexity, requiring the introduction of discretized motion directions to be fully solvable. In contrast, Sec. 1.3 explored real bacterial habitats, where confinement is rarely as simple as a planar slit. Instead, these environments typically involve heterogeneous and disordered obstacles (see, for instance, Fig. 1.6). These considerations motivate the present work. The results of Chapter 2 underscored the value of a model capable of accurately predicting diffusivity, as it allowed for the rationalization of the relationship between diffusivity, motion, and environmental parameters, thereby identifying optimality criteria for motion. The primary goal of this chapter is to replicate and extend the results of Chapter 2 to porous media, *i.e.*, environments where obstacles of arbitrary shapes are distributed in space.

A Vast Parameter Space This extension presents a significant challenge: the vast diversity in natural microstructures implies a potentially infinite variety of confining geometries that should be considered. This diversity makes it challenging to define a universal "porous medium" model that accurately represents the broad spectrum of natural habitats, where pore morphologies can be very diverse, with sizes that range from micrometers to millimeters [171]. This complexity is further compounded by the variety of motions typically exhibited by microorganisms (see Sec. 1.1.1) and the wide range of behaviors they display when interacting with solid boundaries (see Sec. 1.3.1).

Linking to Existing Research and Knowledge Gaps These challenges align with the current research landscape outlined in Sec. 1.4.2. Despite a recent increase in studies on both non-tumbling [127,139,172,173] and tumbling microorganisms [12,20,21,118,128–130,143,174] within confined settings, the uncertainty regarding whether the insights from idealized porous media can be applied to the diversity of natural microstructures remains a critical challenge. Furthermore, few general principles have emerged, as most studies rely on system-specific assumptions or simplified formulations. One notable exception is the observation across different systems of an optimal persistence time at which dispersal is maximized [20–22,128,131], a result that also aligns with the findings of Chapter 2 [143]. However, no overarching theory exists to predict this maximum across different systems.

In this context, an interesting hypothesis has been put forward in a pre-print by Mattingly [131], which suggests that the specific details of the porous microstructure can be "largely forgotten", suggesting that only a small set of environmental features significantly influences dispersal. However, the generality and applicability of this claim remains unclear, as it was derived from a specific microstructure and swimmer model[1].

Summary and Main Findings The work presented in this chapter investigates the dispersal of motile microorganisms in porous media. Similar to Chapter 2, the focus is on run-and-tumble microorganisms, which stop moving upon encountering a solid surface

[1]Point-like run-and-tumble particles moving within a two-dimensional porous medium consisting of overlapping randomly placed disks

but can escape through tumbling. However, unlike Chapter 2, which began with theory that is later tested by simulations, this chapter begins with a purely numerical exploration across different combinations of microstructures and swimming strategies. The results of the numerical exploration suggest that dispersal may universally depend on the mean run time, regardless of both the specifics of the microstructure or the swimming strategy. This finding is then explained by a simple theoretical framework, which is able to predict diffusivity across all cases tested. The model also rationalises the key insight from Mattingly [131] that much of the microstructure's complexity can be "forgotten", the key being the invariance of the mean free path [175, 176], also known as Cauchy universality [177].

Outline of the Chapter The chapter is organized as follows: Sec. 3.2 begins with a numerical investigation of dispersal across diverse microstructures and swimming strategies, identifying a universal relationship between dispersal and mean run time. Sec. 3.3 introduces an analytical model that combines the RT analytical framework for bulk diffusivity with Cauchy universality, and then compares it to both the numerical data and previous results from the literature. Finally, Sec. 3.4 expands the analytical framework to include microorganisms capable of sliding along surfaces, then it validates these new findings through simulations.

3.2 Numerical Exploration

This section presents a numerical exploration of diffusivity across a wide range of parameter combinations, including various porous microstructures. Sec. 3.2.1 details the specific model used, while Sec. 3.2.2 describes the simulation methods. The results of this exploration, covering a broad variety of swimming parameters and confinement morphologies, are presented in Sec. 3.2.3.

3.2.1 Swimmer Model and Porous Media

Swimming Strategies A run-and-tumble (RT) microorganism moving through a porous medium is considered (Fig. 3.1). The microorganism moves with velocity v_o, undergoes rotational diffusion with coefficient D_r, and tumbles following a Poisson process at a rate of τ^{-1}, with reorientation angles following a non-chiral, arbitrary distribution. In the numerical results, three specific swimming strategies are examined: run-reverse (RR), where reorientation results in a complete reversal of direction; run-and-tumble with isotropic reorientations (RTi); and run-reverse-flick (RRF), which alternates between reversals and random $\pm 90°$ turns. Figure 1.1c shows examples of the three strategies considered here.

Surface Behavior Upon encountering a surface, the microorganism comes to a stop and remains at the solid boundary. Each tumble event while at the surface results in escape with a probability of η^{-1}, where η is the average number of tumbles required to escape. The escape direction is uniformly distributed in the available half-space (Fig. 3.1, inset). This assumption simplifies the complexity of real cell dynamics cells [11, 118] (see Sec. 1.3.1), while remaining a generic approach, consistent also with the framework used in the previous chapter for motion within the slit (see Sec. 2.2.2).

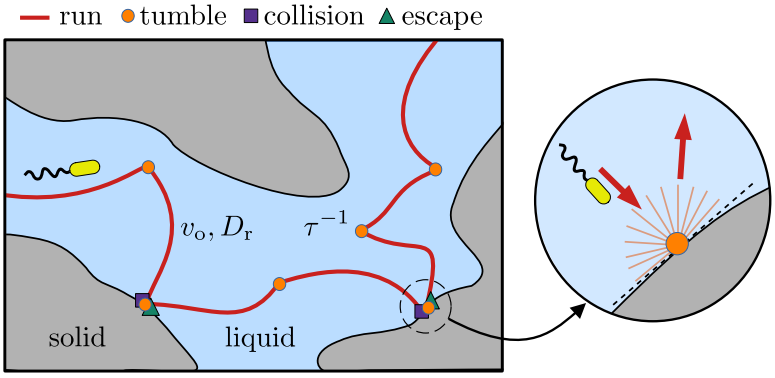

Figure 3.1: **Model of a run-and-tumble microorganism in a porous medium.** The microorganism moves with velocity v_o, undergoes rotational diffusion with coefficient D_r, and tumbles at rate τ^{-1}, where τ is the mean run time. After colliding with a surface, the microorganism can escape only by tumbling, with the new direction randomly sampled from the available half-space (orange rays in the inset).

Porous Environments To address the challenge of defining a general porous medium, different models of porous environments are considered, featuring solid obstacles of various shapes, sizes, and orientations. Specifically, the following configurations are examined: monodisperse disks on a square lattice (Fig. 3.2a), ordered rectangles with centers placed on a square lattice (Fig. 3.2b), randomly placed, non-overlapping polydisperse disks (Fig. 3.2c), and randomly placed, non-overlapping rods (Fig. 3.2d). For the polydisperse disks, radii are distributed according to a uniform distribution in the range $[0.1\overline{R}, 1.9\overline{R}]$, where $\overline{R}$ is the mean obstacle radius. This ensemble of geometries captures a wide range of possible environments, including both ordered and disordered structures, circular and linear boundaries, as well as mono- and polydisperse configurations.

3.2.2 Numerical Methods

Agent-based simulations were performed to determine diffusivity as a function of the mean run time τ across various porous environments and swimming parameters. The simulations were based on a custom `Julia` code, utilizing the `MicrobeAgents.jl` library. Detailed informations on the simulation model are provided in Appendix A.1.2.

Simulation Units In all simulations, the swimming speed v_o is set to one, defining the time unit as $t_u = l_u/v_o$, where l_u is the unit of length. The choice of l_u depends on the environment. For ordered geometries (Fig. 3.2a-b), the lattice constant W is chosen as the unit length. For disordered polydisperse disks, $l_u = \overline{R}$, the average disk radius, is used. For disordered rods, $l_u = \ell_2$, the longest side of a rod, is selected.

Diffusivity Measurements For each diffusivity measure, 2000 independent trajectories were simulated, each lasting 500 to 2000 times the mean run time τ of the microorganism. The mean-squared displacement $M(t)$ exhibits a diffusive regime at time scales typically 5-10 times larger than the mean run time. The microorganism's diffusivity is then calculated as $D = \lim_{t\to\infty} M(t)/2dt$, where $M(t)$ is the mean-square displacement

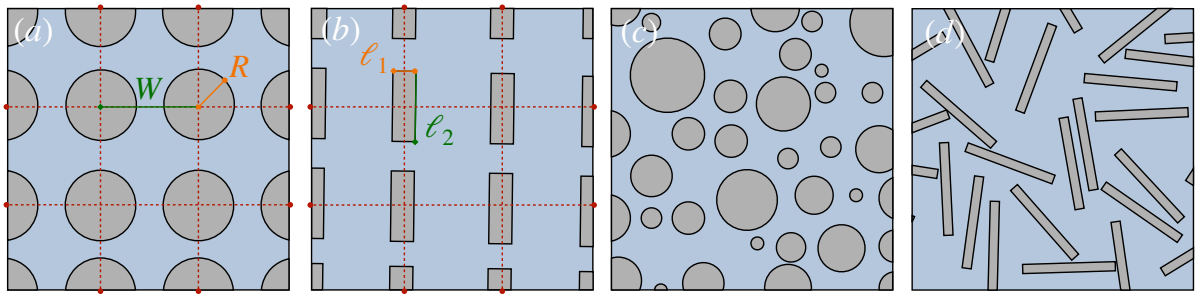

Figure 3.2: **Model porous media.** Solid regions are shown in grey, and bulk liquid in blue. (a) Monodisperse disks of radius R centered on a square lattice with constant W (in red). (b) Monodisperse rectangles with side lengths ℓ_1 and ℓ_2, centered on a square lattice. (c) Polydisperse, disordered, non-overlapping disks, with mean radius $\overline{R}$. (d) Monodisperse, disordered, non-overlapping rods.

at time t, and d is the spatial dimension. Numerical estimates of diffusivity are obtained using the same protocol as in Chapter 2, detailed in Appendix A.1.3. Displacements along the x and y directions are considered independently, yielding D_x and D_y, which are then averaged to obtain the overall diffusivity: $D = (D_x + D_y)/2$.

3.2.3 Diffusivity Maxima and Optimal Run-Times

This section presents the results of a numerical exploration of diffusivity across different environments, considering various morphologies, porosities, and swimming strategies.

Diffusivity as a function of Mean Run-Time Each case is defined by a combination of a microstructure morphology (one among the four shown in Fig. 3.2), a porosity[2] φ, a swimming pattern, and a value of rotational noise D_r. For each case, diffusivity is numerically measured as a function of the mean run-time, with at least $n_\tau \geqslant 10$ values obtained by sampling run-times spaced logarithmically over more than two orders of magnitude. The result is a $D(\tau)$ numerical curve for each case, shown in Fig. 3.3 for four different examples. Despite the variety of microstructure morphologies, solid fractions ($\bar{\varphi} = 1 - \varphi$), and swimming strategies considered, all four curves exhibit a similar trend: diffusivity reaches a maximum as a function of mean run-time. However, both the position τ^* and the peak diffusivity D^* vary from case to case.

Universal Behavior To test this maximum, $D(\tau)$ curves were measured numerically across 38 different cases, which are detailed in Table 3.1. Across all microstructures, porosities, swimming patterns, and values of rotational noise, an optimal run time τ^* has been observed, at which diffusivity reached a maximum D^*. To quantify this behavior, each $D(\tau)$ curve was fitted with a parabola over 5-7 points[3], providing numerical estimates for the position τ^*_sim and peak diffusivity D^*_sim (see Fig. 3.4a). Additionally, Fig. 3.4b shows that when $D(\tau)$ curves are rescaled by their respective maximum values, they collapse

[2]Porosity is the ratio of accessible liquid volume to total volume.

[3]The number of points is chosen manually for each case to ensure a proper fit around the maximum, depending on how many mean run times were sampled and the position of the peak.

onto a common trend. This suggests a universal dependency of diffusivity on mean run time across the diversity of all cases considered.

Ordered Disks:
Units: $l_u = W$, $t_u = W/v_o$

Case	$\bar{\varphi}$	R	D_r	Strategy	n_τ
A1	0.03	0.1	0.1	RTi	15
A2	0.03	0.1	0.1	RR	15
A3	0.07	0.15	0.1	RTi	15
A4	0.07	0.15	0.1	RR	15
A5	0.13	0.2	0.1	RTi	15
A6	0.13	0.2	0.1	RR	15
A7	0.20	0.25	0.1	RTi	15
A8	0.20	0.25	0.1	RR	15
A9	0.03	0.1	0.1	RRF	15
A10	0.07	0.15	0.1	RRF	15
A11	0.13	0.2	0.1	RRF	15
A12	0.20	0.25	0.1	RRF	15
A13	0.03	0.1	1	RTi	10
A14	0.03	0.1	2	RTi	10
A15	0.13	0.2	0.1	RTi	10
A16	0.13	0.2	0.5	RTi	10
A17	0.13	0.2	1	RTi	10
A18	0.13	0.2	2	RTi	10
A19	0.28	0.3	0.1	RTi	10
A20	0.28	0.3	0.5	RTi	10
A21	0.28	0.3	1	RTi	10
A22	0.28	0.3	2	RTi	10
A23	0.50	0.4	0.1	RTi	10
A24	0.50	0.4	0.5	RTi	10
A25	0.50	0.4	1	RTi	10
A26	0.50	0.4	2	RTi	10

Ordered Rectangles:
Units: $l_u = W$, $t_u = W/v_o$

Case	$\bar{\varphi}$	ℓ_2/ℓ_1	D_r	Strategy	n_τ
B1	0.08	1	0.1	RTi	10
B2	0.08	1	0.1	RR	10
B3	0.16	2	0.1	RTi	10
B4	0.16	2	0.1	RR	10
B5	0.24	3	0.1	RTi	10
B6	0.24	3	0.1	RR	10

Polydisperse Disordered Disks:
Units: $l_u = \overline{R}$, $t_u = \overline{R}/v_o$

Case	$\bar{\varphi}$	D_r	Strategy	n_τ
C1	0.15	0.1	RTi	10
C2	0.3	0.1	RTi	10
C3	0.3	0.1	RR	10
C4	0.4	0.1	RTi	10

Disordered Rods:
Units: $l_u = \ell_2$, $t_u = \ell_2/v_o$

Case	$\bar{\varphi}$	ℓ_2/ℓ_1	D_r	Strategy	n_τ
D1	0.03	10	0.1	RTi	10
D2	0.13	10	0.1	RTi	10

Table 3.1: **Overview of simulated parameter combinations.** n_τ is the number of mean run time values considered. Geometric parameters W, $\bar{R}$, and ℓ_1 are defined in Fig. 3.2, while D_r and swimming strategies are described in Sec. 3.2.1. All diffusivity estimates across the 38 scenarios follow a common trend, shown in Fig. 3.4.

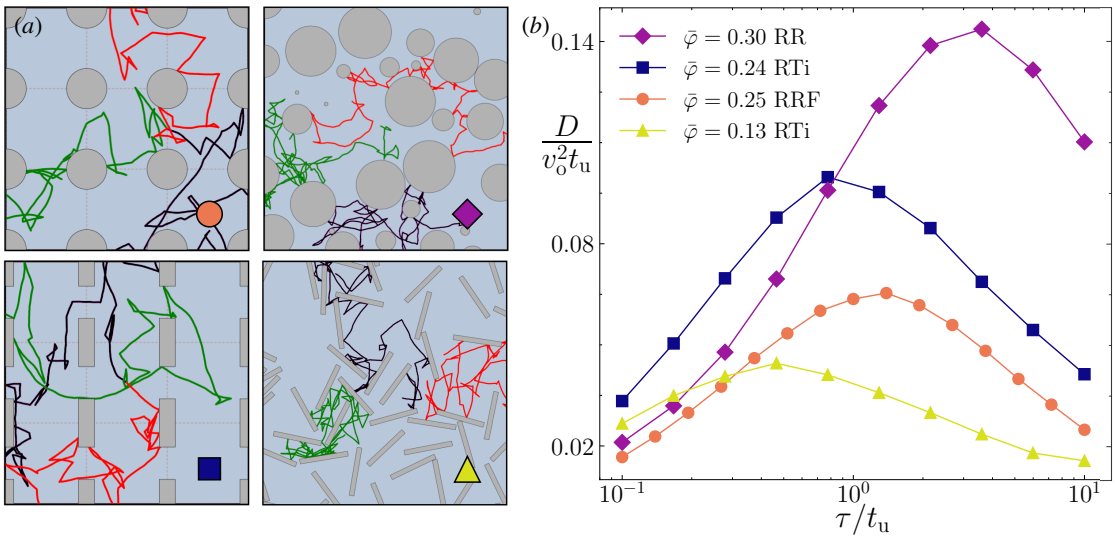

Figure 3.3: **Diffusivity vs. mean run-time across different microstructures and swimming strategies.** (a) Simulated motion within the four porous geometries detailed in Fig. 3.2. Symbols correspond to the data shown in (b): numerical estimates of diffusivity D across different microstructures at varying solid fractions $\bar{\varphi} = 1 - \varphi$, as a function of mean run time τ. A fixed value of $D_r = 0.1 t_u^{-1}$ is considered, with three possible swimming strategies: run-reverse (RR), isotropic run-and-tumble (RTi), and run-reverse-flick (RRF). All four scenarios exhibit diffusivity maxima as a function of mean run time.

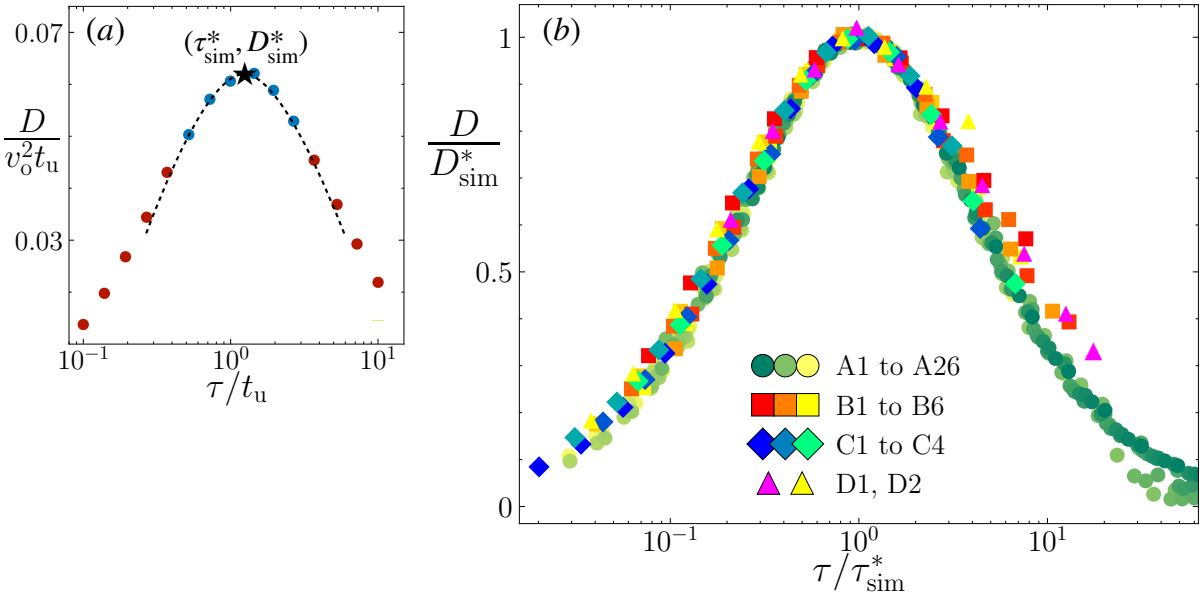

Figure 3.4: **Universal dependence of diffusivity on mean run time.** (a) Each numerical diffusivity curve (points) is fitted with a parabola (dotted line) over 5-7 points around the maximum (blue points). The fit is done in logarithmic x-scale. The fit provides a numerical estimate of the maximum location: $(\tau^*_{sim}, D^*_{sim})$. (b) Diffusivity curves rescaled by their maximum value and time. The legend refers to cases defined in Table 3.1.

3.3 Diffusivity Model and Cauchy Universality

As suggested in Sec. 3.2.3, diffusivity appears to follow a universal relationship with the mean run time, applicable across many different combinations of microstructures and motion patterns. This section develops a model to explain this behavior and provide diffusivity predictions for the different cases. Section 3.3.1 introduces a simple analytical framework, extending bulk diffusivity predictions to account for motion interruptions caused by obstacle interactions. Readers primarily interested in the results may proceed to Sec. 3.3.2, where the conclusions are summarized and the formalism is applied to the current study.

3.3.1 Analytical Framework

Unimodal Motion To develop a model for dispersal, an analytical framework to handle unimodal and multimodal motions at constant speed is first considered. This simple case of unimodal motion serves to introduce the method that will be applied throughout the chapter. For simplicity, two-dimensional motion ($d = 2$) is considered.

Diffusivity and Correlation Function Consider a particle moving at constant speed v_o, with its orientation at time t specified by the unit vector $\mathbf{e}(t)$ or angle $\theta(t)$. The orientation correlation function is defined as

$$C(t - t') \equiv \langle \mathbf{e}(t) \cdot \mathbf{e}(t') \rangle, \tag{3.1}$$

where $\langle . \rangle$ represents the ensemble average. The probability distribution $p(\theta, t)$ for the orientation θ at time t, given the initial value $p_{\text{in}}(\theta) = \delta(\theta)$, is used to express the correlation function as follows:

$$C(t) = \int_{-\pi}^{\pi} \mathrm{d}\theta \, p(\theta, t) \cos\theta. \tag{3.2}$$

Applying Fourier series for the angle ($\theta \to l$) and Laplace transforms for time ($t \to s$), as defined in Appendix. A.3.1, yields:

$$C(s) = \pi \sum_{l=\pm 1} p(l, s)\,. \tag{3.3}$$

The variable dependence of C and p are explicitly written to distinguish between the function and its transform. The diffusion coefficient D of the swimmer (defined as Eq. 1.7) is connected to the orientation correlation function[4] by:

$$dD = v_o^2 \int_0^{\infty} \mathrm{d}t \, C(t), \tag{3.4}$$

and using Eq. (3.3), the reduced diffusivity is defined as:

$$\mathcal{D} \equiv \frac{dD}{v_o^2} = \pi \sum_{l=\pm 1} p(l, s = 0). \tag{3.5}$$

Thus, knowledge of $p(l, s)$, the Fourier and Laplace transform of the probability distribution of orientation θ at time t, provides access to the swimmer's diffusivity.

[4]This relationship is detailed in Appendix A.1.3, see Eqs. A.3-A.4-A.5.

Run-and-Tumble with Interruptions

Consider now the specific case of run-and-tumble motion: the particle undergoes rotational diffusion with coefficient D_r and experiences tumbles at a rate $\tau^{-1} = \lambda$, characterized by a distribution of turning angles $h(\theta_\mathrm{t})$. Throughout this discussion, it is assumed that the tumbles are symmetric, meaning $h(\theta_\mathrm{t})$ is an even function. As noted in Sec. 1.2.2, the only aspect of h needed here is the first circular moment $\alpha = \langle \cos\theta_\mathrm{t} \rangle_h$, representing the mean cosine of the turning angle. This quantity appears frequently and is referred to as the "correlation" of the turning angle distribution h. The correlation α takes values in $[-1, 1]$, where $\alpha = 1$ indicates no directional change, $\alpha = -1$ corresponds to full reversals, and $\alpha = 0$ represents either isotropic reorientation or a 90-degree random turn[5].

The Fokker-Planck equation governing $p(\theta, t)$ is:

$$\partial_t p(\theta, t) = \mathcal{L} p(\theta, t) = D_\mathrm{r} \partial^2_{\theta\theta} p(\theta, t) - \lambda p(\theta, t) + \lambda h \otimes p(\theta, t)\,, \tag{3.6}$$

where $\mathcal{L}$ is A Liouvillian operator, and $\otimes$ denotes convolution with respect to θ, as defined in Eq. (A.13). Using a Fourier series on the angles ($\theta \to l$) yields:

$$\partial_t p(l, t) = \mathcal{L}(l) p(l, t) = \left[-D_\mathrm{r} l^2 - \lambda + 2\pi\lambda h(l) \right] p(l, t)\,. \tag{3.7}$$

Taking the Laplace transform with respect to time ($t \to s$) and solving gives $p(l, s) = p_\mathrm{in}(l)/(s - \mathcal{L}(l))$, with $p_\mathrm{in}(l) = 1/2\pi$. Using Eq. (3.5), the classical expression for the bulk diffusivity of run-and-tumble motion, initially introduced in Eq. 1.8 [82], is now re-expressed in terms of the Liouvillian $\mathcal{L}$:

$$\mathcal{D}^\mathrm{RT} = \frac{1}{2} \sum_{l=\pm 1} \frac{1}{-\mathcal{L}(l)} = \frac{1}{D_\mathrm{r} + \lambda(1 - \alpha)}\,. \tag{3.8}$$

Two important remarks follow from Eq. (3.8). First, the left equality holds whenever the Liouvillian $\mathcal{L}$ is diagonal, meaning $\mathcal{L}(l)$ acts as a multiplication operator on $p(l, \cdot)$. Second, extending this result to three-dimensional motion ($d = 3$) is done by using spherical harmonics instead of Fourier series. In the spherical harmonics basis Y_l^m, the angular Laplacian $\Delta_\mathrm{a} \equiv (1/\sin\theta)\,\partial_\theta \sin\theta\,\partial_\theta + (1/\sin^2\theta)\,\partial^2_{\phi\phi}$ can be rewritten[6] as $\Delta_\mathrm{a} = -l(l+1)$. The result is that Eq. (3.8) still applies when $d = 3$, if D_r is replaced by $2D_\mathrm{r}$.

Interrupted Motion A modified process termed interrupted motion is now introduced for any diagonal Liouvillian $\mathcal{L}$. In this process, in addition to the evolution governed by $\mathcal{L}$, reorientation events occur also according to a Poisson process with rate Λ and an even distribution of turning angles characterized by the correlation β. Interruptions are treated as a second type of tumbling event, though they serve a distinct role, and thus a separate term is used to avoid confusion. The diffusivity of run-and-tumble motion with added interrupted motion at rate Λ and correlation β can be computed straightforwardly:

$$\mathcal{D}(\Lambda, \beta) = \frac{1}{2} \sum_{l=\pm 1} \frac{1}{-\mathcal{L}(l) + \Lambda\bar{\beta}} = \frac{1}{D_\mathrm{r} + \lambda\bar{\alpha} + \Lambda\bar{\beta}}, \tag{3.9}$$

[5] Whether the reorientation angles are sampled from a uniform distribution or correspond to random $\pm 90°$ turns, the average cosine of turning angles is zero.

[6] See Ref. [90] for further details.

with $\bar{\alpha} \equiv 1-\alpha$ and $\bar{\beta} \equiv 1-\beta$. Since the three decorrelation processes—rotational diffusion, tumbling, and interruptions—are memoryless and independent, their rates simply add together. Equation (3.9) will be used throughout the subsequent sections. Specifically, Sec. 3.3.2 will use it to develop a diffusivity model.

3.3.2 Minimal Model of Diffusivity

A simple model of microbial dispersal in a porous medium is proposed, where the primary approximation is to neglect the complex correlations between the microorganism's trajectory and the microstructure. Specifically, encounters with solid surfaces are assumed to occur along the trajectory as a Poisson process with rate $\mathcal{T}^{-1}$ and are treated as a second type of tumble [118, 127], in addition to the inherent tumbling behavior of the microorganisms. Starting from Eq. 3.9, the proposed model of diffusivity for a microorganism moving with in the porous medium is:

$$\boxed{D = \frac{\mathcal{T}}{\mathcal{T} + \tau_\mathrm{s}} \frac{v_\mathrm{o}^2/d}{D_\mathrm{r}' + \bar{\alpha}\tau^{-1} + \bar{\beta}\mathcal{T}^{-1}} K(\bar{\varphi}).} \tag{3.10}$$

Here, $\tau_\mathrm{s} = \eta\tau$ is the mean time spent at the surface after an encounter, $D_\mathrm{r}' \equiv (d-1)D_\mathrm{r}$, $\bar{\alpha} = 1-\alpha$, $\bar{\beta} = 1-\beta$, and $\bar{\varphi} = 1-\varphi$. The parameter α is the mean cosine of the reorientation angle θ_t, or "correlation" in short, induced by a tumble, while β represents the correlation of reorientation induced by a surface encounter. The factor $K(\bar{\varphi})$ is a correction term dependent on the porosity $\varphi = 1-\bar{\varphi}$ and on the morphology of the microstructure.

The physical interpretation of Eq. (3.10) is simple. Each of the three terms in the equation encapsulates one physical effect governing dispersal. The first term represents the fraction of time spent moving through the bulk fluid. The second term captures the three independent processes—-rotational diffusion, tumbling, and surface encounters—that drive orientational decorrelation, with their rates simply adding together in the denominator. Finally, the third term accounts for the excluded volume and correlations imposed by the porous microstructure.

Completing the Model: $\mathcal{T}$, β, and $K(\varphi)$

To finalize the model, three additional elements must be specified: the mean time $\mathcal{T}$ between surface encounters, the correlation β associated with interruptions, and the excluded volume term $K(\varphi)$. Each quantity is now addressed one by one.

Encounter Rate $\mathcal{T}$ and Cauchy Universality The surface encounter time $\mathcal{T}$ follows a surprisingly simple and universal expression, a result [175, 176] whose connection to microbial dispersal seems to have gone mostly unnoticed, with some exceptions [118, 127, 177, 178]. Given that the swimming speed is constant, $v_\mathrm{o}\mathcal{T}$ corresponds to the mean free path $\langle L \rangle$, which is defined as the trajectory length between successive contacts with the surface. This mean free path exhibits an invariance property, commonly referred to as Cauchy universality, which states that the mean free path is equal to the mean chord

length l_c of the medium. The mean chord length is known generically in dimension d, giving:

$$v_o \mathcal{T} = \langle L \rangle = l_c = \sigma_d \frac{\Omega}{\partial\Omega} = \sigma_d \frac{\varphi}{\mathcal{S}}, \tag{3.11}$$

where σ_d equals π for $d = 2$ and 4 for $d = 3$; Ω represents the volume of the porous space, $\partial\Omega$ is the solid interface area, and $\mathcal{S}$ is the specific surface[7] of the microstructure. Originally derived for ballistic motion [179–181], Eq. (3.11) applies under more general conditions [177, 178], including random motion with reorientation events that may be anisotropic, inhomogeneous, or non-Poissonian [175, 176, 182]. Thus, it is applicable to the generic run-and-tumble model considered in the simulations.

Correlation β The correlation β, which characterizes the reorientation induced by an encounter with the surface, must now be specified. This requires the distributions of the in-going angle ϕ_{in} and out-going angle ϕ_{out}, defined relative to the surface normal (Fig. 3.5). In this regard, the simplest assumptions are considered. The angle ϕ_{in} is taken to be proportional to $\cos\phi_{\text{in}}$, accounting for the directional dependence of the flux against the wall. Assuming that tumbles completely randomize the direction of escape, the angle ϕ_{out} is chosen to be uniformly distributed within the free half-space outside the surface tangent. These assumptions lead to the following probability distributions:

$$P(\phi_{\text{in}}) = I_{[-\frac{\pi}{2},\frac{\pi}{2}]}(\phi_{\text{in}}) \frac{\cos\phi_{\text{in}}}{2}, \qquad P(\phi_{\text{out}}) = I_{[-\frac{\pi}{2},\frac{\pi}{2}]}(\phi_{\text{out}}) \frac{1}{\pi}, \tag{3.12}$$

where $I_{[a,b]}(u) = 1$ for $a \leqslant u \leqslant b$ and 0 otherwise. The distribution of the turning angle induced by an encounter with the surface is then:

$$h(\theta) = \iint_{-\pi}^{\pi} \mathrm{d}\phi_{\text{in}}\, \mathrm{d}\phi_{\text{out}}\ \delta[\text{v.p.}(\theta - (\phi_{\text{out}} + \pi - \phi_{\text{in}}))]\, P(\phi_{\text{in}}) P(\phi_{\text{out}}) = \frac{1 - \cos\theta}{2\pi} I_{[-\pi,\pi]}, \tag{3.13}$$

where δ is the Dirac function, $\text{v.p.}(\theta) \equiv \arg[e^{i\theta}]$ takes values in the $[-\pi, \pi]$ interval, and the $+\pi$ term accounts for the reversal of direction at the wall. The correlation characterizing wall encounters is therefore $\beta = \langle \cos\theta \rangle_h = -1/2$.

[7] The term "specific surface" refers to the ratio of surface area to total volume in three dimensions, or to total boundary length over total area in two dimensions

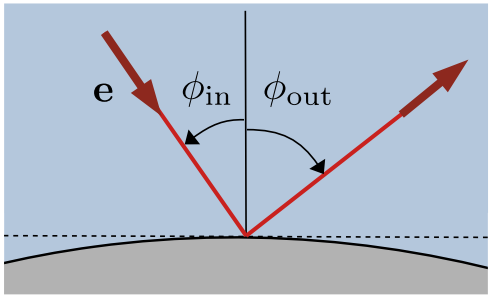

Figure 3.5: **Reorientation induced by a stay at the wall.** The particle's direction is described by the in-going angle ϕ_{in} before contact and the out-going angle ϕ_{out} upon escaping, taken with respect to the surface normal.

Factor $K(\varphi)$ Equation (3.10) without the factor $K(\varphi)$ was found to overestimate the numerical estimates of diffusivity (not shown), likely due to neglecting the excluded volume and fixed positions of solid domains. To reintroduce these effects in a simple way, the prediction is adjusted to be exact in the limit of passive Brownian motion[8], by incorporating an ad hoc prefactor $K(\bar{\varphi})$ that depends solely on the solid fraction $\bar{\varphi}$. This modification yields the final form of Eq. 3.10. For a given microstructure, $K(\bar{\varphi}) \equiv D^{\mathrm{BM}}/D_{\mathrm{o}}^{\mathrm{BM}}$ is defined as the ratio between the effective diffusivity D^{BM} of a passive Brownian tracer in a porous structure with solid fraction $\bar{\varphi}$, and its free-space diffusion coefficient $D_{\mathrm{o}}^{\mathrm{BM}}$. This factor $K(\bar{\varphi})$ is known for several cases. For a square array of disks, Ref. [183] provides an analytical approximation covering the full range of porosities. Specifically, at low solid fractions, a rigorous expansion yields:

$$K(\bar{\varphi}) = \frac{1}{1+\bar{\varphi}} + \mathcal{O}(\bar{\varphi}^5). \tag{3.14}$$

For randomly placed overlapping obstacles, such as spheres and cylinders, Refs. [184,185] propose the approximation $K(\bar{\varphi}) = (1-\bar{\varphi}/\bar{\varphi}_{\mathrm{c}})^{\mu}/1-\bar{\varphi}$, where the critical fraction $\bar{\varphi}_{\mathrm{c}}$ and exponent μ are determined numerically.

A more general relation that applies for arbitrary microstructures in any dimension is the low-$\bar{\varphi}$ expansion [181]:

$$K(\bar{\varphi}) = 1 - \frac{\bar{\varphi}}{d-1} + \mathcal{O}(\bar{\varphi}^2), \tag{3.15}$$

valid for small solid fractions. Throughout this work, Eq. (3.14) is used for square arrays of disks, while Eq. (3.15) is applied in all other cases.

3.3.3 Assessing the Model: Diffusivity Master Curve

The predictions of the model are now assessed. Based on the observation that numerical results collapse when rescaled by their maxima (see Fig. 3.4), Equation (3.10) is first rewritten as:

$$\frac{D}{D^*} = \frac{(2+c)\xi}{1+c\xi+\xi^2}, \quad \xi \equiv \frac{\tau}{\tau^*}, \tag{3.16}$$

where ξ is the mean run time rescaled by the optimal value. This formula indicates that diffusivity reaches a maximum D^* at the mean run time τ^*, given by:

$$D^* = \sqrt{ab}K(\bar{\varphi})/(2+c)\bar{\alpha}d, \quad \tau^* = \sqrt{ab}, \tag{3.17}$$

with $a \equiv \mathcal{T}/\eta$, $b \equiv \bar{\alpha}/(D_{\mathrm{r}} + \bar{\beta}/\mathcal{T})$, and $c \equiv (a+b)/\sqrt{ab}$. Although Eq. (3.16) is not strictly universal, due to its dependence on the parameter c, this dependence can be entirely accounted for by introducing the modified diffusivity ratio:

$$\mathcal{R} \equiv 4\left[2 - c + (2+c)\frac{D^*}{D}\right]^{-1} = \frac{4\xi}{(1+\xi)^2}, \tag{3.18}$$

[8]This limit can be approached by taking $D_{\mathrm{r}} = 0$, $\alpha = 0$, and $\tau \to 0$, while keeping $v_{\mathrm{o}}^2\tau/d \equiv D_o$ fixed.

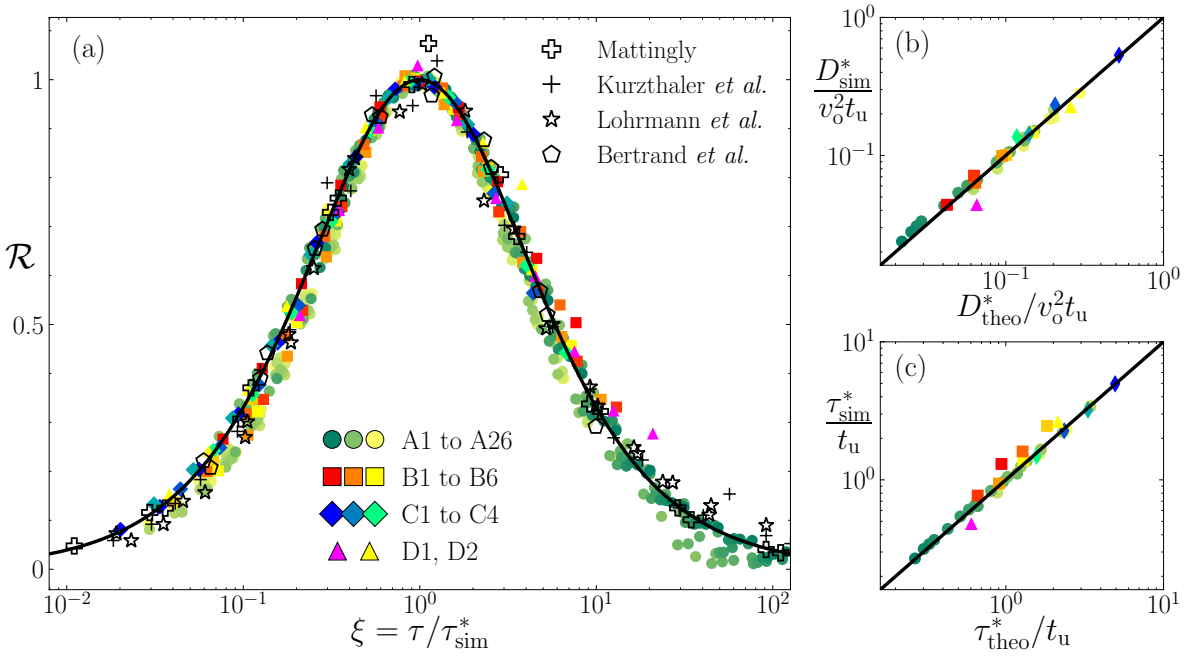

Figure 3.6: **Diffusivity predictions and master curve.** (a) The modified diffusivity ratio $\mathcal{R}$ for various solid fractions, microstructures, and swimming strategies collapses onto the master curve (black line), as predicted by Eq. (3.18). The colored legend refers to cases in Table 3.1, while symbols correspond to data from the literature (see text for references). (b-c) Comparison between simulation results (y-axis) and theoretical predictions (x-axis) for (b) maximum diffusivity D^* and (c) optimal run time τ^*. The black line represents the 1:1 correspondence between theory and simulation.

which depends only on ξ and is independent of both motion parameters and microstructure. Fig. 3.6a shows that for the 38 parameter combinations tested—varying swimming strategy, rotational diffusion, porosity, and microstructure—the diffusivity values from simulations collapse onto the master curve $\mathcal{R}(\xi)$, as predicted by Eq. (3.18). The dependence on c in Eq. (3.16) is relatively weak, as c varies over a limited range across simulations. This explains the approximate collapse seen for D/D^* in Fig. 3.4. Additionally, the simulation results for maximum diffusivity D^* and optimal run time τ^* closely match the theoretical predictions from Eq. (3.17) (Figs. 3.6b-c). The comprehensive numerical exploration thus supports the proposed generic diffusivity model.

Data from literature In addition to the simulations from Table 3.1, results from several prior studies were incorporated to further test the model[9]. In the preprint by Mattingly [131], run-and-tumble point particles move in a porous medium composed of overlapping disks. Kurtzhaler *et al.* [21] and Lohrmann *et al.* [128] study three-dimensional motion through overlapping spheres, with finite-sized RT polymers. Bertrand *et al.* [22] examine motion where both particles and obstacles are constrained on a lattice, using

[9]Specifically, data from Ref. [131] was extracted from Fig. 3, inset D, focusing on three curves where diffusivity maxima are shown. Data from Ref. [21] was taken from the three numerical curves in Fig. 3, inset a. Data from Ref. [128] was obtained from Fig. 8, specifically for RT, RR, and RRF motion with $r_p = 4\,\mu$m. Data from Ref. [22] corresponds to the three curves in Fig. 2 ("Fixed obstacle" inset).

discrete directions. Each of these studies reports diffusivity maxima as a function of run-time. For each study, diffusivity data was first rescaled by their estimated maximum. Then, a fit to Eq. (3.16) was used to estimate the c parameter[10], which in turn was used to compute the ratio $\mathcal{R}$ from Eq. (3.18). The resulting curves aligned well with the model's master curve (Fig. 3.6a), suggesting that the theoretical framework is applicable across these cases, including three-dimensional motion, overlapping obstacles, surface motion, and discrete directions.

Prediction for Run-reverse-flick On a last note, the model described by Eq. 3.10 does not yet account for bimodal swimming patterns like RRF, but offers a foundation for a simple approximation. Neglecting the strict alternation between reversals ($\alpha = -1$) and flicks ($\alpha = 0$), the two event types are treated as independent processes, each occurring at a rate of $(2\tau)^{-1}$. With this simplifying assumption, Eq. 3.10 still holds, but with the correlation set to the average of reverse and flick events, yielding $\alpha = -1/2$. This approximation successfully rescaled the data onto the master curve and accurately predicted the diffusivity maximum (RRF data included in Fig. 3.6).

Physical Interpretation of the Maximum The existence of the diffusivity maximum can be anticipated, as diffusivity scales as $D \sim \tau$ for short runs but decreases as $D \sim (\eta\tau)^{-1}$ for long runs, since most time is spent at the surface waiting to escape. A similar argument was already given for the case of motion within slit confinement, as discussed earlier in Sec. 2.4.1. From Eq. (3.17), the explicit expression for the optimal mean run time is:

$$\tau^* = \sqrt{\bar{\alpha}\mathcal{T}/(\eta(D_\mathrm{r} + \bar{\beta}/\mathcal{T}))}. \tag{3.19}$$

When rotational diffusion is strong ($D_\mathrm{r}\mathcal{T} \gg 1$), $\tau^* = \sqrt{\bar{\alpha}\mathcal{T}/D_\mathrm{r}\eta}$ is the harmonic mean between the surface encounter time and the rotational diffusion time, balancing the two processes driving orientation decorrelation. When rotational diffusion is negligible ($D_\mathrm{r}\mathcal{T} \ll 1$), $\tau^* = \mathcal{T}\sqrt{\bar{\alpha}/\eta\bar{\beta}}$ is primarily controlled by the surface encounter time, with a prefactor typically less than one. In this case, the optimal mean run length $v_\mathrm{o}\tau$ is dictated by the mean free path l_c, as it represents the best compromise between efficient transport through the porous space and the drawback of becoming trapped at the surface.

3.4 Multimodal Motion and Surface Sliding

Re-tracing the steps of Chapter 2, the focus now shifts to cases that include motion occurring at the surface. This reflects the already well-discussed importance of microorganisms that move along obstacle boundaries (see Secs. 1.3.1 or 2.2.2). To address this, the formalism from Sec. 3.3.1 is first extended to handle bimodal and trimodal motion. Readers interested only in results may proceed to Sec. 3.4.2, where surface motion model is introduced, and the analytical approach is concluded. Finally, in Sec. 3.4.3 results are tested and discusses on new numerical data that includes motion at the boundary.

[10]Due to additional effects not modeled in this work and incomplete descriptions of specific cases, c was fitted rather than computed from system parameters.

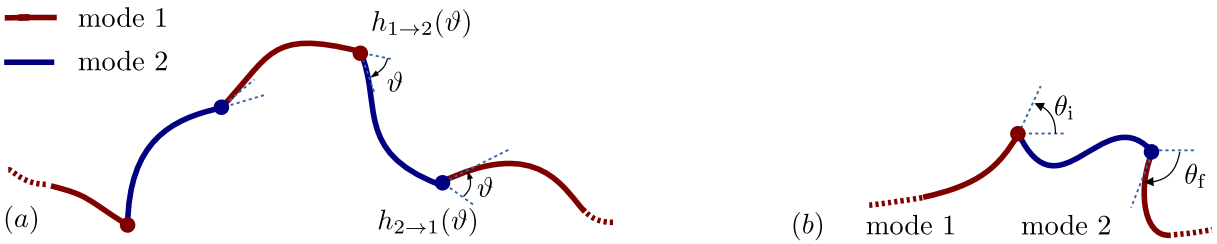

Figure 3.7: **Bimodal process.** (a) The microorganism alternates between two modes, each with different properties. $h_{m\to m'}(\vartheta)$ represents the turning angle distribution when switching from mode m to m'. (b) Initial angle θ_i and final angle θ_f involved in the effective correlation β_1^e.

3.4.1 Diffusivity for Bimodal Motion

Consider now bimodal motion, where the particle, or microorganism, alternates between two distinct modes of motion. Each mode, labeled $m = 1, 2$, is governed by a Liouvillian $\mathcal{L}_m$, assumed diagonal and even in l in Fourier space. Transitions between modes occur with rate μ_1 or μ_2 and involve a distribution of turning angles $h_{1\to2}$ with correlation β_1 for transitions from mode 1 to mode 2. Similar notations apply for transitions from mode 2 to mode 1. The goal is to obtain the diffusivity of this bimodal motion and its relationship to the diffusivities of unimodal motions.

Diffusivity Equation Let $p_m(\theta, t)$ denote the probability distribution in mode m. The Fokker-Planck equations are:

$$\partial_t p_1(\theta,t) = \mathcal{L}_1 p_1 - \mu_1 p_1 + \mu_2 p_2 \otimes h_{2\to1}, \tag{3.20a}$$
$$\partial_t p_2(\theta,t) = \mathcal{L}_2 p_2 - \mu_2 p_2 + \mu_1 p_1 \otimes h_{1\to2}. \tag{3.20b}$$

In Fourier-Laplace space, this system becomes:

$$\begin{bmatrix} s+\mu_1-\mathcal{L}_1(l) & -2\pi\mu_2 h_{2\to1}(l) \\ -2\pi\mu_1 h_{1\to2}(l) & s+\mu_2-\mathcal{L}_2(l) \end{bmatrix} \begin{bmatrix} p_1(l,s) \\ p_2(l,s) \end{bmatrix} = \begin{bmatrix} p_{1\mathrm{in}}(l) \\ p_{2\mathrm{in}}(l) \end{bmatrix}. \tag{3.21}$$

Here, $p_{m\mathrm{in}}(l)$ are the initial conditions, and ν_m denotes the fraction of time spent in mode m, with:

$$\nu_1 = 1 - \nu_2 = \frac{\mu_2}{\mu_1+\mu_2}. \tag{3.22}$$

Solving Eq. (3.21) yields the total probability $p = p_1 + p_2$ and the diffusivity. Introducing the effective correlation β_1^e induced by the transition from mode 1 to mode 2 (derivation shown at the end):

$$\beta_1^\mathrm{e} = \frac{\beta_1\beta_2}{2} \sum_{l=\pm1} \frac{\mu_2}{\mu_2 - \mathcal{L}_2(l)}, \tag{3.23}$$

the diffusivity for bimodal motion is given by:

$$\boxed{\mathcal{D} = \nu_1 \mathcal{D}_1(\mu_1, \beta_1^\mathrm{e}) + \nu_2 \mathcal{D}_2(\mu_2, \beta_2^\mathrm{e}) + C', \quad C' = \frac{(\beta_1+\beta_2)/(\mu_1+\mu_2)}{[\mu_1\mu_2\mathcal{D}_1(0)\mathcal{D}_2(0)]^{-1} - \beta_1\beta_2},} \tag{3.24}$$

where $\mathcal{D}_m(\mu, \beta)$ follows the same definition as in Eq. (3.9), and $D_m(0)$ is the diffusivity of uninterrupted motion in mode m.

Discussion and Limiting Behaviours The first two terms in Eq. (3.24) can be intuitively expected: the diffusivity involves a weighted average of interrupted unimodal diffusivities because each mode m is interrupted with rate μ_m by the other, and these interruptions induce a reorientation with effective correlation β^{e}_m. Yet, Eq. (3.24) also indicates that the diffusivity includes an additional contribution, which involve the transitions between modes. Whenever some degree of correlation is retained, on average, when switching mode ($\beta_1 + \beta_2 \neq 0$), the correction is needed.

In special cases, such as isotropic reorientations ($\beta_1 = \beta_2 = 0$), Eq. (3.24) recovers previous results from the literature. Similarly, if both modes only involve rotational diffusion and share the same switching rate, it reduces to expressions from prior studies [82]. As a final remark, Eq. (3.24) can be used to recover the minimal model presented earlier. Mode 1 corresponds to run-and-tumble motion in porous space, while mode 2 corresponds to a motionless state. This leads back to Eq. (3.9) and, after including the correction factor $K(\bar{\varphi})$, Eq. 3.10.

Derivation of effective correlation β^{e} Consider the situation depicted in Fig. 3.7b, where the microorganism experiences a sojourn in mode 2, surrounded by two periods in mode 1. The objective is to determine the effective correlation induced by such a passage through mode 2, denoted as $\beta^{\mathrm{e}}_1 \equiv \langle \cos(\theta_{\mathrm{f}} - \theta_{\mathrm{i}}) \rangle$, where θ_{i} (resp. θ_{f}) represents the orientation immediately before exiting (resp. after re-entering) mode 1. To derive the probability distribution $P(\theta = \theta_{\mathrm{f}} - \theta_{\mathrm{i}})$ at the final time, the evolution of θ is broken down into three steps. First, upon the interruption of mode 1, the new distribution is given by $P_I(\theta) = p_{\mathrm{in}} \otimes h_{1\to 2}$, resulting in $P_{\mathrm{I}}(l) = h_{1\to 2}(l)$. Second, during the sojourn in mode 2, the evolution follows the equation $\partial_t P_{\mathrm{II}}(\theta, t) = (\mathcal{L}_2 - \mu_2) P_{\mathrm{II}}$, leading to $P_{\mathrm{II}}(l, s) = h_{1\to 2}(l)/(s + \mu_2 - \mathcal{L}_2(l))$. The probability density for leaving mode 2 at any time with orientation θ is then $P_{\mathrm{III}}(l) = \mu_2 P_{\mathrm{II}}(l, s = 0)$. Finally, when mode 2 is interrupted, the distribution becomes $P = P_{\mathrm{III}} \otimes h_{2\to 1}$. Combining all steps, the final probability distribution is:

$$P(l) = 2\pi h_{1\to 2}(l) \frac{\mu_2}{\mu_2 - \mathcal{L}_2(l)} h_{2\to 1}(l). \tag{3.25}$$

The effective correlation $\beta^{\mathrm{e}} \equiv \langle \cos\theta \rangle$ is obtained by $\pi(P(l = 1) + P(l = -1))$, which yields back Eq. (3.23). This result shows that the effective correlation is simply the product of the correlations involved in each individual step.

3.4.2 Surface Sliding and Trimodal Motion

When a microorganism encounters a solid surface and slides along it, rather than stopping, the motion becomes multimodal. In this section, a microswimmer model incorporating surface motion is introduced, and the formalism initially developed in Sec. 3.4 is further extended to model its diffusivity.

Microswimmer Model with Surface Motion The porous medium considered is a square lattice of disks (Fig. 3.2a). Upon encountering an obstacle, the microswimmer aligns its direction parallel to the surface and swims either clockwise or counterclockwise, following the circular boundary with a tangential velocity equal to its bulk speed (Fig. 3.8).

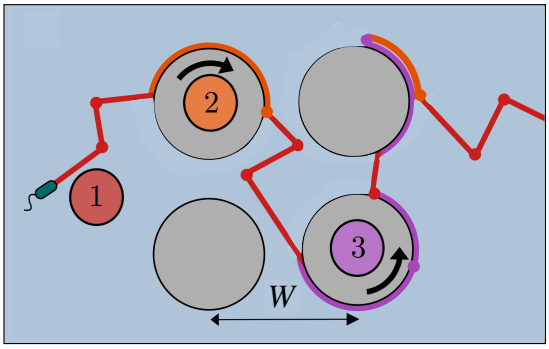

Figure 3.8: **Run-and-tumble with surface motion.** Porous media consist of monodisperse disks, with radius R, arranged on a lattice with constant W. The microorganism can move through the porous space (mode 1) or along the obstacle surface in either a clockwise (mode 2) or counterclockwise (mode 3) direction. Upon collision, the microorganism aligns with the surface, while each tumble ($\circ$) at the surface results can result in an escape or a reversal.

While sliding along the surface, tumbling events can lead to one of three outcomes: an escape from the surface, a reversal along the surface, or continuation in the same direction. Assuming surface tumbling is isotropic, as was done for surface motion within a slit in Chapter 2, these events occur with probabilities of 1/2, 1/4, and 1/4, respectively[11].

Trimodal Motion: Model and Diffusivity

To explore the implications of multimodal motion, Sec. 3.4 introduced an analytical formalism for bimodal processes, where modes $m = 1$ and 2 alternate. However, in this case, the motion is trimodal because displacement along the obstacle surface can be either clockwise or counterclockwise (Fig. 3.9a). Mode 1 represents run-and-tumble motion in the porous space, governed by the Liouvillian $\mathcal{L}_1$, and is exited with rate μ_1. Mode 2 (clockwise motion) and mode 3 (counterclockwise motion) describe surface sliding, with angular velocities of $-\omega$ and ω, respectively. Upon leaving mode 1, there is an equal probability (1/2) of entering mode 2 or mode 3. While on the surface (in mode 2 or 3), the particle can reverse direction with rate κ or escape with rate μ. The distribution of turning angles between modes is denoted by $h_{m\to m'}$, with $h_{\mathrm{r}}(\theta) = \delta(\theta - \pi)$ representing the reversal angle distribution between modes 2 and 3. The transition rates between the different states are summarized in Fig. 3.9.

The governing equations for $p_m(\theta, t)$ are now

$$\partial_t p_1(\theta,t) = \mathcal{L}_1 p_1 - \mu_1 p_1 + \mu\left[p_2 \otimes h_{2\to1} + p_3 \otimes h_{3\to1}\right], \tag{3.26a}$$

$$\partial_t p_2(\theta,t) = \mathcal{L}_2 p_2 - (\mu+\kappa) p_2 + \frac{\mu_1}{2} p_1 \otimes h_{1\to2} + \kappa p_3 \otimes h_{\mathrm{r}}, \tag{3.26b}$$

$$\partial_t p_3(\theta,t) = \mathcal{L}_3 p_3 - (\mu+\kappa) p_3 + \frac{\mu_1}{2} p_1 \otimes h_{1\to3} + \kappa p_2 \otimes h_{\mathrm{r}}. \tag{3.26c}$$

It is assumed that particles moving clockwise and counterclockwise are subject to the same dynamics, which results in the following symmetry relations linking mode 2 and 3:

$$h_{1\to2}(\theta) = h_{1\to3}(-\theta), \qquad h_{2\to1}(\theta) = h_{3\to1}(-\theta). \tag{3.27}$$

[11] At the boundary, if the new direction after tumbling is chosen isotropically, there is a 1/2 probability of pointing outward into the free half-space and a 1/2 probability of pointing inward, back toward the surface. When pointing inward, there is a 1/4 probability of being aligned with either the original direction or its opposite.

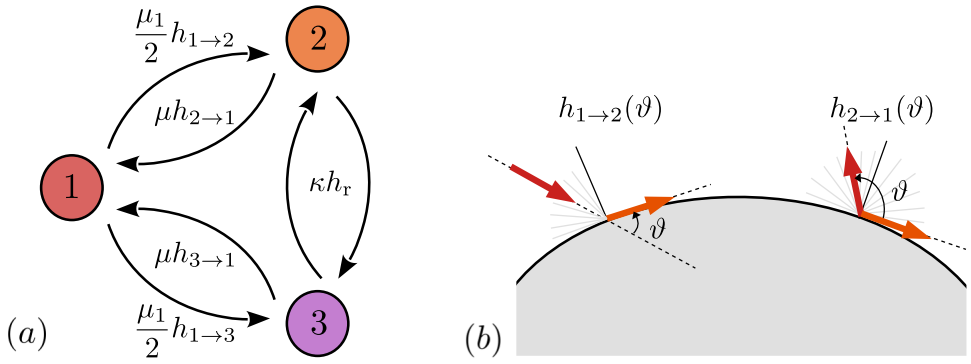

Figure 3.9: **Trimodal Motion.** (a) Mode transition diagram showing rates between the three motion modes (defined in Fig. 3.8). (b) Reorientation of the particle when encountering or leaving the surface.

Though the Liouvillians take a specific form in our model, the diffusivity derived below is in fact valid in more general conditions: Liouvillians are all diagonal, $\mathcal{L}_1(l)$ is even, $\mathcal{L}_2 = -\mathcal{L}_3$ and Eq. (3.27) holds.

Diffusivity Equation The method to address the trimodal motion is entirely similar to that used for bimodal case. The end result is

$$\boxed{\mathcal{D} = \nu_1 \mathcal{D}_1(\beta_1^{\mathrm{e}})\,[1+\mathcal{C}] + \nu_{\mathrm{s}}\mathcal{D}_{\mathrm{s}}(\beta_{\mathrm{s}}^{\mathrm{e}}),} \tag{3.28}$$

where $\nu_{\mathrm{s}} = 1 - \nu_1$ is the fraction of time spent in surface mode. To specify each term of Eq. (3.28), let us introduce the short-hand notations

$$Z \equiv \mu - \mathcal{L}(l), \quad \gamma \equiv [h_{1\to2}(l)h_{2\to1}(l)]|_{l=1}\,, \tag{3.29a}$$
$$Z^\star \equiv \mu + \mathcal{L}(l), \quad \gamma' \equiv [h_{1\to2}(l) + h_{2\to1}(l)]|_{l=1}\,, \tag{3.29b}$$
$$\langle z_1, z_2\rangle \equiv \mathrm{Re}[z_1^* z_2], \quad \gamma'' \equiv -1/4[h_{1\to2}(l) - h_{1\to2}(-l)][h_{2\to1}(l) - h_{2\to1}(-l)]|_{l=1}\,. \tag{3.29c}$$

where Re denotes the real part and * the complex conjugate. The diffusivity $\mathcal{D}_1$ and effective correlation β_1^{e} associated to mode 1 are

$$\mathcal{D}_1(\beta) = \left.\frac{1}{-\mathcal{L}_1(l) + \mu_1\bar{\beta}}\right|_{l=1}, \qquad \beta_1^{\mathrm{e}} = \mu\left.\frac{\langle\gamma, Z\rangle - 2\kappa\gamma''}{ZZ^\star + 2\kappa\mu}\right|_{l=1}. \tag{3.30}$$

The diffusion coefficient $\mathcal{D}_{\mathrm{s}}$ and effective correlation $\beta_{\mathrm{s}}^{\mathrm{e}}$ associated to surface mode are:

$$\mathcal{D}_{\mathrm{s}}(\beta) = \left.\frac{\mu(1+\beta\gamma'')}{ZZ^\star - \beta\langle\gamma, Z\rangle + 2\kappa\mu(1+\beta\gamma'')}\right|_{l=1}, \qquad \beta_{\mathrm{s}}^{\mathrm{e}} = \left.\frac{\mu_1}{\mu_1 - \mathcal{L}_1(l)}\right|_{l=1}. \tag{3.31}$$

Finally, the correction term is

$$\mathcal{C} = \left.\frac{\mu_1\langle\gamma', Z\rangle}{ZZ^\star + 2\kappa\mu}\right|_{l=1}. \tag{3.32}$$

3.4.3 Predictions and Simulations

This section presents the explicit predictions for the model introduced in Sec. 3.4.2 and tests the formalism using numerical estimates of diffusivity for the surface sliding model.

Run-and-Tumble and Surface Sliding within an Array of Disks

To apply the diffusivity formula for specific trimodal motion (Eq. 3.28) to the surface motion model (Fig. 3.8), the Liouvillians for the three modes are given by:

$$\mathcal{L}_1 = D_\mathrm{r}\partial^2_{\theta\theta} - \lambda + \lambda h\otimes, \qquad \mathcal{L}_2 = -\mathcal{L}_3 = -\omega\partial_\theta. \tag{3.33}$$

Regarding the distribution $h_{m\to m'}$ (Fig. 3.9b), it is assumed that upon contacting the surface, the particle immediately aligns with the surface tangent, selecting the direction closest to its initial orientation. As before, a particle leaving the surface chooses a random direction uniformly distributed in the available half-space. The corresponding turning angle distributions for transitions between modes are:

$$h_{1\to2}(\theta) = h_{1\to3}(-\theta) = I_{[0,\pi/2]}(\theta)\times\sin\theta, \qquad h_{2\to1}(\theta) = h_{3\to1}(-\theta) = \frac{I_{[0,\pi]}(\theta)}{\pi}, \tag{3.34}$$

which results in $\gamma = -1/2 - i/\pi$, $\gamma' = 1/2 - i(2/\pi + \pi/4)$, and $\gamma'' = 1/2$. Applying Eq. (3.28), the diffusivity is explicitly given by:

$$\mathcal{D} = \frac{\mu}{\mu+\mu_1}\frac{2\left(2\kappa\mu+\mu^2+\omega^2\right)+2\mu_1\left(D_\mathrm{r}-\omega\mathrm{Im}\left[\gamma'\right]+\lambda\bar{\alpha}+\mu\mathrm{Re}\left[\gamma'\right]+\mu_1+\mu_1\gamma''\right)}{2\left(2\kappa\mu+\mu^2+\omega^2\right)\left(D_\mathrm{r}+\lambda\bar{\alpha}\right)+2\mu_1\left(2\kappa\mu+\mu^2+\omega^2+\mu\omega\mathrm{Im}[\gamma]-\mu^2\mathrm{Re}[\gamma]+2\kappa\mu\gamma''\right)} \tag{3.35}$$

Here, the angular velocity is $\omega = v_\mathrm{o}/R$, where R is the disk radius, while $\mu_1 = \mathcal{T}^{-1}$ and $\lambda = \tau_\mathrm{r}^{-1}$. Finally, a particle tumbling at the surface has a probability η^{-1} of leaving. If it remains at the wall, the particle has an equal probability of continuing in the same direction or reversing, which gives the rates:

$$\mu = \lambda\eta^{-1}, \qquad \kappa = \lambda\frac{1-\eta^{-1}}{2}, \tag{3.36}$$

where $\eta = 2$ is the value used in all numerical results presented below.

Comparison with Numerical Data To test Eq. 3.35, the system under study is simulated. Results are presented in Fig. 3.10 for two swimming strategies (RTi and RR) at varying solid fractions $\bar{\varphi}$. The predicted diffusivities (solid lines) agree well with the simulation data (Fig. 3.10a-b). In comparison to cases corresponding cases without surface motion (dotted lines), surface motion has a net effect of increasing diffusivity, especially at low and intermediate run-times.

Influence of Surface Motion on the Maximum The influence of surface behavior on the diffusivity maximum can also be examined (Fig. 3.10c-d). At high solid fraction $\bar{\varphi}$, the maximum D^* vanishes in the case of wall trapping, whereas for sliding, it reaches a plateau where displacement is dominated by surface motion. Interestingly, the optimal run times τ^* for both sliding and trapping remain comparable up to a high solid fraction ($\bar{\varphi} \simeq 0.4$), suggesting that environments with different surface properties can lead to similar optimal strategies. Whether this conclusion holds beyond disk-shaped obstacles remains an open question, though the framework used here can be extended to other microstructures.

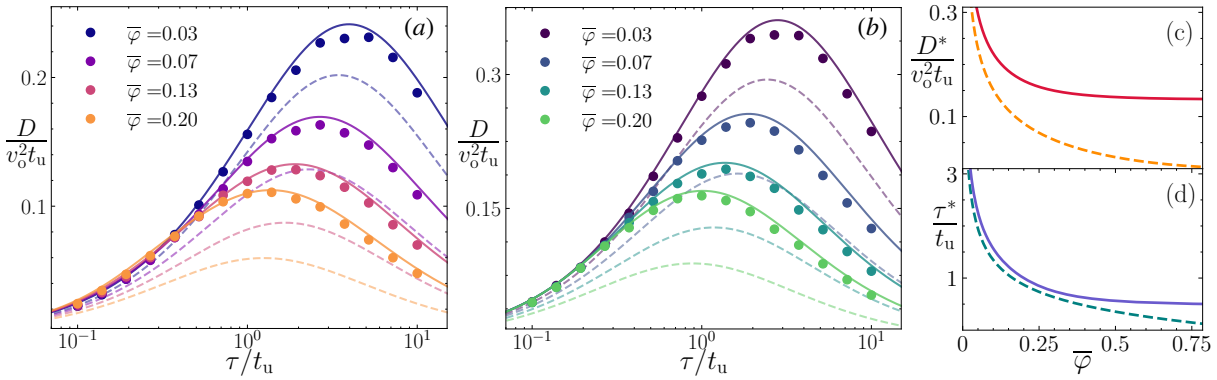

Figure 3.10: **Diffusivities with Surface Motion.** (a-b) Diffusivity as a function of mean run time, comparing numerical data (points) with model predictions (solid line) for two swimming patterns: RTi (a) and isotropic RR (b). Dashed lines show corresponding diffusivity without sliding (Eq. 3.10). (c-d) Maximum diffusivity D^* and optimal run time τ^* for RTi, as a function of solid fraction, with and without surface motion (solid and dashed lines, respectively). The time unit is $t_u = W/v_o$.

Comparison with Surface Motion in a Slit It is noteworthy that all diffusivity curves still exhibit a maximum and decay to zero as $\tau \to \infty$ when surface motion is considered. This contrasts with what was observed in the slit, where surface motion introduced a plateau at large τ. Beyond a critical surface velocity, the plateau overtook the maximum, causing diffusivity's dependence on τ to become monotonous (See Figs. 2.7). The key difference lies in the effect of surface motion within the two different geometries: in the slit, moving on the flat walls allows for unobstructed linear motion parallel to the confinement, significantly enhancing long-time dispersal. In porous media, however, surface motion contributes primarily to orientational correlation, which has a smaller impact on diffusivity. This distinction is especially clear in the limit $\tau \to \infty$: in the slit, diffusivity converges toward one-dimensional ballistic motion, whereas in porous media, particles remain mostly localized, orbiting a single obstacle for long periods, causing diffusivity to approach zero as in the case without motion at the surface.

3.5 Conclusions: Final Remarks and Perspectives

This work presented in this chapter demonstrates that the long-time dispersal of motile microorganisms in porous media is governed by a generic law, which is rooted in the invariance of the mean free path (Eq. 3.11). The concept of Cauchy universality has been known in contexts such as wave propagation through scattering media [186, 187] and the residence time of bacteria in microstructures [188]. This work shows that despite the diversity of swimming strategies and porous environments, microbial dispersal can be understood within a common and unified framework.

Extension to ABP-only Case Although the model in this work has been applied to run-and-tumble motion, it is also applicable to non-tumbling cases, such as active Brownian particles. In this case, it is assumed that the ABP has zero velocity at the

surface and that escape is governed by rotational diffusion[12]. This process has been studied in detail [146], and the mean time spent at the wall is given by $\tau_s = \zeta\tau_p$, where ζ is a known prefactor. Replacing τ with τ_p, $\xi \equiv \tau_p/\tau_p^*$, $a = \mathcal{T}/\zeta$, and $b = \mathcal{T}/\bar{\beta}$, Eq. 3.10 remains valid, indicating that the diffusivity $D(\tau_p)$ still follows the same generic curve. The maximum diffusivity is achieved at:

$$\tau_p^* = \frac{\mathcal{T}}{\sqrt{\zeta\bar{\beta}}}, \qquad \mathcal{D}^* = \frac{\tau_p^*}{2+c}K(\bar{\varphi}), \quad c = \sqrt{\zeta/\bar{\beta}} + \sqrt{\bar{\beta}/\zeta}. \tag{3.37}$$

The optimal persistence time remains proportional to the mean chord length of the medium, with the prefactor depending on the specific escape behavior.

Significance and Insight In natural porous environments where surface trapping [12, 133] is a good approximation—such as in the rough or irregular boundaries found in rocks, soils, gels, and tissues (see Fig. 1.6)—the expression for diffusivity in Eqs. (3.16)-(3.18) proves to be remarkably generic. This means that materials with very different microstructures may lead to similar long-time dispersal characteristics, as most microstructural properties are irrelevant, with the mean chord length of the material being the dominant factor in determining long-time dispersal. Furthermore, the mean chord length is not only the dominant factor but also a simpler quantity to access experimentally, possibly offering a practical means to estimate long-time dispersal without requiring detailed knowledge of the porous medium's full morphology [181].

Comparison with Previous Literature The connection between dispersal and the invariance of the mean-free path provides new insights into previous findings in the literature. Mattingly [131] developped a model for diffusivity in porous media, focusing on ballistic runs and isotropic tumbles in randomly placed overlapping disks. The resulting diffusivity prediction, derived through homogenization methods and explicit at low solid fractions, can be recovered as a specific case of Eq. (3.10). The minimal model presented here also explains why Mattingly's claim that "one can forget almost everything about the medium when measuring diffusivity" is a broadly applicable result. Furthermore, it offers a way to revisit earlier conclusions, such as the observation in Ref. [21] that "the size of the pores, not their shape, matters" for RT polymers in disordered media. Similarly, a study on active Brownian particles in periodic media [173] emphasized that "the effective mean free path is the critical length scale governing cell transport". Both insights are consistent with the Cauchy universality described by Eq. (3.11).

Finally, it was shown numerically in Ref. [128] that a "reverse-when-stuck" swimming strategy outperforms other strategies. The current model generalizes this conclusion by predicting that the optimal strategy for maximizing diffusivity in organisms with surface-sensing abilities would involve immediate escape after surface contact, and reorientation parallel, not normal, to the surface[13]. This conclusion is not specific to any particular porous medium, making it broadly applicable.

[12] The particle escapes when its direction points into the free space.

[13] Setting $\tau_s = 0$ in Eq. (1) maximizes the first term, while the second term is maximized for ballistic motion and small $\bar{\beta}$.

Future Directions Several avenues for future research emerge from this work. First, the impact of non-Poissonian processes on tumbling and trapping [12,159] needs to be explored further. Additionally, anisotropic dispersal induced by external fields or symmetry-breaking microstructures should be characterized, as well as the effects of chemotaxis or fluid flows [189]. Second, more understanding is required to delineate the conditions under which Cauchy invariance holds [177].

CHAPTER 4

Motion under Constraints: Novel Magnetotactic Bacteria

Contents of this Chapter

This last results chapter of the thesis transitions from the theoretical approach of the two previous chapter to a mostly experimental focus. Moreover, it reintroduces the role of taxis, a crucial factor in bacterial motility that was not considered in the earlier chapters. The emphasis here is on Magnetotactic Bacteria (MTB), which had been introduced in the introduction of the manuscript, in Sec. 1.1.2.

Outline of the Chapter The chapter starts by clearly defining the background and motivation behind the study in Sec. 4.1. Then, Sec. 4.2 and 4.3 are two results sections. The first investigates the magnetic response and basic motility features of a novel MTB strain, for which only rough estimates are currently available in literature. The second focuses on early findings concerning a newly observed phenomenon involving motion under magnetic constraints and in the presence of solid interfaces. This latter section remains largely open-ended, but it offers a foundation for future research.

4.1 Background and Motivation

This section reintroduces key topics initially covered in Sec.1.1.2, which were only minimally addressed in Chapters 2-3. Specifically, it delves deeper into magnetotactic bacteria and the role of motility responses to external signals. The primary focus is on the SS-5 strain, a novel MTB specie discovered ten years ago [190], which has garnered significant interest in recent years.

4.1.1 Biological Swimmers with a Magnet

MTB are a diverse group of motile microorganisms that navigate along magnetic field lines using intracellular structures known as magnetosomes. These are nanometric, ferromagnetic crystals stored within linear intra-cellular membranes, which enable the bacterium to respond to external magnetic fields. This unique ability forms a navigation system that merges micro-scale motility with nanometric magnets, alongside other internal motility responses such as aerotaxis. Unsurprisingly, this combination gives rise to a biological swimmer that exhibits a complex and fascinating pattern of motion [24, 25].

Reasons to Study MTB In recent years, a multi-disciplinary research has grown around MTB. From a physicist's perspective, magnetotaxis introduces a clear physical element to the complex biological problem of bacterial movement, as the interaction between a magnetic field and a ferromagnetic agent is a well-established problem of classical physics. In terms of applications, MTB's unique properties have been employed and are currently being tested in innovative techniques. In medical applications, *Magnetic Hyperthermia* is a developing cancer treatment that uses heat generated by magnetosomes subjected to an alternating magnetic field, to target and selectively destroy tumor cells [191]. In ecological applications, MTB strain BW-1 has been found to biomineralize copper sulfide nanoparticles, opening new possibilities for biological metal recovery [192]. Moreover, different studies have looked into MTB for drug delivery systems [25, 193] or as possible replacements of contrast agents [194, 195]. All of these applications require a comprehensive predictive framework for their motion, which remains incomplete. Gaining deeper insight into their motility in response to applied fields could enable "remote control" of their movement at the micro-scale through the application of appropriate external fields. This issue is also closely related to broader topics such as active transport and magnetic alignment, contributing to the development of magnetically driven microagents. [196, 197].

MSR-1 Strain: What is Known? The understanding of MTB motility comes primarily from studies done on the MSR-1 strain, one of the most studied species of the family. Key features include its helical cell morphology and movement mechanisms. MSR-1 has a linear magnetosome chain and is propelled by two flagella on each side of its cell body (See Fig.4.1). Its motion characteristics, such as propulsion velocities and swimming patterns, are well documented. Like most MTB, MSR-1 exhibits a run-reverse swimming pattern through motor switching[1] [24]. Magnetic responses in MSR-1 have been modeled by de-

[1]Earlier chapters introduced run-reverse as a motility of bacteria with a single flagellum, which can either propel the cell forwards or backwards. This pattern also applies to MSR-1, which has instead two

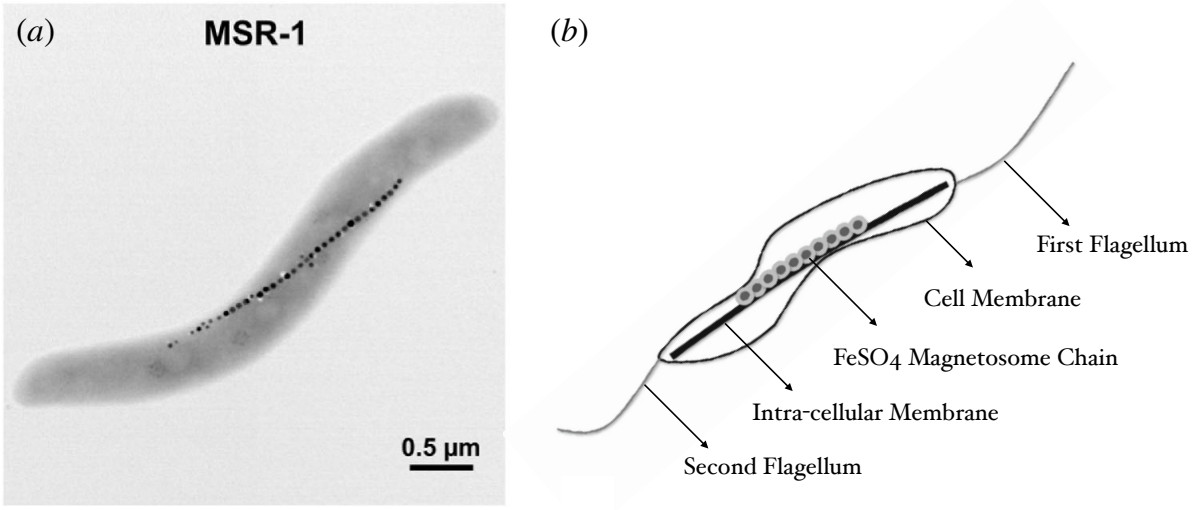

Figure 4.1: **Magnetotactic bacteria MSR-1 strain.** (a) Electron microscopy image of one MSR-1 cell (flagella not visible). (b) Schematic representation of cell features: cell morphology, position of flagella and magnetosomes chain. Adapted from [199].

scribing the bacterium as an ABP with an added magnetic dipole aligned with its motion, leading to various methods and estimates of its characteristic magnetic moment [198–201]. Although models of aerotaxis have attempted to capture motility responses to oxygen gradients, detailed studies on "magneto-aerotaxis"—the combined response to oxygen and magnetic fields—are still needed [99, 199]. Other motility-related research includes interactions with flow fields and collective behavior, such as the destabilization into mobile clusters under certain conditions, when dense suspensions are exposed to external fields and opposing flows [200]. Recent and ongoing studies continue to explore MSR-1 motility, investigating swarming behaviors in high-density suspensions [202] and directed motion within flows [203] and confined environments [204].

4.1.2 Novel SS-5 Strain

This section introduces the specific bacterial strain that will be used in the experiments presented in Sec. 4.2-4.3.

SS-5 Strain: What is Known? The strain of interest is named SS-5, originally found in what remains of Salton Sea, a saline lake turned toxic and inhospitable to life by unregulated agriculture [205]. Although discovered ten years ago, only recent developments have established stable and reproducible methods to culture this strain in the lab, therefore not much is known about the specie. The currently available estimates of SS-5's characteristics include its rod-shaped cell morphology (See Fig. 4.2), with an average length of 2.5 µm and an average width of 1.2 µm; its propulsion velocity estimated at approximately 55 µm/s; it's magnetic response due to an average of 20 iron-oxide magnetosomes, each with an average size of about 80 nm [190]. Lastly, SS-5 is known to perform microaerotaxis, leading to accumulation at particularly low oxygen, at least 21 times lower than

flagella at each end of its elongated cell body.

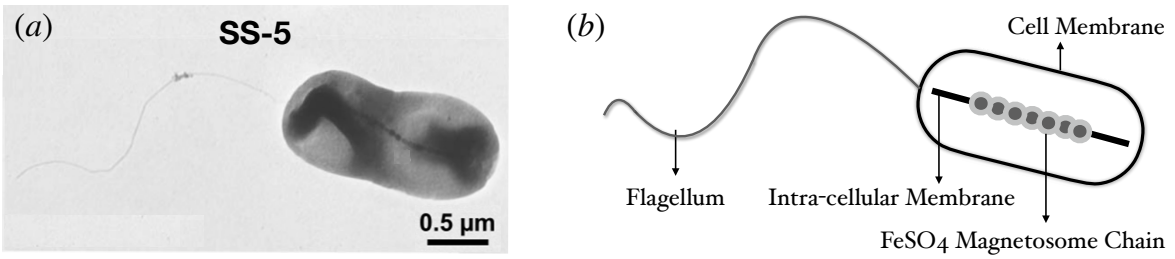

Figure 4.2: **Magnetotactic bacteria SS-5 strain.** (a) Electron microscopy image of one SS-5 cell. Schematic representation of cell motility features: cell morphology, position of flagellum and magnetosomes chain. Adapted from [24].

atmospheric levels [24].

Why a New Strain? It's natural to ask why one would choose a novel strain over MSR-1, for which many basic aspects of motility are already well documented. The reason why SS-5 has attracted interest for physical studies is due to its simple rod-shaped cell body, resembling that of *E. coli*, and its propulsion via a single flagellum. This straightforward shape offers clear advantages in modeling, particularly when compared to the more complex helix-shaped, biflagellated MSR-1. This simplicity is especially important, for instance, if the aim is to model interactions between the bacterium and solid obstacles. With SS-5, simplifying assumptions and comparisons with existing results for *E. coli* are feasible, whereas the complex two-motor system of MSR-1 may introduce unique dynamics that require new approaches. Additionally, the biological properties of SS-5 have attracted attention in related fields, leading to its complete genome being recently sequenced [206], making it a strong candidate for future studies and applications that may require characterization of its motility.

4.2 Magnetic Response of the SS-5 Strain

This section investigates the motility response of the SS-5 strain to magnetic fields in bulk fluid. Sec. 4.2.1 discusses the experimental setup used, while Secs. 4.2.2-4.2.3 focus on results and modeling. The work in this section results from a collaboration with Valentin Poncet, who worked on this part of the project during his M2 internship, and has since become a PhD student, currently working with SS-5 at Institut Lumière Matière.

4.2.1 Experimental Setup

Growing SS-5 in the Lab The SS-5 strain is cultured following the protocol detailed in Appendix B. The growth process is complex and lengthy, relying on semi-solid cultures for micro-aerophilic bacteria that enable controlled anoxia. Additionally, SS-5 uses inorganic carbon sources (sodium bicarbonate) for growth, resulting in slow duplication times, estimated to be around 24 hours—nearly two orders of magnitude longer than that of *E. coli*. Typically, cultures reach optimal growth conditions about 7 days after

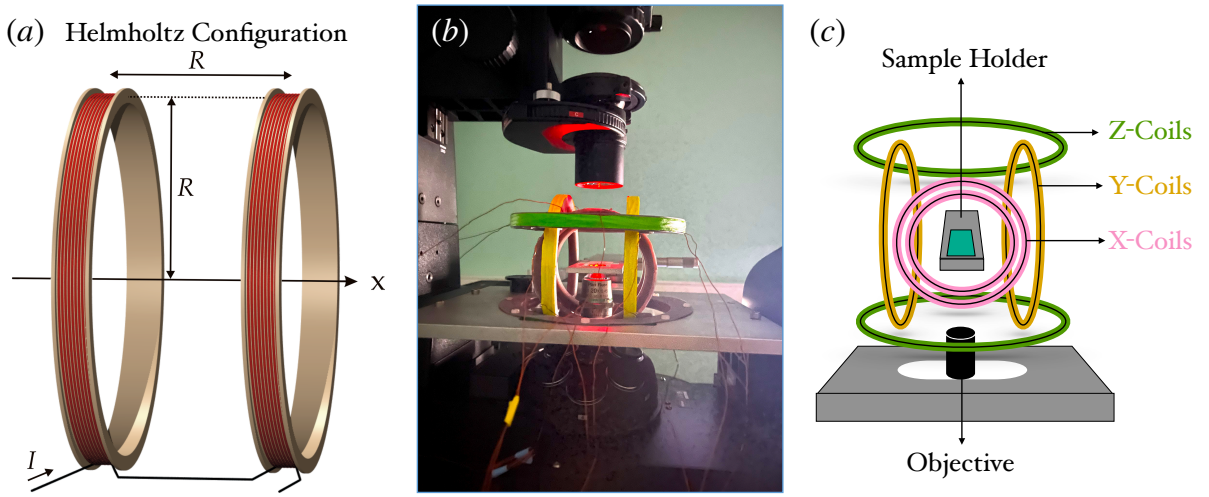

Figure 4.3: **Experimental Setup.** (a) Helmholtz coils configuration: two parallel coils of radius R, spaced R, carrying an equal electric current in the same direction. (b) Observation setup: an inverted microscope with custom sample holder, allowing for three Helmotz pairs to be placed around the sample. (c) Schematics: the three coils are placed on three orthogonal (x,y,z) axis, without obstructing the field of view.

refresh, at which point the bacteria can be transferred from the semi-solid medium to a swimming medium, following the protocol in Appendix B.2. Samples are then prepared and observed using a custom microscope setup, as detailed below.

3-Axis Control of Applied Fields To characterize bacterial movement under precisely applied magnetic fields, an inverted microscope was modified with a custom sample holder designed to accommodate coils. The setup and schematics are illustrated in Fig.4.3. Specifically, a pair of Helmholtz coils (See Fig.4.3a) is centered around the sample for each axis. This configuration generates uniform and constant magnetic fields within the central region of the coils. To achieve three-dimensional control over the applied field, three pairs of Helmholtz coils, totaling six coils, are arranged in a three-axis setup (See Fig. 4.3b-c). Given the geometric constraints of the Helmholtz configuration and the following requirements: 1) the coils must not impede the objective's field of view, 2) the sample holder must be precisely centered to maintain uniformity of the applied field, and 3) the applied fields needed to reach a maximum of 2 mT; a lot of trial and error was necessary to develop a successful holding system for the three pairs of intertwined coils surrounding the sample holder. In the final setup, each set of coils is connected to an independent power supply, and calibration measurements with a Gauss-meter were conducted to measure the strengths of the applied fields, and to determine the intensity-to-field relationship for each set[2].

[2]The intensity of field in the center of Helmotz coils can be derived from the Biot-Savart Law: $B = (4/5)^{3/2}\mu_0 nI/R$, where n is the number of turns in each coil and $\mu_0 = 4\pi \times 10^{-7}$T m A^{-1}. Calibration measures were made to ensure linearity and to better estimate the linear coefficient of each set of coils.

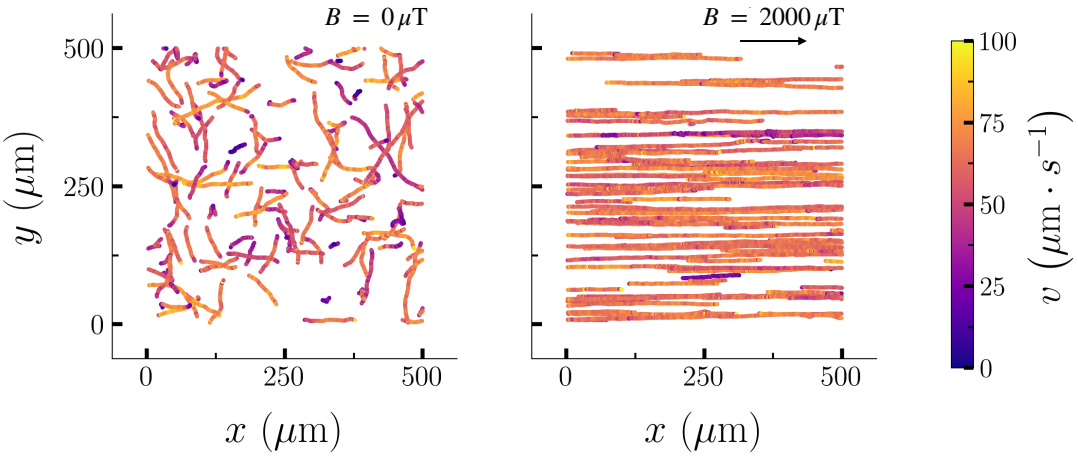

Figure 4.4: **Bacterial Tracks with and without Applied Field.** Examples of experimental tracks of SS-5 without applied field (left) and with applied field in the x-direction (right). Coloured points shows the recorded instantaneous velocity

Contribution of Earth's Magnetic Field In the upcoming analyses, it is crucial to consider the total magnetic field affecting the bacteria[3], not just the one applied by the coils. To do so, the microscope is oriented with the y-axis pointing North. Then, according to measurements done within the area of Lyon, the main contribution of the Earth's field is primarily in the z-axis (approximately 50 µT) and in the y-axis (approximately 20 µT). The field in z is consistently cancelled out in all observations, by imposing an equal and opposed field. This guarantees that bacteria are subject to fields that are parallel to the plane of observation of the microscope. The y-axis contribution is included in the estimates of imposed magnetic fields reported hereafter.

4.2.2 Transport under Magnetic Fields

This section investigates the motion of SS-5 in response to magnetic fields. Bacterial motion is recorded using samples prepared according to the methods described in Appendix B.2. Recordings are performed at a low-to-intermediate cell density within the field of view, typically between 10^{-4} and 10^{-3} cells/µm^2. This density range provides sufficient statistics while minimizing particle-particle interactions. As a result, subsequent analyses assume the dilute limit, ignoring the effects of bacterial collisions.

Bacterial Tracks Experimental trajectories are obtained using a tracking algorithm based on Python library `trackPy`, as detailed in Appendix B.2.2. Sample trajectories, depicted in Fig. 4.4, demonstrate the bacteria's motion with and without an external magnetic field. The trajectories reveal a significant alignment effect on the bacteria's orientation due to the magnetic field, in contrast to the seemingly random motion observed in the zero-field scenario. Notably, since the applied field is parallel to the field of view, strong fields also result in longer recorded trajectories, as bacteria constrained by the field remain within the field of view for longer periods.

[3]In nature, it is likely that the bacteria can sense the Earth's geomagnetic field and use it for navigation, therefore it is expected that its contribution will not be negligible in our observations.

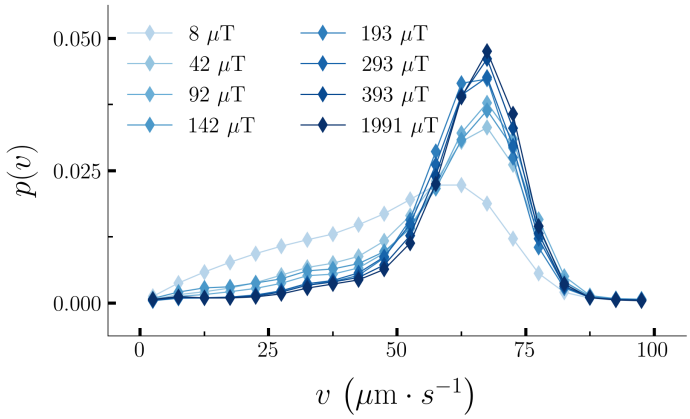

Figure 4.5: **Velocity distribution of SS-5.** Normalized distributions of instantaneous velocities recorded in bulk fluid under different applied magnetic fields. The measured velocities are the projections of the actual cell velocities onto the (x, y) observation plane.

Instantaneous Velocity A first natural question is whether the magnetic field influences only the orientation of the bacteria or also alters their swimming dynamics, such as by increasing their velocity. The curves in Fig. 4.5 shows the distribution of measured instantaneous velocities under varying field strengths. Data indicates a constant peak at around 60 µm s^{-1} for all fields considered, a value is consistent with the only available estimates in literature for SS-5 [24,190]. The spread of the distributions around the maximum remains consistent across different field strengths, except for the velocity distribution at 8 µT. At near-zero field, the distribution shows a flat tail extending toward zero, likely due to bacteria moving in and out of the 2D observation plane. In contrast, when a field constrains motion within the observation plane, these 3D effects are minimized.

Orientation Further analysis focuses on the orientation of the bacteria relative to the magnetic field. Figure 4.6a displays a histogram of particle orientations with respect to the field direction, for different field strength. A clear trend emerges: stronger fields result in a more pronounced alignment, with distributions increasingly peaked around zero. Conversely, in the absence of a field, the distribution is flat, indicating no directional bias.

What about Reverse Events? Assuming that the interaction with the field only involves alignment, the run-reverse motion of SS-5 raises questions. In earlier chapters, run-reverse motion was understood as stochastic inversions of the direction of motion which occur at a fixed rate. If this were the case, an orienting field would restrict movement along its direction, but the back-and-forth dynamics would not cause the bacteria to drift either towards, or against, the field orientation (See Fig 4.7a). However, what is observed for SS-5 is that, while reverse events occasionally occur, all cells drift towards the orientation of the field. This can be qualitatively explained by two factors: 1) bacteria move primarily in the direction of the field, while cells are considered to be in pusher-mode[4]. When a reversal induces the transition from pushing to pulling, SS-5 move against the field direction only for brief periods (typically less than 1 second), before a second reverse occurs to switch back to pushing (See Fig 4.7b). 2) Such "double reversals"—a

[4]Since the cell body must remain aligned with the field, the two motor states can be directly "seen" as whether the particle is moving with the field, or against it. The convention used here is that pusher state corresponds to motion in the direction of the field, while those moving against it are in a pulling state. However, this assumption should be verified through direct observation of SS-5 flagellar propulsion, which are currently unavailable.

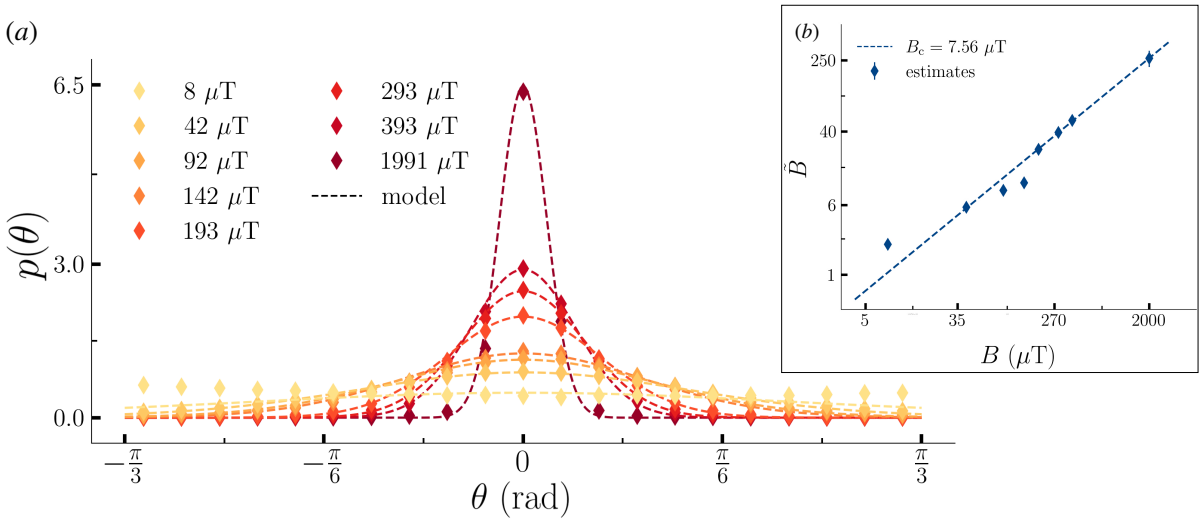

Figure 4.6: **Alignment under different applied fields**. (a) Normalized distribution of instantaneous orientation relative to the field direction for various applied field strengths. Experimental data (points) are fitted using the model (dotted lines) described in Section 4.2.3. (b) Values of $\tilde{B}$ obtained by fitting curves at different applied fields B, along with a linear regression (dotted line) which gives an estimate of $B_c = \tilde{B}/B$.

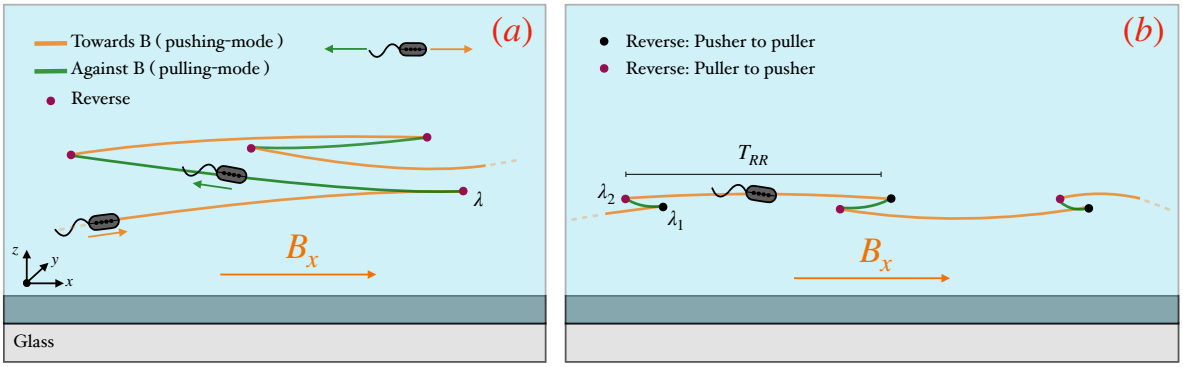

Figure 4.7: **Run-reverse of SS-5 at air oxygen levels.** (a) Example of run-reverse motion at a constant reverse rate λ under an orienting field B_x: bacteria go back-and-forth, switching from pusher to puller, without drifting in the direction of the field. This behaviour is not consistent with observations. (b) Example of run-reverse motion consistent with observations of SS-5: motion predominantly occurs in the direction of the field (pushing mode), while reversals are more frequent in the pulling mode ($\lambda_2 > \lambda_1$). Time spent in uninterrupted pushing mode T_{RR} is estimated to be 5-10 seconds, while typical times spent pulling are below 1 second.

switch from pusher to puller, followed quickly by a second switch back to pusher—are relatively rare, occurring once every 5-10 seconds. As a result, motion predominantly occurs in "pusher-mode", with reversals having a minimal impact on the dynamics[5]. Notably, these considerations apply only to experiments conducted at air oxygen levels. Since the aerotactic response of SS-5 targets low oxygen levels (typically 21 times below atmospheric levels [24]), the influence and dynamics of reversals are expected to change under lower oxygen conditions.

4.2.3 Modeling Motion and Magnetic Alignment

In this section, a simplified physical model is discussed which characterizes a bacterium swimming under the influence of an imposed magnetic field. This basic model, consisting of an ABP with a magnetic dipole, allows to understand the underlying physical principles of motion and deduce quantitative estimates. Based on earlier discussions, reverse events are neglected in the model and the dilute limit is considered.

Model A bacterium is modeled as an active spherical particle of radius R, with a magnetic moment $\mathbf{m_0}$, moving at constant velocity v_0 in a fluid with viscosity η. It is assumed that the direction of the magnetic moment aligns with the direction of motion, represented by the vector $\mathbf{v}$. The following analysis is done in a reference frame where the x-axis aligns with the direction of the total external magnetic field, hereinafter referred to as B. Initially, movement is considered to occur on a two-dimensional plane, an assumption which could be justified in experiments with high field strengths, where motion is strongly confined to the plane of observation by the magnetic field.

Dynamics The orientation of the particle within this reference frame, denoted θ, results from the equilibrium of different torques. These include the viscous torque, $\dot{\theta}\gamma_\mathrm{r}$, where $\gamma_\mathrm{r} = 8\pi\eta R^3$ is the rotational friction coefficient; the torque exerted by the magnetic field, $\mathbf{m_0} \times \mathbf{B}$; and a stochastic torque representing rotational diffusion, given by $\sqrt{2D_\mathrm{r}}\gamma_\mathrm{r}\xi(t)$, with ξ being delta-correlated white noise. At low Reynolds numbers, the torque balance equation can be expressed as an over-damped Langevin equation (See Sec. 1.2.1), yielding:

$$\dot{\theta} = \frac{-m_0 B \sin(\theta)}{\gamma_\mathrm{r}} + \sqrt{2D_\mathrm{r}}\zeta(t)\,. \tag{4.1}$$

Correspondingly, the associated Fokker-Planck equation (derivation not shown) is:

$$\frac{\partial p(\theta)}{\partial t} = \frac{m_0 B}{\gamma_\mathrm{r}} \frac{\partial \sin(\theta) p(\theta)}{\partial \theta} + D_\mathrm{r} \frac{\partial^2 p(\theta)}{\partial \theta^2}\,. \tag{4.2}$$

Where $p(\theta)$ is the probability distribution of particle orientation with respect to the field direction. The stationary solution to this problem is known [200], and expressed as:

$$p_\mathrm{2D}(\theta) = \frac{e^{\tilde{B}\cos(\theta)}}{2\pi I_0(\tilde{B})}\,, \tag{4.3}$$

[5] In terms of run-reverse dynamics, this leads to assume that reversals can't be characterised by a single reverse rate, but rather involves two reverse rates each associated to its own motor-state.

where $\tilde{B} = B/B_c$, with $B_c = \gamma_r D_r/m_0$, and I_k denotes the k-th order modified Bessel function.

The two-dimensional assumption may not be accurate for the comparison with experimental data, as from observations at low and intermediate fields it is clear that bacteria can swim in three dimensions within the depth of field. To address this, the model considers the observed projection of θ, termed Θ, on the observation plane. The probability density function for Θ can be obtained following an analogous three-dimensional formulation [200], which only involves more complex calculations (not shown), yielding:

$$p_{3D}(\Theta) = \frac{I_1(\tilde{B}\cos(\Theta)) + L_{-1}(\tilde{B}\cos(\Theta))}{4\sinh(\tilde{B})}, \tag{4.4}$$

where L_k is the k-th order of the modified Struve function.

Comparison with Experimental Data Despite the model's simplicity, Eq. 4.4 effectively fits experimental data across a range of magnetic field strengths, as illustrated in Fig.4.6a. For each fit on experimental curves, an estimate for $\tilde{B}$ is derived and plotted as a function of the imposed magnetic field B in Fig.4.6b. The observed linearity across all tested fields suggests that the magnetic response is governed by a roughly constant coefficient $B_c = \gamma_r D_r/m_0$. With γ_r and D_r assumed to be independent of the applied field, this result would indicate that motion is described by a constant magnetic dipole. This finding supports the initial hypothesis that the magnetosome chain acts as a magnetic dipole for the cell body, and its role "motility-wise" is to passively orient the cell body along magnetic field lines. In conclusion, at air oxygen levels, SS-5's motion resembles that of an ABP with an added constant magnetic dipole aligned in the direction of motion.

Estimate of the Magnetic Moment From the linear regression of Fig. 4.6b, a fit of $B_c \simeq 7.6\,\mu$T is obtained. Starting from this value, a rough estimate of the magnetic moment of SS-5 can be derived by employing a simplifying assumption: rotational diffusion is treated as thermal noise [6]. Thus, it is assumed that $\gamma_r D_r = k_B T$ [208], where T is the temperature during observation and k_B is the Boltzmann constant. At room temperature, this yields an estimate of m_0 on the order of $10^{-17}\,\mathrm{A}\cdot\mathrm{m}^2$. The value is roughly one order of magnitude lower than what has been reported for MSR-1, for which similar trajectory analyses yielded estimates in the range of 1 to $5\cdot10^{-16}\,\mathrm{A}\cdot\mathrm{m}^2$ [209]. Finally, bulk magnetite is known to have a saturation magnetization of 450 kA/m [198], which, given the typical sizes of magnetite crystals in bacteria, sets an upper limit of $10^{-16}\,\mathrm{A}\cdot\mathrm{m}^2$. This upper bound is consistent with the magnetic moment estimate for SS-5.

4.3 Magnetic Forcing at Solid Boundaries

Driven by curiosity, one might wonder: *what happens when an SS-5 is forced against a solid boundary by an applied field?* Earlier results on bulk motion suggest that the

[6] As explained in Sec. 1.1, thermal rotational noise is typically not accurate for bacteria, which rather require active noises with effective temperatures generally higher than the thermal case. For instance, similar analyses on MTB AMB-1 strain estimate $T_{\mathrm{eff}} \simeq 2.3T$ [207]. However, here the thermal assumption is kept, allowing comparison with studies on MSR-1 that employed the same of thermal approximation.

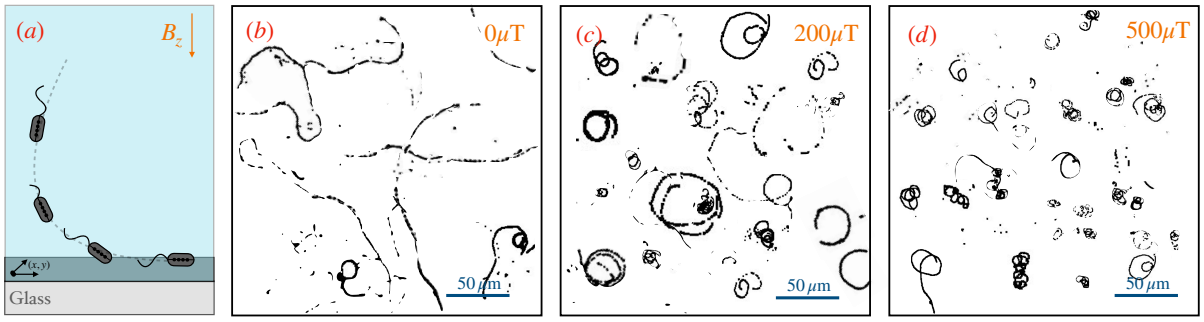

Figure 4.8: **SS-5 motion at the water/glass interface**. (a) SS-5 are forced on the glass surface by a vertically aligned field. (b,c,d) Superimposed images in the (x,y) plane, showing SS-5 trajectories at the surface under varying vertical fields. Images are treated with a binary filter and then superimposed over a 1.5-second recording period.

bacterium, constrained by the field's orientation, will collide with the wall and may remain pinned on it, due to the magnetic torque keeping the bacterium perpendicular to the wall. However, Sec. 1.3.1 had presented a wide spectrum of possible dynamics for bacteria at interfaces. Generally, pushers are hydrodynamically attracted to solid walls, leading to surface residency and, in some cases, motion on the boundary. For SS-5, this could imply that, when in pushing mode, it may be hydrodynamically inclined to move along the surface, potentially overcoming the magnetic field's constraints. In contrast, pullers are hydrodynamically repelled by surfaces. This is also relevant for SS-5, as the bacterium transitions to a puller following reverse events, potentially altering its surface dynamics. Overall, these observations indicate that the interplay between magnetic forces and solid obstacles could lead to complex behaviors, and that the initial question might be more intricate than it appears. The aim of this final chapter is to give insight on this issue.

Why Study this Topic? Besides sheer curiosity, this topic holds practical significance for various applications. As detailed in the thesis introduction, common bacterial habitats are far from homogeneous, often containing obstacles and areas of confinement. It is natural to ask whether the magnetic response of MTB could aid their navigation in such environments. Additionally, research such as those cited earlier for drug delivery [25, 193] or contrast agents [194, 195] are likely to benefit from an understanding of magnetically driven motion in the presence of obstacles. Indeed, this topic is garnering significant attention with the last years, highlighted by the recent publication of papers that explore MTB motion within porous structures and confinement [173, 203].

4.3.1 Surface Motion under Vertical Alignment

Consider the scenario where an SS-5 bacterium is directed towards a glass surface by imposing a vertical field B_z (See Fig. 4.8a). This can be easily reproduced using the experimental setup of Sec. 4.2.1. By recording the motion in (x, y), with the focal plane positioned near the bottom glass surface, bacterial motion on the surface is recorded under different strengths of B_z. Figs. 4.8 b,c,d show superimposed image sequences that illustrate recorded trajectories of bacteria swimming on the surface.

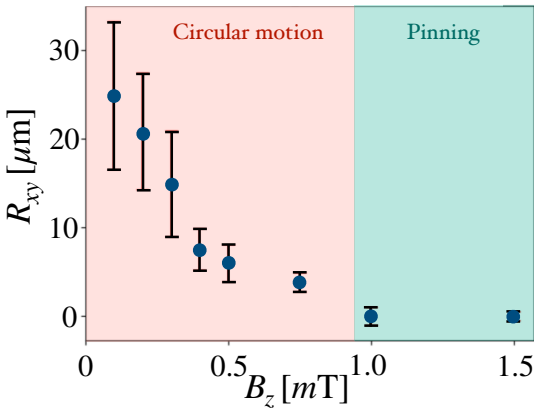

Figure 4.9: **Circular motion and pinning.** Mean radius of circular motion in the (x, y) plane as a function of the vertical magnetic field B_z. For B_z >1 mT, radii tend to zero, indicating that bacteria stop performing circular motion and are instead pinned in place by the field. Each average radius is calculated from 100 measurements of circular trajectory radii.

Without Field Figure 4.8a specifically shows the SS-5 trajectories near a glass boundary in the absence of magnetic field. Similar to *E. coli*, SS-5 move along the surface boundary as typically occurs for pusher-like swimmers. However, unlike what is typically observed for *E. coli* (See Sec. 1.3.1), SS-5 does not follow circular trajectories when moving along the surface. Instead, its motion at the surface resembles that of its movement in bulk: random and with no clear orientational bias.

With Vertical Field In contrast, when a vertical field is forcing the bacteria to orient towards the surface, SS-5 exhibit clock-wise circular motion at the water-glass interface. Comparing Fig. 4.8b-c, the typical radius of these circular trajectories appears to shrink as the strength of the vertical field increases. To give a rough estimate of this radius, an average was measured from different image sequences recorded under varying vertical field strengths. Results are shown in Fig. 4.9, confirming that the typical radius of motion decreases when higher vertical fields are considered. At sufficiently strong fields, typically above 1 mT, SS-5's circular motion ceases, and the bacterium becomes stationary on the surface, unable to move in the (x, y) plane when the field is applied.

4.3.2 Discussion: Physical Interpretation

This section discusses the circular motion and pinning behaviour observed under vertical alignment. To understand SS-5's behavior at the glass boundary, it is useful to begin with what is known about the well-studied problem of bacteria moving near solid surfaces.

Surface Motion and Other Species It is known that *E. coli* traces circular trajectories at interfaces, exhibiting clockwise (CW) motion at no-slip boundaries like water/glass interfaces [210] and counterclockwise (CCW) motion at free boundaries like water/air interfaces [211]. As shown in Fig. 4.10a, the radii of these trajectories typically range from 10 to 50 µm, and decrease with increasing temperature [212]. Similarly, monoflagellated bacteria such as *V. alginolyticus* can exhibit alternating CW and CCW circular tracks corresponding to either forward or backwards movement (see Fig. 4.10b) [213]. Finally, the radius of curvature is also observed to increase with the length of the cell body [110].

Pushers and Pullers on Flat Interfaces Far-field hydrodynamics models, which reduce swimming bacteria to flow singularities, can account for interactions with both

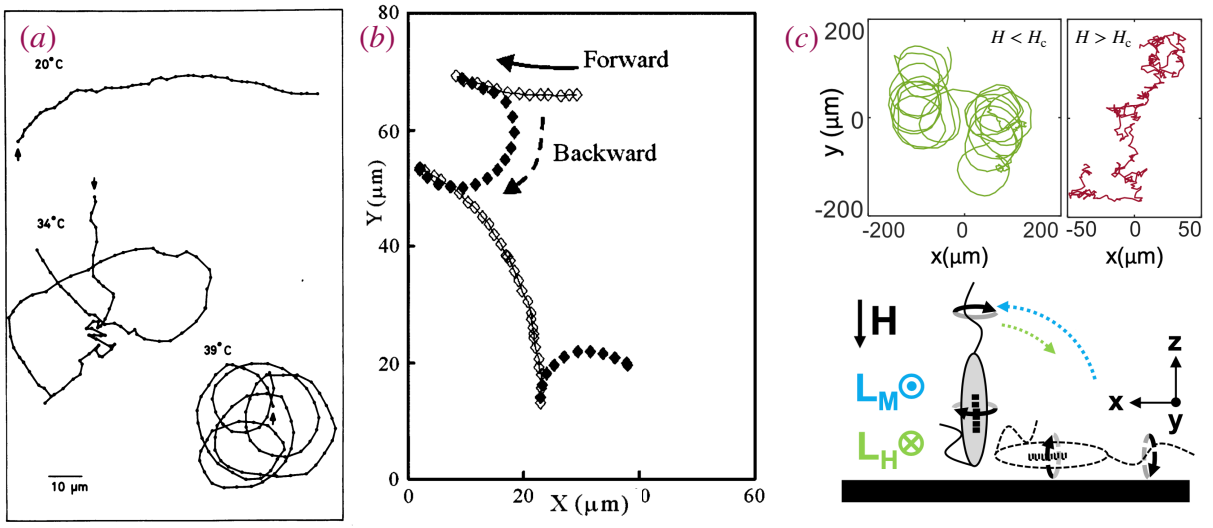

Figure 4.10: **Circular motion at interfaces, across bacterial species** (a) *E. coli* tracks at a glass/water interface show a reduction in motion radius with increasing temperatures. (b) *V. alginolyticus* tracks on glass surfaces exhibit circular motion that alternates between clockwise and counter-clockwise, depending on whether the bacterium is moving forwards or backwards. (c) MSR-1 tracks at a water/glass interface under a vertical magnetic field H. Motion switches from circular when H is below the critical value H_c to diffusive when $H > H_c$, due to competing magnetic L_M and hydrodynamic L_H torques, which respectively orient the bacteria perpendicular and parallel to the surface. From Refs. [201, 212, 213].

no-slip and free boundaries, using mirror hydrodynamic images similarly to what's classically done in electromagnetism. These models show that pushers are subject to wall-induced hydrodynamic re-orientations, which tend to rotate pushers to remain parallel to the boundary, whereas pullers are aligned perpendicularly. Furthermore, these models attribute circular trajectories at boundaries to hydrodynamic interactions from torque exerted by the swimmer on the surrounding fluid while near the surface. The predicted rotation rate scales with the strength of the torque and exhibits a non-trivial dependence on the swimmer's elongation, with the effect diminishing rapidly as the swimmer moves away from the wall [210].

The Case of MSR-1 The magnetotactic specie MSR-1 has been also observed performing circular motion at the water/glass interface under low vertical magnetic fields, transitioning instead to random diffusive motion under higher fields (see Fig. 4.10) [201]. This behavior was explained as the interplay of a magnetic torque and a surface-induced hydrodynamic torque. Consequently, motion is characterized by two states: a circular motion state dominated by the hydrodynamic torque, where the bacterium aligns parallel to the surface, and a diffusive state dominated by the magnetic torque, where the bacterium aligns perpendicular to the surface. The transition between these states occurs when the applied magnetic field exceeds a critical value B_c, predicted as

$$B_c = \frac{\gamma_r v}{m_0 L}, \tag{4.5}$$

where γ_r is the rotational drag coefficient, m_0 is the magnetic moment of the species, and v and L are the speed and size of the bacterium, respectively. For MSR-1, the critical field B_c is estimated to be around 2300 µT, though this varies with cell size and speed.

The Case of SS-5 The behavior of SS-5 under magnetic fields is comparable to that observed for MSR-1, with two predominant torques likely influencing motion on the surface. In fact, the estimate of B_c for SS-5, based on Eq. 4.5 and the parameters derived in Sec. 4.2.3, falls between 300 and 500 µT, which aligns with the observed transition to circular motion characterized by very small radii [7] (Fig. 4.9).
However, clear differences in behavior are also observed. Unlike MSR-1 and most pusher bacteria, SS-5 exhibits bulk-like random motion on the surface when no vertical field is applied. Secondly, for $B < B_c$, the radii of SS-5's circular paths decrease progressively with increasing field strength, unlike the abrupt transition from circular to diffusive motion seen in MSR-1. Finally, when $B > B_c$, SS-5 remains stationary on the (x, y) plane, in contrast to the diffusive behavior of MSR-1. These differences could be attributable to morphological differences between the mono-flagellated SS-5 and the bi-flagellated MSR-1 (see Figs. 4.1 and 4.2). The observed shrinking of radii in SS-5's motion resembles dynamics seen in *E. coli* under increasing temperatures (Fig. 4.10a), yet thermal/stochastic fluctuations are not incorporated in the model used for MSR-1, which may instead play a role in SS-5's case. Furthermore, reverse dynamics are minimally addressed, however the transition from pusher to puller likely alters hydrodynamics interaction, and may result in surface behaviours similar to those of *V. Algynolycticus* (Fig. 4.10b). Overall, these considerations suggest that a full picture of SS-5's behavior is still missing, highlighting the need for more in-depth studies to understand its unique surface interactions.

4.3.3 Perspectives: 3-Axial Digital Holography

Section 4.3.1 showed that SS-5 can performs either circular motion or is pinned at the boundary when forced on a glass surface by a vertical field. Section 4.3.2 concluded that a full understanding of this surface behaviour is not yet achieved. However, the experimental setup used so far is limited to two-dimensional recordings, whereas a thorough understanding of this phenomenon may require precise information on 3D information on the orientation of SS-5's cell body as it moves along the surface. This has led to a collaboration with Di Leonardo Lab at "*La Sapienza*" University, supported by ETN "Phymot". The goal is to reproduce the earlier work by Bianchi *et al.* [214] by using SS-5 rather than *E. coli*. This would enable single-cell 3D visualization as cells approach and move along the surface, achieved using an existing setup for three-axial digital holographic microscopy [215]. In this final perspective section, this new setup is introduced, along with the initial steps taken to apply it to the study of SS-5.

Classic and 3-Axial DHM Digital Holographic Microscopy (DHM) is a technique that allows for 3D imaging by capturing a 2D snapshot of the interference pattern (or hologram) generated by the interaction between a reference beam and light scattered by

[7] Since SS-5 is pinned to the surface at high fields, rather than exhibiting diffusive motion, it is reasonable to assume that circular motion at small radii indicates the dominance of the magnetic torque over the hydrodynamic one.

an object. This 2D hologram contains information about the 3D structure of the object, which can be reconstructed using computational techniques. The major advantage of DHM is that it does not require mechanical scanning, enabling fast acquisition rates for dynamic imaging. One significant limitation of traditional DHM is poor axial resolution. This happens because the back-propagation method struggles to resolve depth information with high precision. Three-axial digital holographic microscopy improves upon standard DHM by using three tilted beams of different wavelengths (red, green, and blue) (See Fig. 4.11a). The reconstruction from each beam provides depth information, and their overlap gives a more accurate volumetric image.

Challenges for 3-Axial DHM with SS-5 Several factors had to be adressed before the use of 3-axial DHM to study SS-5 motion:

1. Optical compatibility: bacteria must be optically compatible with DHM[8]. *A priori*, this is a particularly relevant inquiry for MTB, as magnetite has a refractive index of around 2.42, a much larger value than typical refractive indexes of cells.

2. Aspect ratio and image distortion: 3-axis DHM is suited for rod-shaped bacteria like *E. coli* (aspect ratio $\sim$4), where the orientation of the cell body can be resolved. Each of the color channels produces its own volumetric image, but the focal region of each channel is elongated along the respective illumination axis. This elongation can lead to axially stretched images even when the product of the three different reconstruction is considered. Consequently, reconstructed cells appear dilated along the z-axis. If the observed cell is sufficiently elongated, this stretching artifact can still allow for the long axis to dominate in the reconstruction. For less elongated bacteria like SS-5 (aspect ratio $\sim$2), this elongation could mask the orientation signal, leading to inaccurate measurements of the cell's true orientation.

3. Stabilization for motion capture: In previous experiments with E. coli, optical tweezers were necesary to to localise and center the bacteria in the field of view, which were then recorded after being released after the optical trap. This is a practical necessity to record fast-moving objects at high magnification (between 60 and 100X) and frame rates (>100 fps). However, optical tweezers for SS-5 have not been developed yet.

4. Magnetic field: The project aims to study bacterial motion under vertically applied magnetic fields, ideally requiring Helmholtz coils around the sample. However, integrating these coils into the 3-axis DHM setup is challenging, as the existing arrangement already requires precise alignment of the three tilted beams, leaving little room for additional equipment.

[8]DHM relies on the refractive index difference between the bacterium and the surrounding medium to generate a clear hologram. If the refractive index contrast is too low, scattering will be insufficient for proper reconstruction. If too high, excessive or multiple scattering could distort the image.

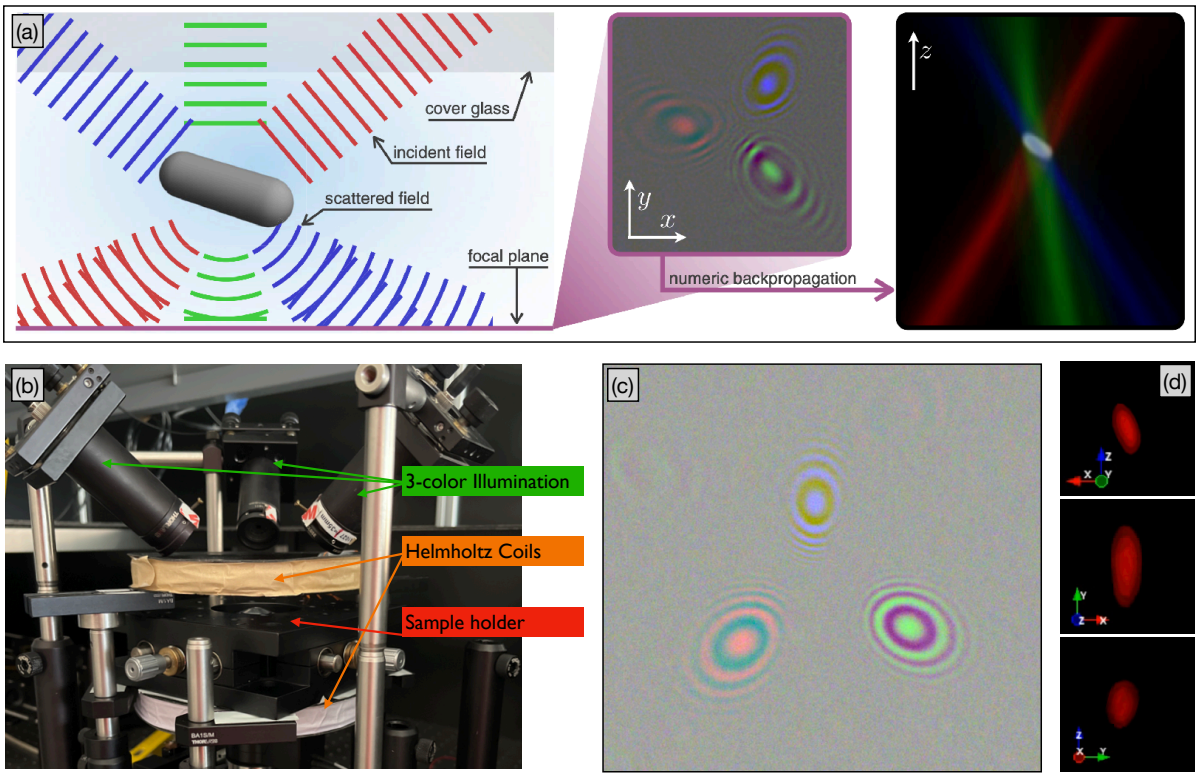

Figure 4.11: **3-Axis Holographic Microscopy.** (a) Working principle of the method: samples are illuminated by three partially coherent beams having different colors and directions; the resulting holograms from the interference between scattered and unscattered light are acquired by a RGB camera; A volumetric image of the sample is obtained as the overlap of three independent reconstructions [214, 215]. (b) Modified setup with the addition of a Helmholtz coil around the sample holder. (c) Raw image of the hologram of an SS-5 cell. (d) Re-constructed SS-5 cell body from different view-points in one frame. The (x, y) view (middle inset) shows that elongation can be resolved outside of the z-axis.

Ongoing Developments Several attempts have been made to record, reconstruct, and analyze SS-5 motion using the 3-axis DHM setup. Initial results confirm that the bacteria are optically compatible with the technique. Multiple configurations were tested to integrate Helmholtz coils into the DHM setup, and a recent solution incorporates large Helmholtz coils around the illumination stage, enabling the generation of vertical magnetic fields during observations (Fig. 4.11b). Interestingly, this addition also addressed the lack of optical tweezers, as the magnetic response can now be used to immobilize the bacteria with strong vertical fields, effectively replacing tweezers. Several reconstructions have been performed (Fig. 4.11c-d), but it's still under review whether the low aspect ratio of SS-5 significantly affects the accuracy of orientation measurements. Early results show promising reconstructions, where the cell body appears clear and elongated on the focal plane, but quantifying the accuracy of the 3D reconstructions remains challenging. Methods are currently being explored to assess, and possibly correct, the z-axis elongation, including potential post-processing algorithms to mitigate the reconstruction artifact.

Current State While significant progress has been made in adapting the 3-axis DHM setup to study SS-5, the current protocols require further refining and testing to make actual data that can be used and studied. For now, these preliminary results provide a solid foundation for continued exploration.

4.4 Conclusions

The final results chapter has shifted focus from the theoretical groundwork laid in earlier chapters to an experimental investigation, emphasizing bacterial motility under external stimuli. The reintroduction of magnetotaxis provides a new dimension to the study, with SS-5, a novel MTB strain, taking center stage. The chapter outlines both the background and the motivation for studying this strain, highlighting the significance of magnetotaxis as a model for understanding physical interactions in bacterial movement. A comparison was drawn between the well-studied MSR-1 strain and the novel SS-5, emphasizing the advantages of SS-5's simpler morphology for modeling motility in complex environments.

A basic characterisation of SS-5's magnetic response under controlled experimental conditions was presented, providing key insights into its motility. This required the development of a custom microscope setup, using Helmholtz coils enabled precise field control. Additionally, a simplified physical model was presented and able to describe SS-5 motion as the one of an ABP with an added magnetic dipole. The model fits the experimental data, and allows for a rough estimate of the specie's magnetic moment. This analysis provides a necessary foundational understanding of the motion of the novel strain, setting the stage for future experiments.

The last section of the chapter examined SS-5's behavior under vertical magnetic fields near solid boundaries. A new behaviour was observed: without a field, SS-5 moves randomly along surfaces, but under a vertical field, it exhibits either circular motion or is pinned in place, depending on the strength of the applied field. This behaviour highlights complex interplay between magnetic forces and hydrodynamic interactions at boundaries, which can't be fully understood by the existing frameworks in literature. Early results using 3-axis digital holography offer a new promising path to better understanding SS-5's surface motion. Although initial findings are promising, the study remains largely open-ended, with further investigation and data needed to draw meaningful conclusions.

In terms of perspectives, this work was envisioned as a foundation for future projects, and that vision has already come to fruition—not only through a collaboration with Rome, but more significantly through the work of another standalone PhD project. This endeavor is now led by former M2 intern, fellow PhD student, and dear friend Valentin Poncet. Over the past two years, it has evolved into a comprehensive study of SS-5's aerotaxis and has already produced promising new results. For this reason, despite the modest scope and unfinished nature of the results presented here, I personally consider this work a success. It has sparked new collaborations, inspired further research, and set in motion projects that will hopefully continue to evolve well beyond the timeline of this thesis.

Conclusions and Future Directions

"You don't have to decide now, but you have to start prospecting your future."

Cécile

This thesis has explored bacterial motion in confinement with a specific focus on dispersal, optimality and universal behaviours. The study presented theoretical and experimental results, characterising motion across diverse environments, species and dynamics. This conclusion section summarizes the key insights drawn from each chapter, highlighting the progress made and the questions that remain open. Lastly, it will explore perspectives and avenues for future research.

The first chapter lays the foundation for understanding bacterial motility and microswimmer behavior. While progress has been made in describing bacterial transport near surfaces and in porous environments, gaps remain in generalizing models, especially regarding surface interactions and confined motion. These gaps define the scope of the thesis and motivates the development of more comprehensive frameworks. In this context, the second chapter develops a model for diffusivity within slit-like confinement, whereas previous studies have primarily focused on accumulation and distribution profiles near walls. This work introduces a fully solvable discrete-direction model for run-and-tumble motion within a two-dimensional planar slit. The main outcome is a prediction for the diffusion coefficient, which is validated through simulations, demonstrating the robustness of the model even when the directional constraints are relaxed. Additionally, the model reveals that optimal transport occurs when the mean run time matches the confinement size, a finding with important implications for motility in confined environments. Lastly, the model is also extended to account for surface motion, and the chapter discusses its impact on long-time dispersal.

Building on the exploration of confined motion, the third chapter aimed instead to understand dispersal in porous media, originally motivated by the potential for driven motion through external fields. However, the study revealed richer, unexpected behaviors in the absence of such fields. This chapter introduces a unifying framework for understanding the long-time dispersal of motile microorganisms in porous media, based on

the invariance of the mean free path, also referred to as Cauchy Universality. Dispersal follows a generic law, with the mean chord length of the medium emerging as the key material property in predicting dispersal, a result that is confirmed numerically through simulations that cover a wide range of swimming strategies and microstructures. The proposed model is also consistent with previous findings and offers a generic framework to understand dispersal.

One of the original motivations for this PhD was to investigate dynamics under driven motion through external fields. However, theoretical and numerical investigations uncovered richer results than initially anticipated, leading to a shift in focus. While the initial plans for studying driven motion are discussed in the next section on perspectives, this original objective triggered the experimental chapter of the PhD. The experimental work focuses on SS-5, a novel magnetotactic strain with a simple cell morphology and a single flagellum, which make it an ideal candidate for physical studies on motility. Initial objectives included characterizing its driven motion under external fields, which led to the development of a custom microscope setup and provided an estimate of the magnetic moment of this new species. The experiments also revealed novel surface behaviors under vertical magnetic fields, opening new perspectives on SS-5's motility in the presence of solid boundaries.

Overall, the work presented in this thesis advances the understanding of bacterial motion in confinement, offering new insights and paving the way for future research.

Future Directions

The model developed for run-and-tumble motion in a slit offers valuable insights into a simplified version of confinement but leaves room for further exploration, particularly regarding disorder and more complex media. Moreover, the slit model assumes the simplest form of surface motion, but more specific surface behaviors observed in microswimmers, such as hydrodynamics-induced circling trajectories [110], billiard-like scattering [113], or twitching [2], could be incorporated into the existing framework. This would allow to investigate the impact of these surface behaviors on dispersal within the slit and provide insight on the advantages of various surface dynamics, though doing so may restrict the model's applicability to a narrower class of systems.

Looking ahead at the generic model proposed for dispersal in porous media, several directions for future work are possible. Cauchy universality is expected to hold in a variety of cases [177] that have yet to be tested in the context of dispersal. For instance, the model's applicability could extend to non-Poissonian processes for both tumbling and trapping [12, 159], and it would be valuable to explore the model's validity in environments featuring anisotropy. Symmetry-breaking microstructures, for example, can have far-reaching implications beyond dispersal. Asymmetric obstacles may induce phenomena such as active wetting, where particles accumulate near structures like half-disks, leading to segregation based on particle speed or characteristics [216]. Furthermore, such structures can create rectification currents, causing particles to exhibit directed motion as a result of environmental asymmetry [217]. Connecting Cauchy universality to environments with these symmetry-breaking microstructures could provide new insights into these broader phenomena. This line of inquiry also applies to other potential directions related to anisotropy, for instance in cases in which it is induced by external fields rather

than the environment geometry. For example, future work could investigate chemotactic drift driven by chemical gradients within a porous structure [189], fluid flows in confinement [123], light-driven motion as seen in microalgae [172], or magnetically-driven motion as in the case of magnetotactic bacteria [204]. Furthermore, this work has only considered stationary environments, where obstacles remain fixed over time. Future studies could consider extending the model to incorporate motile obstacles and dynamic environments [22]. Moreover, the current analysis has focused exclusively on single bacteria. While the case of an ensemble of interacting particles presents more complexity [6], future research could look into possible implications of the framework presented here on collective behaviours. Finally, the broader implications of the model could be explored beyond microorganisms. For instance, given the analogy between the random walks of motile microorganisms and polymer chains, Cauchy invariance may have potential applications for polymers in porous media and could inform the design of nano-composites [218–220].

There are multiple perspectives for the experimental chapter that warrant further exploration. One topic, briefly mentioned but not deeply examined in this thesis, is the aerotaxis of SS-5 [190], which refers to the motility response to oxygen gradients. A standalone PhD project has branched from the initial work presented here, and over the past two years, it has focused on studying this phenomenon. This has already led to the development of experimental setups that allow for controlled oxygen levels and gradients at significantly low concentrations, with the aim of providing a microscopic characterization of reverse dynamics arising from magneto-aerotaxis—motility resulting from the interplay between oxygen gradients and magnetic fields. Regarding SS-5 motion near solid boundaries, early results from the application of 3-axis digital holography [215] suggest that preparations for using this technique on SS-5 are nearing completion, paving the way for further analysis and concrete findings. This study will offer valuable insights into how SS-5 cells orient under varying levels of magnetic alignment when in the presence of a solid boundary, and how these dynamics are influenced by effects like reversals.

Additionally, merging experimental and theoretical approaches presented in this thesis offers several promising avenues. For example, magnetotactic alignment due to external fields could be considered as a source of directed transport and tested within the context of the dispersal model with Cauchy universality. This could be done through numerical studies, for instance looking at run-reverse particle that incorporate a magnetic alignment and move within idealised porous media, replicating the dynamics of magnetotactic bacteria. Alternatively, the approach could involve experimental work, replicating porous structures within microfluidic devices and investigating the dispersal of magnetotactic bacteria under different applied fields. Overall, coupling magnetotaxis—or even magneto-aerotaxis—with confinement presents a new research direction that is gaining interest [27], and the work presented here, both experimentally and theoretically, opens up further opportunities to pursue this path.

Et voilà !

Résumé en Français

Mouvement de Bactéries en Environnements Confinés

Présentation Générale. Les bactéries présentent une diversité de comportements de motilité, essentielle à leur survie au sein des environnements complexes et variés qu'elles habitent dans la nature. Comprendre ces mécanismes de motilité, en particulier dans des espaces confinés, est un sujet central dans la physique de la motilité bactérienne, mais aussi crucial pour l'écologie microbienne et le développement de technologies bio-inspirées. Cette thèse explore le transport bactérien dans des environnements confinés en s'appuyant sur des modèles théoriques, numériques et expérimentaux. Plus précisément, elle vise à caractériser le mouvement bactérien dans des canaux à parois parallèles ou dans des milieux poreux en développant de nouveaux modèles capables de prévoir la dispersion. Ces modèles sont ensuite utilisés pour comprendre comment la dispersion dépend des caractéristiques du mouvement et pour identifier des stratégies optimales qui maximisent l'exploration de l'espace. De plus, l'étude propose une première caractérisation d'une nouvelle souche de bactéries magnétotactiques, une famille unique de bactéries capables de se déplacer en suivant les champs magnétiques.

Organisation de la Thèse. La thèse est organisée en quatre chapitres. Le premier chapitre passe en revue l'état de l'art sur la recherche en motilité bactérienne, avec une attention particulière aux limites et lacunes qui motivent le reste du travail. Le deuxième chapitre développe un nouveau cadre permettant de prédire la dispersion des particules de type "Run-and-Tumble" dans des canaux à parois parallèles, et permet d'identifier la stratégie de nage optimale. Le troisième chapitre se concentre sur les milieux poreux et présente un nouveau modèle capable de prédire la diffusivité bactérienne à travers une large variété de stratégie de déplacement et de conditions environnementales. Le quatrième chapitre présente des études expérimentales sur une nouvelle souche de bactéries magnétotactiques, en examinant leur réponse magnétique et leurs interactions avec des interfaces solides.

Bilan et Perspectives. Cette thèse présente des contributions aux domaines de la motilité bactérienne et de la matière active. Les résultats présentés dans les chapitres 2 et

3 proposent deux cadres généraux avec une large applicabilité. De plus, ils fournissent un cadre unifié pour comprendre l'existence de temps de persistance optimaux maximisant la dispersion. De plus, ils fournissent un cadre unifié pour comprendre l'existence de temps de persistance optimaux maximisant la dispersion. De manière plus large, les résultats pourront être utiles pour potentielles dans des domaines allant du génie biologique à la recherche microbienne. Dans ce cadre, le chapitre 4 décrit la caractérisation physique d'une nouvelle espèce de bactéries magnétotactiques, qui présente un fort potentiel pour la recherche future et a déjà donné naissance à deux projets en cours qui se poursuivront au-delà de cette thèse.

APPENDIX A

Supplementary Results and Analyses

A.1 Numerical Methods

This section first presents a details the simulation model for motion within the slit and porous structures. Then, it presents an analysis aimed at identifying the optimal method to estimate diffusivity numerically.

A.1.1 Run-and-tumble in a Slit: Implementation

Simulation Setup The simulation of a run-and-tumble particle confined within a slit begins by integrating the equation of motion using the Euler method, using a custom `Python` code. One trajectory is generated by setting a simulation time-step Δt_{sim} and total simulation time T_{sim}. The motion is restricted to two dimensions within a planar slit, where the flat parallel walls are positioned at $y = \pm W/2$. Initially, the particle is placed at the origin with a random starting orientation and then its position and orientation are updated at each time-step, until the total simulation time has elapsed.

Bulk Motion and Swimming strategies. In the bulk region within the slit, the particle moves at a constant velocity v_{o} and undergoes two re-orientation processes. The first is rotational noise, which is modeled as standard Brownian motion. This is incorporated by integrating the angular dynamics, as described in Sec. 1.2.1, using the discretized form of Eq. 1.1 in the high Péclet number limit. The second re-orientation process is governed by tumbling events, modeled as Poisson processes occurring at rate λ. The tumbling process involves re-orientation angles that follow different distributions based on the swimming patterns. The simulation considers three specific distributions: isotropic run-and-tumble, run-reverse, and a realistic run-and-tumble case mimicking *E. coli*. These cases result in mean cosine values of the turning angles as 0, -1, and 0.375, respectively, as defined in Sec. 1.2.2.

Wall Collisions and Surface Motion. To simulate interactions with the walls, the particle's position is checked at each time step. If the y-coordinate crosses $\pm W/2$, a collision is detected. The precise collision point is calculated, and the particle's position is updated accordingly. If surface motion is included in the model, the particle chooses a random orientation parallel to the wall (either left or right) and initiates one-dimensional run-and-tumble motion along the surface. This motion excludes rotational noise and involves only tumbling events, as described in the bulk motion.

Escape from the Wall. The particle's escape from the wall is modeled as a Poissonian process with escape rate μ. When an escape event occurs, the particle detaches from the wall and re-enters the bulk fluid within the slit. The new direction of motion is chosen randomly from the half-space that points away from the surface, ensuring the particle moves back into the interior of the slit.

A.1.2 Run-and-tumble in a Porous Media: Implementation

Simulation Setup. Numerical simulations were performed using a custom Julia code based on the `MicrobeAgents.jl` library. Microorganisms are represented as non-interacting point particles moving at a constant speed v_o, with their trajectories integrated using Euler's method. Tumbles are modeled as instantaneous reorientation events, occurring according to a Poisson process with a rate of $1/\tau$. The simulation timestep is chosen as $\Delta t = \tau/200$ where τ is the average run time of the microorganism. At each timestep, rotational diffusion affects the microorganism's orientation by inducing a reorientation, the magnitude of which is sampled from a Gaussian distribution with zero mean and variance $2D_\mathrm{r}\Delta t$. Three different swimming strategies are considered: run-reverse (RR), isotropic run-and-tumble (RTi) and run-reverse-flick (RRF)

Wall Collisions and Surface Motion. At each timestep, after the new position $x(t+\Delta t)$ of the microorganism is calculated, the algorithm checks if the segment between the previous position $x(t)$ and the new position $x(t+\Delta t)$ intersects with the boundary of any object. If no intersection occurs, the new position was accepted. In cases where an intersection is detected, the intersection point is set as the microorganism's new position. Surface motion is implemented only for circular obstacles (see Sec. 3.4). In these cases, after a collision, particles move along the circular boundary, performing orbits with a tangential velocity equal to their bulk velocity. During surface motion, tumbling events could result in one of three outcomes: escape from the boundary into free space with a random orientation (probability 1/2), reversal of motion along the surface (probability 1/4), or continued motion in the same direction.

Boundary Conditions. For ordered environments, a unit cell containing a single solid object is defined, and periodic boundary conditions are applied to mimic an infinite space. For disordered environments, the geometry of a unit cell was generated using a brute-force approach, where objects are randomly positioned in space, and any overlap with previously placed objects is rejected. This process continues until the desired solid fraction $\bar{\varphi}$ is achieved. The unit cell is generated once, using a specific seed, and reused across all

simulations. To simulate infinite space, periodic boundary conditions are applied, and unit cells were made large enough to ensure that finite-size effects are negligible.

A.1.3 An Optimised Guide to Measuring Diffusivity

In Chapter 2 and 3, extensive numerical data was used to validate and extend the applicability of new theoretical models. Simulations were specifically designed to measure long-time diffusivity of run-and-tumble motion across a wide range of conditions, requiring both accuracy and computational efficiency. A preliminary analysis using the developed simulation code was conducted to identify the fastest method for obtaining diffusivity estimates with relative errors below one percent. This section focuses on optimising the protocol by which diffusivity is measured.

Different Ways to Measure Diffusivity

The simulation process begins with generating tracks by integrating numerically the equations of motion (see Sec. A.1.1 or Sec. A.1.2). The next step involves measuring the diffusion coefficient from the numerical trajectories. This measurement can be performed in different ways, each potentially leading to different relative errors depending on the simulation parameters: the total simulation time $T_{\rm tot}$ and the integration time-step $\Delta t_{\rm sim}$. Consequently, the initial focus of this analysis is to define different methods for measuring diffusivity, test them through simulations, and conduct error analysis to determine the optimal approach. Although these are not the only ways, the present analysis focuses on the two most commonly used ways to measure diffusivity, one that goes through the mean-squared and the other *via* the directional correlation function. Let's start by defining the two methods.

***Via* the Mean-squared Displacement** The primary method follows the definitions of Sec. 1.2.3. It starts by measuring the mean-squared displacement from the simulated trajectories, and then extracts the diffusivity from a linear fit on the diffusive region of the curve. Specifically, the fitting function is

$$M(t) = 2dD_{\rm f}t^{\nu}\,, \tag{A.1}$$

where d is the space dimension, $D_{\rm f}$ the fitted diffusivity and ν a second fitting parameter that needs to be close to unity to ensure that the fit is performed in the diffusive regime.

Additionally, a consideration regarding the definition of mean-squared displacement (See Eq. 1.5) can be made to improve efficiency of the numerical approach. For a stationary system, transport properties are independent of initial conditions. Consequently, the average of $M(t)$ can be performed not only over the ensemble of independent realisations of the system, but also over all possible time delays within the simulation time. This is equivalent to averaging over all initial times t_0, giving:

$$M(t) = \left\langle \frac{1}{T_{\rm sim}-t}\int_0^{T_{\rm sim}-t}[\mathbf{r}(t'+t)-\mathbf{r}(t')]^2dt' \right\rangle_{N_{\rm sim}}\,, \tag{A.2}$$

where $\mathbf{r}(t)$ is the position at time t, t' is the time delay, $T_{\rm sim}$ is the total observation time and the ensemble average is over $N_{\rm sim}$ realization of the system. This re-formulation

of the $M(t)$ significantly increases sampling, especially at intermediate time intervals, which are the regions of interest for diffusivity measures. Indeed, according to the original definition of Eq. 1.5, the statistical fluctuations while measuring the mean-squared displacement measures would scale as $1/\sqrt{N_{\text{sim}}}$. Following instead Eq. A.2, errors scale instead as $1/\sqrt{N_{\text{sim}}(T_{\text{sim}} - t)}$. Within this second approach, fluctuations scale with time, reaching larger deviations as t approaches T_{sim}. Since diffusivity measures are on long-time quantities, to ensure the long-time deviations do not influence results, the slope of $M(t)$ curve is always fitted on intermediate intervals in which sampling is highest. These intervals are chosen between the onset of the diffusive regime up to a maximum of $T_{\text{sim}}/3$.

***Via* the Directional Correlation Function** The directional correlation function is defined as:

$$\mathrm{C(t)} = \langle \mathbf{e}(t) \cdot \mathbf{e}(t') \rangle \,, \tag{A.3}$$

where $\mathbf{e}(t)$ denotes the orientation of the particle at time t. Using the Taylor-Kubo formula [82], we can rewrite the definition of mean-squared displacement (See Eq. 1.5) in terms of the velocity correlation function[1], as follows:

$$\mathrm{M(t)} = 2\int_0^t \mathrm{d}t' \int_0^{t'} \mathrm{d}t'' \langle \mathbf{v}(t') \cdot \mathbf{v}(t'') \rangle = 2v_0^2 \int_0^t \mathrm{d}t' \int_0^{t'} \mathrm{d}t'' \langle \mathbf{e}(t') \cdot \mathbf{e}(t'') \rangle \,, \tag{A.4}$$

where $\mathbf{v}(t)$ is the velocity vector and the second equality is valid for a particle that moves with constant velocity modulus v_0. By subsequent insertion of Eq. (A.4) in the definition of diffusivity (See Eq. (1.7)), the diffusion coefficient can be re-written in terms of the directional correlation function:

$$\mathrm{D} = \frac{v_0^2}{d} \int_0^\infty \mathrm{d}t \, \mathrm{C(t)} \,. \tag{A.5}$$

The directional correlation function is easily measured from simulated trajectories, and offers an alternative for determining diffusivity. It involves integrating a numerical quantity rather than fitting a long-time limit, thus allowing for diffusivity measurements from short times behaviour, due to the correlation function generally decaying to zero rapidly.

Computationally Efficient Measurements, with Errors Below 1%

As a case study, consider bulk motion with parameters $v_{\text{o}} = 1$, $\tau = 1$ and $D_{\text{r}} = 1$ (in arbitrary simulation units). The aim is to asses the most computationally efficient choice of the simulation time-step, while ensuring relative errors[2] below 1% for the estimates of diffusivity. This analysis involves reproducing bulk motion, where exact diffusivity solutions are known (see Eq. 1.8), and these findings are considered good approximations for measurements in confined settings.

[1] This relation is simply obtained by integration of $\mathrm{d}\mathbf{r}(t) = \mathbf{v}(t)\mathrm{d}t$ and by using the symmetry of the velocity correlation function to permutations of the times t' and t".

[2] Errors are measured by comparison with the exact solution for bulk motion (See Eq. 1.8).

Assessing Errors and Efficiency To focus solely on the impact of Δt_{sim}, let's begin by assuming an excessively large total sampling time[3], ensuring that any errors in the measurements primarily arise from the choice of time-step. Figure A.1a shows the relative errors obtained using the two methods previously discussed for measuring diffusivity. The data clearly indicate that a 1% error can be achieved with $\Delta t_{\text{sim}} \sim 0.1\tau$ when calculating D from $M(t)$, whereas a smaller time-step of $\Delta t_{\text{sim}} \sim 0.01\tau$ is required when measuring D from $C(t)$[4]. This order-of-magnitude difference becomes particularly significant when considering simulation times, as shown in Fig. A.1b. Given that computation times are inversely proportional to the chosen simulation time-step, the mean-squared displacement method is the most efficient choice for measuring diffusivity with regards to the choice of Δt.

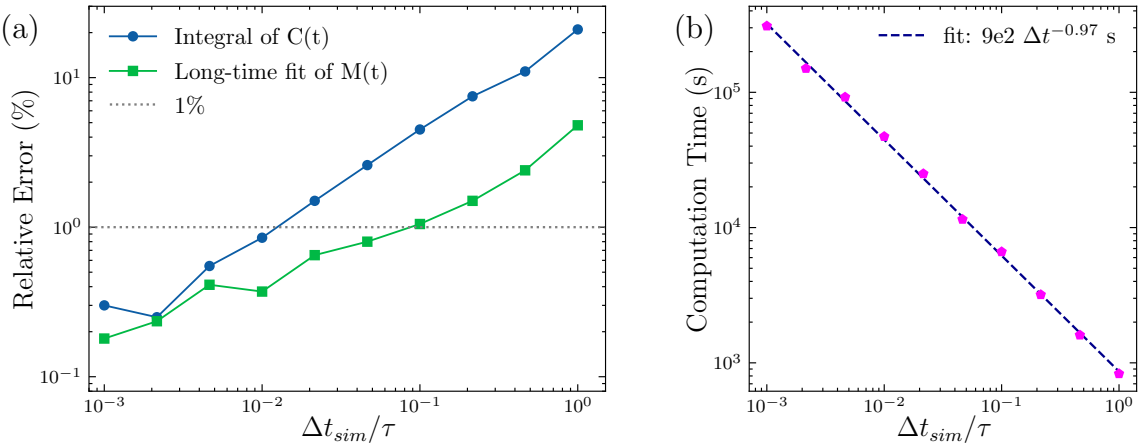

Figure A.1: **Influence of simulation time-step on errors and efficiency.** (a) Relative error on diffusivity estimates as a function of the ratio between simulation time-step and mean run time. Results compare two methods of measuring diffusion coefficients. (b) Average computation times, in seconds, as a function of simulation time-step, with linear fit. Results are obtained by sampling a total of 10^7 mean-run times.

Assessing the Necessary Statistics Another important aspect to consider is determining the total sampling time (T_{tot}) required to ensure that the statistical fluctuations in diffusivity measurements remain below the 1% threshold. Based on previous results, a fixed simulation time-step of $\Delta t = 0.01\tau$ is used. To estimate statistical errors, various values of T_{tot} are selected. For each value, 40 independent simulations with identical parameters are conducted. The normalized standard deviation is then calculated from the 40 independent diffusivity measurements under the same conditions[5]. Results are shown in Fig.A.2a: the diffusivity measured via the correlation function (blue) exhibits fewer

[3]The value used was $T_{\text{tot}} = 10^7\tau$, meaning that each diffusivity estimate is derived from simulated trajectories that include, on average, ten million tumbling events.

[4]This difference can be attributed to the fact that short-time effects, from which the $C(t)$ measure is derived, may be more sensitive to the simulation time-step, while long-time transport, from which $M(t)$ is calculated, may be less affected by larger time-steps.

[5]Mathematically, the normalized standard deviation is expressed as $\sqrt{\langle (D - \langle D \rangle)^2 \rangle}/\langle D \rangle$, where $\langle .. \rangle$ represents the average over 40 independent measurements of the same system.

fluctuations compared to the mean-squared displacement approach (green), reaching the 1% threshold at a nearly an order of magnitude smaller T_{tot}[6]. However, if the fitting method is performed with only one fitting parameter (orange), the fluctuations can be significantly reduced. Specifically, by fixing $\nu = 1$ in Eq. A.1 and allowing diffusivity to be the sole fitting parameter, the fluctuations in the results decrease by a factor of 4. As expected, computation times are directly proportional to the total simulation time (See Fig. A.2b). Therefore, these results suggest that the short-time integral method generally converges faster than the $M(t)$ fitting approach, even though using a one-parameter fit can significantly improve the accuracy of the $M(t)$ results.

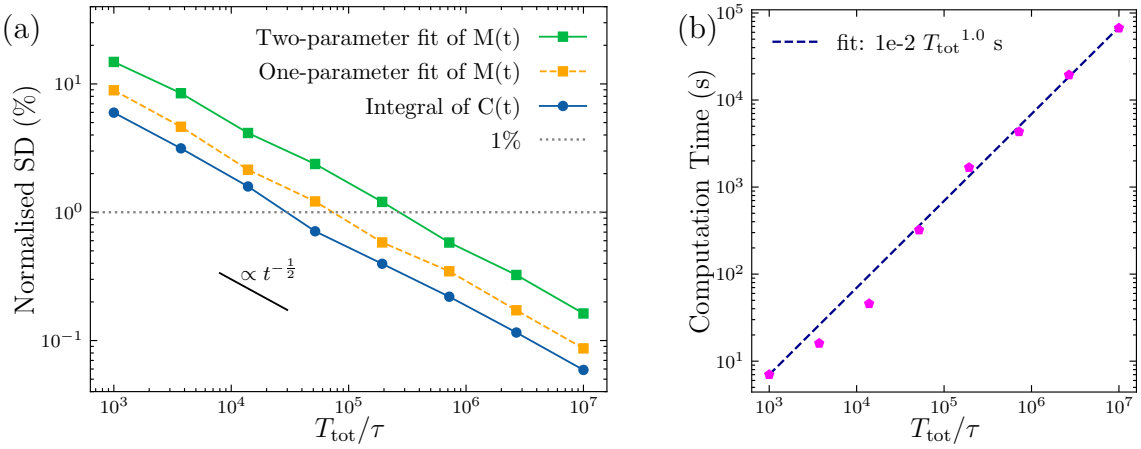

Figure A.2: **Influence of total simulation time on errors and efficiency.** (a) Normalised standard deviation of diffusivity measures as a function of the ratio between total sampling time over mean run time. Results compare different methods of measuring diffusion coefficients. In each scenario, fluctuations follow the expected $1/\sqrt{t}$ dependency. (b) Average computation times, in seconds, as a function of total simulation times. Results are obtained using a simulation time-step that is 1% the mean-run time.

Optimal Method for Measuring Diffusivity

Based on the previous analysis, the method used to measure diffusivity across all results shown in Chapter 2 and Chapter 3 is explained. Diffusivity is measured through a one-parameter linear fit, in log-log scale[7], within the linear interval of the $M(t)$, selected in the range $[100\tau, 500\tau]$. To ensure the linearity of this fit, first a two-parameter fit is performed to verify that ν is close to unity. For all numerical data presented in Chapter 2,the fit exponent ν is consistently close to one, with deviations around 1.7%, as shown from the histogram of Fig. A.3. The numerical parameters used in this analysis are $\Delta t_{\text{sim}}/\tau = 10^{-2}$ and $T_{\text{tot}}/\tau = 10^6$. This selection comfortably meets the required accuracy and each

[6]This is likely due to statistical fluctuations diminishing rapidly at short times, where the $C(t)$ measurement is taken, whereas the intermediate-time MSD fitted region requires more extensive sampling to achieve convergence.

[7]To perform linear regression on the log-log data of the mean-squared displacement as a function of time, Eq. A.1 is rewritten as $\log M(t) = \log(2dD) + \nu \log t$.

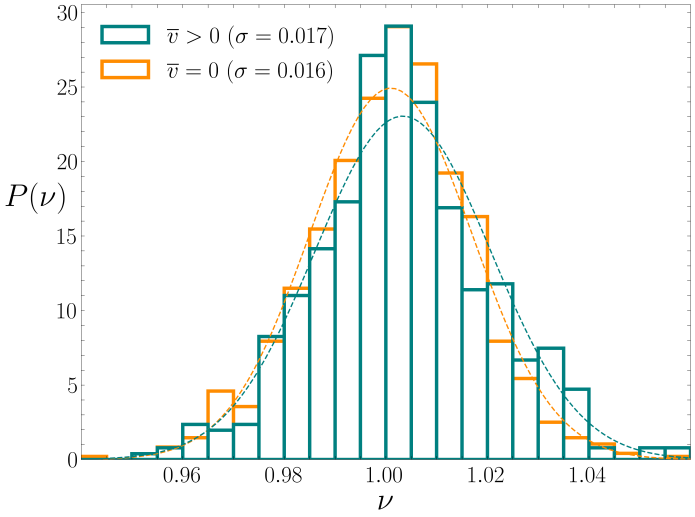

Figure A.3: **Fit exponent for all simulation data in Chapter 2** Histogram of the fitted linearity coefficients for the 2000 diffusivity estimates presented in Chapter 2. The coefficient follows a normal distribution centered around one, with a fitted standard deviation of approximately $1 - 2\%$. Results are consistent across cases with and without surface motion ($\bar{v_o} > 0$ and $\bar{v_o} = 0$, respectively).

numerical estimate is completed within approximately one hour of computation time[8].

A.2 Additional Analyses of the Four-direction Model

This section contains additional results and analyses linked to the discrete-direction model presented in Chapter 2.

A.2.1 Numerical Check of the Model

The numerical method used in Sec. 2.3 can be adapted to simulate run-and-tumble motion within a slit for the four-direction model. Shown in Fig. A.4 is the diffusion coefficient obtained for a variety of parameter combinations. The relative error between numerical and analytical results does not exceed 1% and is 0.4% on average. A similar agreement holds for other parameter combinations tested.

A.2.2 Effective Escape Rate

The correction factor in the effective escape rate of Eq. (2.23a) might be interpreted from a purely geometric argument. Consider the flux of particle leaving the wall and imposing that it has to remain unchanged when matching the continuous and discrete models. For a unit length of wall occupied with a particle density ρ, the flux of particle crossing a line infinitely close to the wall is $\rho\hat{\mu}\langle v_\perp\rangle$, where the average velocity perpendicular to the wall is given by

$$\frac{\langle v_\perp\rangle}{v_o} = \frac{1}{\pi}\int_{-\pi/2}^{\pi/2}\cos\theta\,\mathrm{d}\theta = \frac{2}{\pi}, \tag{A.6}$$

because in the continuous model, the direction of escape is uniformly distributed. To establish a correspondence from the continuous model to the four-direction model, a

[8]This computation time is based on each simulation running on a single CPU thread. The choice to run in a single thread, rather than multi-threading, simplifies the management of running a large number of simulations in parallel.

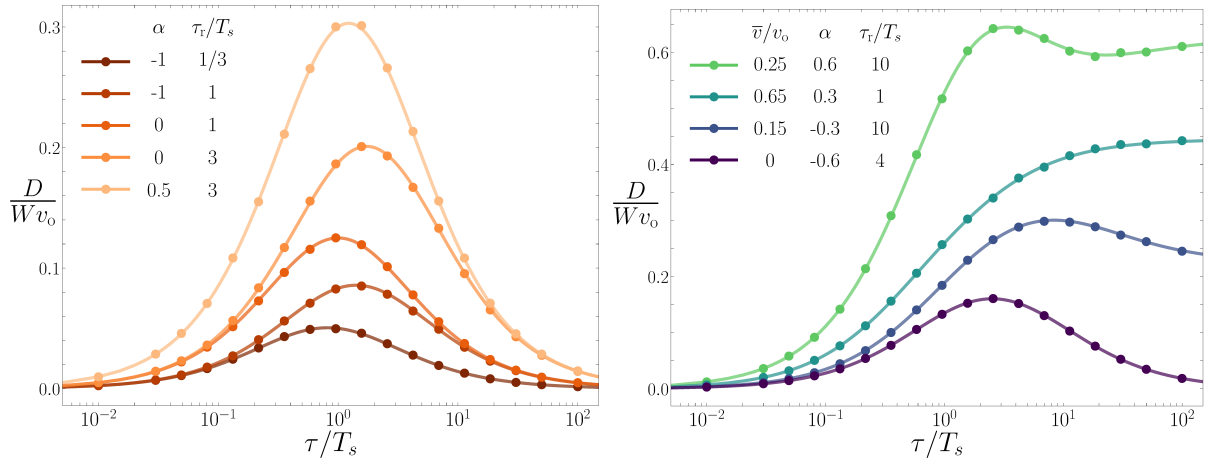

Figure A.4: **Numerical check of diffusivity solutions in the four-direction model.** The diffusion coefficient obtained from numerical simulations (points) is compared to the theoretical expression (lines) given by Eq. (2.27). Surface-motion cases are on the right, and those without are on the left.

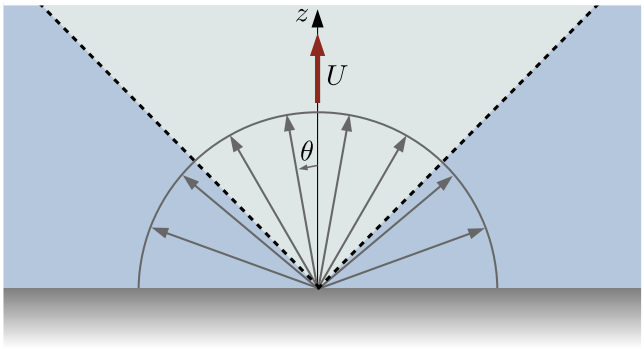

Figure A.5: **Escape rate matching between models.** Matching the escape rate between the continuous and four-direction model. In the former, a particle leaves the wall with a random angle θ which is uniformly distributed. In the latter, a particle escapes perpendicular to the wall.

natural matching procedure is to define angular sectors as in Fig. A.5 and require that only particles with $|\theta| < \pi/4$ are ascribed the up-direction and actually leaving the surface. With those assumptions, we have now

$$\frac{\langle v_\perp \rangle}{v_o} = \frac{2}{\pi} \int_{-\pi/4}^{\pi/4} \cos\theta \, \mathrm{d}\theta = \frac{2\sqrt{2}}{\pi}. \tag{A.7}$$

Compared to Eq. (A.6), the average velocity perpendicular to the wall is increased by a factor of $\sqrt{2}$. Because physically, we ask for a similar flux in the continuous and four-direction models, one needs to lower the rate in the latter, suggesting

$$\mu = \frac{\hat{\mu}}{\sqrt{2}}. \tag{A.8}$$

Such a correction is perfectly consistent with the data.

A.2.3 Approximations for Optimal Mean Run Time

When the particle remains mobile at the wall, some approximations are required to write the optimal mean run time in explicit form. A first case to consider is when the surface

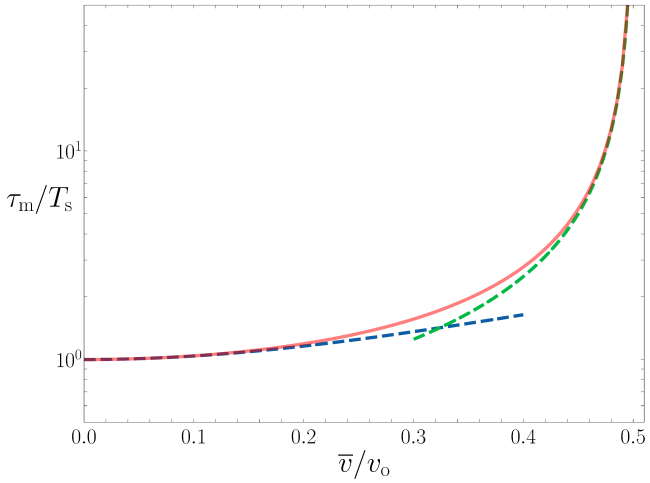

Figure A.6: **Optimal mean run time comparison.** Exact optimal mean run time τ_m computed numerically (continuous line) and approximations (dashed lines) from Eqs. (A.9a) and (A.11). Parameters are $\eta = 2$, $\tau_r = 1$ and $\alpha = 0$, as in Fig. 2.7.

velocity is small. With ϵ denoting a small parameter, one finds a quadratic departure

$$\bar{v} = \epsilon, \qquad \tau_m = \tau_{m,0} + A\epsilon^2, \tag{A.9a}$$

$$A \equiv \frac{\tau_{m,0}(\tau_{m,0} + \alpha'\tau_r)^2\,[\alpha'(\eta\tau_r + 2) + 2\eta\tau_{m,0}]}{2\alpha'(\tau_{m,0} + \tau_r)^2}, \tag{A.9b}$$

where $\tau_{m,0} \equiv \sqrt{2\alpha'\tau_r/\eta}$ and units of Sec. 2.4.1 are used. A second case amenable to exact results is when $2\alpha' - \alpha\eta\tau_r > 0$, a condition that is satisfied in particular for all motion patterns with $\alpha \leqslant 0$ or for strong rotational diffusion. Then, the first scenario applies and τ_m diverges continuously, which allows to obtain the critical velocity

$$\bar{v}_c = \frac{1}{\sqrt{2 + \eta\tau_r}}. \tag{A.10}$$

Close to the critical value $\bar{v}_c$, the divergence of the optimal run time can be characterized as

$$\bar{v} = \bar{v}_c - \epsilon, \qquad \tau_m = \frac{B}{\epsilon}, \quad B \equiv \tau_r \bar{v}_c^3(2\alpha' - \alpha\eta\tau_r). \tag{A.11}$$

As illustrated in Fig. A.6, the approximations of τ_m at low and high surface velocity may give a reasonable estimate in most of the velocity range.

A.3 Additional Notes - Chapter 3

This appendix contains additional calculations and definitions used in Chapter 3.

A.3.1 Appendix: Laplace and Fourier transforms

The definition, inverse and convolution for Laplace transform are given by

$$f(s) = \int_0^\infty \mathrm{d}t\; e^{-st} f(t), \qquad [f * g]\,(t) = \int_0^t \mathrm{d}t'\, f(t - t')g(t'), \tag{A.12a}$$

$$f(t) = \frac{1}{2\pi i}\int_{c-i\infty}^{c+i\infty} \mathrm{d}s\; e^{ts} f(s), \qquad [f * g]\,(s) = f(s)g(s). \tag{A.12b}$$

As regards the Fourier series used for orientation angle θ, we have

$$f(l) = \frac{1}{2\pi}\int_{-\pi}^{\pi} \mathrm{d}\theta\, e^{-il\theta} f(\theta), \qquad [f \otimes g](\theta) = \int_{-\pi}^{\pi} \mathrm{d}\theta'\, f\Big(\text{v.p.}(\theta - \theta')\Big) g(\theta'), \tag{A.13a}$$

$$f(\theta) = \sum_{l=-\infty}^{\infty} f(l)\, e^{il\theta}, \qquad [f \otimes g](l) = 2\pi f(l) g(l), \tag{A.13b}$$

where $\text{v.p.}(\theta) = \arg\left(e^{i\theta}\right)$ with values taken in $[-\pi, \pi[$.

APPENDIX B

Experiments: Material and Methods

B.1 SS-5 Growth Protocol

This appendix details the laboratory methods for cultivating the Magnetotactic Bacteria SS-5 strain. It includes comprehensive protocols and lists of materials required for establishing and maintaining bacterial cultures, as well as preparing all necessary solutions.

B.1.1 Bacterial Culture

The SS-5 strain, having been discovered only ten years ago, the protocol to culture is still an active topic of research. Currently, the only stable protocol for their growth involves semi-solid cultures. The resulting colonies grow with a rather slow duplication rate of roughly one day, so from the time in which cultures are refreshed to the moment where they reach optimal growing condition, roughly a week must pass by.

Culture in the Lab SS-5 grows in a semisolid, enriched oxygen gradient medium, as described by Lefèvre *et al.* [190]. This medium is based on a modified artificial seawater solution, which mimics the typical salt concentrations found in the bacteria's natural environment (a mixture of calcium, potassium, magnesium, and sodium chlorides, along with sodium sulfate; see Sec. B.2.4). The medium is further enriched with minerals, vitamins, iron (to allow for synthesis of magnetosomes), and is reduced in oxygen and solidified with agar. The preparation of the medium follows a specific procedure (see Sec. B.2.3) that establishes a vertical oxygen gradient within the solution, indicated by an oxygen-sensitive pink dye (Resazurin) added to the solution (see Fig.B.1a). Optimal bacterial growth occurs when cells are inoculated in the oxic-anoxic zone (OAZ), identifiable as the interface between the pink and transparent regions of the medium. Within one day, the inoculated bacteria migrate within the solution, forming a flat culture at the OAZ (see Fig.B.1b), which can continue growing for up to four weeks[1]. The culture process

[1] After four weeks, the oxygen gradient gradually dissipates, and bacterial growth diminishes as the nutrients in the solution become depleted.

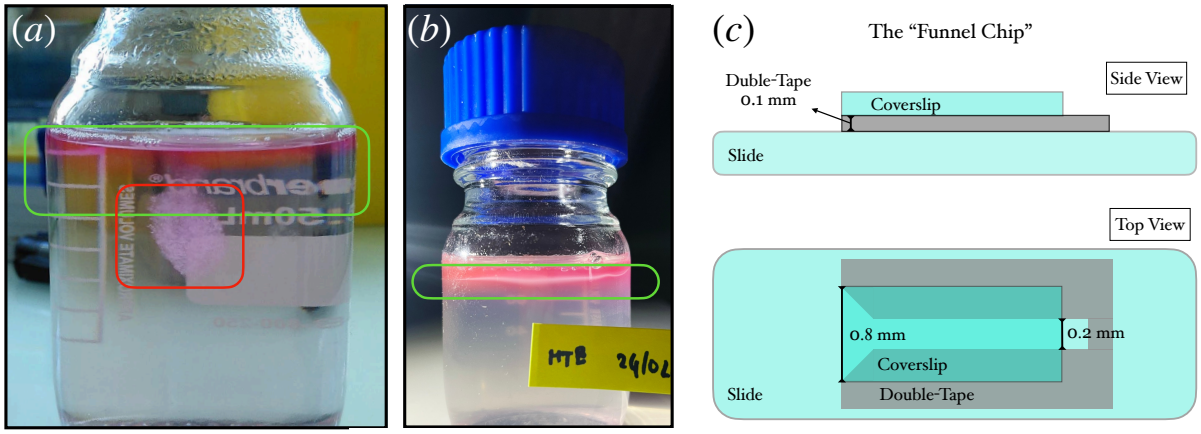

Figure B.1: **Experiments Preparation.** (a)-(b) SS-5 colonies at different stages. (a) at the time of inoculation; the pink Resazurin dye shows oxygen gradient (green), with the bacterial inoculum placed at the end of the pink gradient (red).(b) 7 days after inoculation. A thin grey band (green) represents a dense bacterial colony at the OAZ. (c) Schematics for the "Funnel Chip" used for transfer and observation (not to scale).

is delicate; bacterial growth can be compromised if the cells are displaced from the OAZ interface, which may occur if the culture bottle is tilted or displaced too quickly.

B.2 Methods: Transfer, Observation and Tracking

This section of the Appendix outlines key procedures required for the experimental results. It details the steps necessary to go from bacterial cultures to proper samples suitable for observation and recording. Additionally, it explains how tracks are extracted from image sequences, which are then used for the results discussed in Chapter 4.

B.2.1 Transfer from Agar to a Swimming Medium

To observe bacteria under the microscope, samples are typically collected from colonies 5-10 days after being refreshed. The first step involves transferring bacteria from the agar-rich, semi-solid growth medium to an agar-free liquid. This is crucial since the study in this thesis aims to characterize bacterial motion within bulk fluid, and not within complex semi-solid media. For MTB, the transfer to a liquid phase can be done by taking advantage of their magnetic response. A common method is to place a drop of agar containing bacteria onto a hydrophobic surface, like parafilm, and then position a liquid drop next to it. A magnet is used to move the bacteria from the agar to the liquid. While this approach is quick and effective, it has several limitations: it does not allow for the collection of large quantities of bacteria, offers limited control over the process, and often leads to agar contamination in the liquid, reducing observation quality. To address these issues, a simple chip was developed to perform our experiments.

The Funnel Chip The method used allows for the extraction of bacteria from agar and their observation within the same device. The device itself is simple, shown in Fig. B.1c.

It consists of a 100 µm-thick double-sided tape placed between a slide and a coverslip, enabling observation through the cut region. The tape is cut using a plotter to form a funnel-shaped opening followed by a long, wide channel. To load bacteria into the chip, the channel is first filled from the open end with the liquid phase[2]. An agar drop taken directly from the bacterial colony is then placed on the funnel side. Bacteria are extracted using magnetic fields generated by the coils (see Sec. 4.2.1), and the transfer process can be observed under a microscope.

The channel structure effectively prevents agar from entering the liquid during the experiment, as the bacteria rapidly reach the end of the channel thanks to directed motion, while agar diffusion takes much longer to reach the inner part of the channel. All data in Chapter 4 were obtained using these configurations. It is worth mentioning that this extraction method necessarily selecting only motile bacteria, biasing measurements to the swimming population. It is also a "magnetic sorting", selecting for a specific response to magnetic fields.

B.2.2 Recording and Tracking

Recording After the bacteria are transferred into the liquid phase, recordings of their motion are made under different applied fields. These recordings are taken at approximately 50 µm from the glass layer, roughly at the middle height of the channel. This positioning is intended to observe motion away from the solid glass boundary, which could influence swimming dynamics. The recordings are captured at 10× magnification, at 51 frames per second, typically for a total recording time of 1 minute for each measurement. To ensure minimal changes in the bacterial populations throughout the experiments, magnetic fields are frequently inverted between measurements. This allows bacteria from the same population to cross the field of view multiple times and be observed across different measurements.

Tracking The bacterial tracks are reconstructed from experimental images using the Python library `Trackpy`, which implements the Crocker-Grier algorithm. The reconstruction process consists of two main steps: first, identifying objects to track in each image, and second, linking the detected positions from one image to the next. The first step uses a simple peak detection algorithm, while the second determines the most probable set of displacements. Although the tracking algorithm is straightforward, it comes with typical limitations of trajectory reconstruction, such mismatched trajectories and the inability to follow particles over reasonably long times. However, these issues were not significant in the presented data. The results focus on dilute bacterial suspensions, where particle crossings are rare and negligible. Moreover, most recordings made under applied fields show that bacteria remain in the focal plane for extended periods, enabling long-term tracking.
Two post-tracking filters are applied to prevent tracking artifacts. First, tracks shorter than 150 milliseconds are removed. Then, a second filter eliminates particles with excessively slow mean velocities (lower than 5 µm s^{-1}), likely corresponding to diffusive motion of either dead cells or agar droplets.

[2]The agar-free liquid phase used as the swimming medium is obtained by centrifuging the growth medium at 13,000 rpm for 10 min, followed by extraction of the supernatant.

B.2.3 Preparation of SS-5 Agar/Agarose Medium

Protocol The required chemicals are listed in Table B.5. Recipes and protocols for solutions No. (1), (3), (7), (8), (9) are reported in Sec. B.2.4. To prepare the SS-5 Agar/Agarose medium, proceed as follows:

Step	Procedure
1	Prepare sterile tubes and gather all required chemicals as listed in Table B.5, and equipment including beakers, a magnetic bar, a spatula, and cuvettes for weighing.
2	Into a beaker, add solutions No. (1), (2), and (3).
3	Weigh components No. (4), (5), and (6). Accurately transfer them into the beaker using ultra-pure water to rinse the cuvettes.
4	Ensure thorough mixing with a magnetic stirrer. Check and adjust the pH to 6.2 using 1% HCl.
5	Pour the prepared medium into a graduated cylinder and adjust the volume with ultra-pure water until the desired V_f is reached.
6	Autoclave the medium.
7	Work under sterile conditions. Once the solution has cooled down to approximately 40 degrees Celsius, add solutions No. (7), (8), (9), and (10).
8	Weigh 0.4 g of material No. (11) and dissolve into 10 mL of filtered water, then add the volume indicated in the table to the medium solution. Note that this solution should not be prepared in advance but rather prepared and added to the medium at the time of preparation.
9	Check and adjust the pH to 7 using 1% HCl. Since the main solution is sterile, this procedure must be done by subsequent extractions of aliquots from the medium, not by direct measurement.
10	Once pH is regulated, distribute the medium solution into smaller sterile containers, depending on the use.
11	After approximately one hour, a gradient should become visible within the bottle thanks to the Resazurin dye. The gradient allows for identification of the OAZ and indicates the samples are ready for inoculation.

B.2.4 Additional Solutions and Protocols

Artificial Sea Water (ASW) 3X Concentrated Follow these steps to prepare the 3X concentrated ASW solution:

Step	Procedure
1	Weigh the different components in Table B.6.
2	Initially, add approximately 500 mL of ultra-pure water to the beaker to facilitate the solubilization of the components.
3	Add all powders to the beaker, in order from No. (1) to (5), washing the cuvettes with ultra-pure water to transfer all residues into the beaker.
4	Place a magnetic stirrer in the beaker and allow the solubilization to occur, for at least 15 minutes.

5	Transfer the solubilized solution into the graduated cylinder and make up the volume to the desired final volume, adding ultra-pure water.
6	Pass the solution through a 0.22 µm filtration unit and store in the fridge 4°C.

Wolfe's Mineral Solution Chemicals and quantities are listed in Table B.7. The procedure to make Wolfe's Mineral solution is listed below.

Step	Procedure
1	Add No. (1) to 500 mL of distilled water in a volumetric flask.
2	Adjust the pH to 6.5 using saturated KOH while stirring constantly. (1.45 g/ml is the saturation concentration of KOH in water)
3	The NTA will dissolve as the pH increases. Once the NTA is completely dissolved and the pH is at 6.5, add each mineral salt in the order given No. (2) through No. (13), allowing each to dissolve fully before adding the next.
4	After all the ingredients are dissolved, bring the total volume up to 1 L with distilled water.
5	Autoclave the solution to sterilize it. Store the solution at 4°C.

Wolfe's Vitamins Chemicals and quantities are listed in Table B.8. The procedure to make Wolfe's Vitamins solution is listed below.

Step	Procedure
1	Add No. (1) and No. (2) to approximately 50 mL of distilled deionized water in a volumetric flask.
2	Add the remaining stock vitamins No. (3) through No. (9) to the solution.
3	Bring the total volume up to 100 mL using distilled deionized water in the volumetric flask.
4	Note: The No. (8) stock will need to be warmed to about 50°C to dissolve properly.
5	Note: The No. (9) stock is more like a suspension than a solution. Ensure it is well-mixed before taking an aliquot out. It will dissolve in the final solution.
6	For preparing an anaerobic stock solution of vitamins: Prepare sterile (autoclaved) serum bottles filled with O_2-free N_2 and crimp-sealed.
7	Inject the vitamin solution into the serum bottles using a syringe and a sterile needle through a 0.22 µm filter directly through the stopper.
8	Ensure that a sterile outlet needle is placed through the stopper to prevent excess pressure buildup. Bending the needle sideways will help prevent aerosol contaminants from entering the bottle.
9	Inject 50 mL of the vitamin solution per bottle, remove the needles, and allow the solution to equilibrate for about 30 minutes.
10	Purge the headspace of the bottle with O_2-free N_2 for 30 minutes and leave a positive pressure of at least 8 lbs/in^2.
11	Store the anaerobic stock solution at 4°C.

PO_4 Buffer (0.5M, pH7) The buffer is prepared using dipotassium phosphate (K_2HPO_4) and monopotassium phosphate (KH_2PO_4). Dissolve 17.4 g of dibasic into 200 mL of ultra-pure water, and 6.8 g of monobasic into 100 mL of ultra-pure water. Add the dibasic solution into a flask and then add the monobasic until pH7 is reached. Store in the fridge at 4°C.

$FeSO_4$ solution (0.01mM) Dissolve 0.675 g of $FeSO_4 \cdot 7H_2O$ in 250 mL of ultrapure water. Transfer the solution to a flask with a septum cap and autoclave it. After autoclaving, flush the vial with N_2 through the septum. Ensure that the incoming needle passes first through a filter before entering the solution, and insert a secondary sterile needle into the septum as an outlet to prevent pressure buildup during the flushing process.

Table B.5: Components and quantities for SS-5 Agar/Agarose growth medium. Quantities are reported for three final volumes V_f.

No.	Component	V_f =1000 mL	V_f =500 mL	V_f =250 mL
1	ASW solution	333.2 mL	166.6 mL	83.3 mL
2	Resazurin	200 µL	100 µL	50 µL
3	Wolfe's Mineral solution	5 mL	2.5 mL	1.25 mL
4	NH_4Cl	0.3 g	0.15 g	0.075 g
5	$NaHCO_3$	1.26 g	0.63 g	0.315 g
6	Agar/Agarose	1.2 g	0.6 g	0.3 g
7	Wolfe's Vitamins	500 µL	250 µL	125 µL
8	PO_4 buffer (0.5 M, pH7)	1.8 mL	0.9 mL	0.45 mL
9	$FeSO_4$ (0.01mM)	3 mL	1.5 mL	0.75 mL
10	Thiosulphate (40%)	3 mL	1.5 mL	0.75 mL
11	L-Cysteine (pH7)	7.5 mL	5 mL	2.5 mL

Table B.6: Components and quantities for Artificial Sea Water (ASW) 3X Concentrated. Quantities are reported for final volumes V_f of 1L and 3L.

No.	Component	V_f =1L	V_f =3L
1	NaCl	113.4 g	340.2 g
2	$MgCl_2$ ($6H_2O$)	16.2 g	48.6 g
3	Na_2SO_4 ($2H_2O$)	16.2 g	48.6 g
4	KCl	2.7 g	8.1 g
5	$CaCl_2$	1.5 g	4.5 g

Table B.7: Ingredients and quantities for the Wolfe's Mineral solution (V_f =1L).

No.	**Ingredient**	**Amount**
1	Nitrilotriacetic acid (NTA)	1.5 g
2	$MgCl_2 \cdot 7H_2O$	3.0 g
3	$MnSO_4 \cdot H_2O$	0.5 g
4	NaCl	1.0 g
5	$FeSO_4 \cdot 7H_2O$	0.1 g
6	$CoCl_2 \cdot 6H_2O$ or $CoSO_4 \cdot 7H_2O$	0.1 g
7	$CaCl_2 \cdot 2H_2O$	0.1 g
8	$ZnSO_4 \cdot 7H_2O$	0.1 g
9	$CuSO_4 \cdot 5H_2O$	0.025 g
10	$AlK(SO_4)_2 \cdot 12H_2O$	0.01 g
11	H_3BO_3	0.01 g
12	$Na_2MoO_4 \cdot 2H_2O$	0.4 g
13	$NiCl_2 \cdot 6H_2O$	0.01 g

Table B.8: Components and quantities for the Wolfe's Vitamin mixture (V_f = 100mL).

No.	**Component**	**Amount**
1	Thiamin	90 mg
2	Inositol	40 mg
3	D-, L-Ca^{2+} pantothenate	4 mL
4	Para amino benzoic acid (PABA)	2.5 mL
5	Vitamin B	5 mL
6	Pyridoxine (Vitamin B_6)	4 mL
7	Niacin (Nicotinic acid)	4 mL
8	Biotin*	1 mL
9	Folic acid**	0.4 mL

Bibliography

[1] Y. M. Bar-On, R. Phillips, and R. Milo, "The biomass distribution on Earth," *Proceedings of the National Academy of Sciences of the United States of America*, vol. 115, no. 25, 2018.

[2] K. F. Jarrell and M. J. McBride, "The surprisingly diverse ways that prokaryotes move," *Nature Reviews Microbiology*, vol. 6, no. 6, 2008.

[3] X. Raynaud and N. Nunan, "Spatial ecology of bacteria at the microscale in soil," *PLoS ONE*, vol. 9, no. 1, 2014.

[4] T. Krüger and M. Engstler, "Motility Analysis of Trypanosomatids," *Methods in Molecular Biology*, vol. 2116, 2020.

[5] M. Luo, Y. Feng, T. Wang, and J. Guan, "Micro-/Nanorobots at Work in Active Drug Delivery," *Advanced Functional Materials*, vol. 28, no. 25, 2018.

[6] J. Elgeti, R. G. Winkler, and G. Gompper, "Physics of microswimmers - Single particle motion and collective behavior: A review," *Reports on Progress in Physics*, vol. 78, no. 5, 2015.

[7] C. Bechinger, R. Di Leonardo, H. Löwen, C. Reichhardt, G. Volpe, and G. Volpe, "Active particles in complex and crowded environments," *Reviews of Modern Physics*, vol. 88, no. 4, 2016.

[8] D. Selmeczi, L. Li, L. I. Pedersen, S. F. Nrrelykke, P. H. Hagedorn, S. Mosler, N. B. Larsen, E. C. Cox, and H. Flyvbjerg, "Cell motility as random motion: A review," *European Physical Journal: Special Topics*, vol. 157, no. 1, 2008.

[9] R. Hayat, S. Ali, U. Amara, R. Khalid, and I. Ahmed, "Soil beneficial bacteria and their role in plant growth promotion: A review," *Annals of Microbiology*, vol. 60, no. 4, 2010.

[10] C. Escudero, M. Vera, M. Oggerin, and R. Amils, "Active microbial biofilms in deep poor porous continental subsurface rocks," *Scientific Reports*, vol. 8, no. 1, 2018.

[11] G. Junot, T. Darnige, A. Lindner, V. A. Martinez, J. Arlt, A. Dawson, W. C. Poon, H. Auradou, and E. Clément, "Run-to-Tumble Variability Controls the Surface Residence Times of E. coli Bacteria," *Physical Review Letters*, vol. 128, no. 24, 2022.

[12] T. Bhattacharjee and S. S. Datta, "Bacterial hopping and trapping in porous media," *Nature Communications*, vol. 10, no. 1, 2019.

[13] M. Dentz, A. Creppy, C. Douarche, E. Clément, and H. Auradou, "Dispersion of motile bacteria in a porous medium," *Journal of Fluid Mechanics*, vol. 946, 2022.

[14] L. Angelani, "Run-and-tumble motion in trapping environments," *Physica Scripta*, vol. 12, no. 1, 2023.

[15] F. Q. Potiguar, G. A. Farias, and W. P. Ferreira, "Self-propelled particle transport in regular arrays of rigid asymmetric obstacles," *Physical Review E - Statistical, Nonlinear, and Soft Matter Physics*, vol. 90, no. 1, 2014.

[16] M. Brun-Cosme-Bruny, E. Bertin, B. Coasne, P. Peyla, and S. Rafaï, "Effective diffusivity of microswimmers in a crowded environment," *Journal of Chemical Physics*, vol. 150, no. 10, 2019.

[17] A. Dhar, A. Kundu, S. N. Majumdar, S. Sabhapandit, and G. Schehr, "Run-and-tumble particle in one-dimensional confining potentials: Steady-state, relaxation, and first-passage properties," *Physical Review E*, vol. 99, no. 3, 2019.

[18] J. Elgeti and G. Gompper, "Run-and-tumble dynamics of self-propelled particles in confinement," *EPL*, vol. 109, no. 5, 2015.

[19] C. G. Wagner, M. F. Hagan, and A. Baskaran, "Steady-state distributions of ideal active Brownian particles under confinement and forcing," *Journal of Statistical Mechanics: Theory and Experiment*, vol. 2017, no. 4, 2017.

[20] N. A. Licata, B. Mohari, C. Fuqua, and S. Setayeshgar, "Diffusion of Bacterial Cells in Porous Media," *Biophysical Journal*, vol. 110, no. 1, 2016.

[21] C. Kurzthaler, S. Mandal, T. Bhattacharjee, H. Löwen, S. S. Datta, and H. A. Stone, "A geometric criterion for the optimal spreading of active polymers in porous media," *Nature Communications*, vol. 12, no. 1, 2021.

[22] T. Bertrand, Y. Zhao, O. Bénichou, J. Tailleur, and R. Voituriez, "Optimized Diffusion of Run-and-Tumble Particles in Crowded Environments," *Physical Review Letters*, vol. 120, no. 19, 2018.

[23] Z. Cai, Q. Fu, S. Zhang, C. Fan, X. Zhang, J. Guo, and S. Guo, "Performance evaluation of a magnetically driven microrobot for targeted drug delivery," *Micromachines*, vol. 12, no. 10, 2021.

[24] C. T. Lefèvre, M. Bennet, L. Landau, P. Vach, D. Pignol, D. A. Bazylinski, R. B. Frankel, S. Klumpp, and D. Faivre, "Diversity of magneto-aerotactic behaviors and oxygen sensing mechanisms in cultured magnetotactic bacteria," *Biophysical Journal*, vol. 107, no. 2, 2014.

[25] G. Vargas, J. Cypriano, T. Correa, P. Leão, D. A. Bazylinski, and F. Abreu, "Applications of magnetotactic bacteria, magnetosomes and magnetosome crystals in biotechnology and nanotechnology: mini-review," *Molecules*, vol. 23, no. 10, 2018.

[26] S. Wadmare, "A Review on Magnetotactic Bacteria and Magnetosomes: Recent Trends and Multivalent Advances," *Frontiers in Environmental Microbiology*, vol. 7, no. 4, 2021.

[27] M. Marmol, E. Gachon, and D. Faivre, "Colloquium: Magnetotactic bacteria: From flagellar motor to collective effects," *Rev. Mod. Phys.*, vol. 96, p. 021001, Apr 2024.

[28] J. Kallmeyer, R. Pockalny, R. R. Adhikari, D. C. Smith, and S. D'Hondt, "Global distribution of microbial abundance and biomass in subseafloor sediment," *Proceedings of the National Academy of Sciences of the United States of America*, vol. 109, no. 40, 2012.

[29] S. Liang, H. Li, H. Wu, B. Yan, and A. Song, "Microorganisms in coastal wetland sediments: a review on microbial community structure, functional gene, and environmental potential," *Frontiers in Microbiology*, vol. 14, no. 1, 2023.

[30] F. Reith, M. F. Lengke, D. Falconer, D. Craw, and G. Southam, "The geomicrobiology of gold," *ISME Journal*, vol. 1, no. 7, 2007.

[31] F. W. Collins, C. J. Walsh, B. Gomez-Sala, E. Guijarro-García, D. Stokes, K. B. Jakobsdóttir, K. Kristjánsson, F. Burns, P. D. Cotter, M. C. Rea, C. Hill, and R. P. Ross, "The microbiome of deep-sea fish reveals new microbial species and a sparsity of antibiotic resistance genes," *Gut Microbes*, vol. 13, no. 1, 2021.

[32] J. A. Coker, "Recent advances in understanding extremophiles.," *F1000Research*, vol. 8, no. 1, 2019.

[33] M. Baym, T. D. Lieberman, E. D. Kelsic, R. Chait, R. Gross, I. Yelin, and R. Kishony, "Spatiotemporal microbial evolution on antibiotic landscapes," *Science*, vol. 353, no. 6304, 2016.

[34] N. Merino, H. S. Aronson, D. P. Bojanova, J. Feyhl-Buska, M. L. Wong, S. Zhang, and D. Giovannelli, "Living at the extremes: Extremophiles and the limits of life in a planetary context," *Frontiers in Microbiology*, vol. 10, no. MAR, 2019.

[35] J. P. De Vera, U. Boettger, R. D. L. T. Noetzel, F. J. Sánchez, D. Grunow, N. Schmitz, C. Lange, H. W. Hübers, D. Billi, M. Baqué, P. Rettberg, E. Rabbow, G. Reitz, T. Berger, R. Möller, M. Bohmeier, G. Horneck, F. Westall, J. Jänchen, J. Fritz, C. Meyer, S. Onofri, L. Selbmann, L. Zucconi, N. Kozyrovska, T. Leya, B. Foing, R. Demets, C. S. Cockell, C. Bryce, D. Wagner, P. Serrano, H. G. Edwards, J. Joshi, B. Huwe, P. Ehrenfreund, A. Elsaesser, S. Ott, J. Meessen, N. Feyh, U. Szewzyk, R. Jaumann, and T. Spohn, "Supporting Mars exploration: BIOMEX in Low Earth Orbit and further astrobiological studies on the Moon using Raman and PanCam technology," *Planetary and Space Science*, vol. 74, no. 1, 2012.

[36] S. Moens and J. Vanderleyden, "Functions of bacterial flagella," *Critical Reviews in Microbiology*, vol. 22, no. 2, 1996.

[37] O. A. Soutourina, E. A. Semenova, V. V. Parfenova, A. Danchin, and P. Bertin, "Control of Bacterial Motility by Environmental Factors in Polarly Flagellated and Peritrichous Bacteria Isolated from Lake Baikal," *Applied and Environmental Microbiology*, vol. 67, no. 9, 2001.

[38] H. C. Berg and D. A. Brown, "Chemotaxis in Escherichia coli analysed by three-dimensional tracking," *Nature*, vol. 239, no. 5374, 1972.

[39] E. M. Purcell, "Life at low Reynolds number," *American Journal of Physics*, vol. 45, no. 1, 1977.

[40] H. C. Berg and F. Dyson, " Random Walks in Biology ," *Physics Today*, vol. 40, no. 3, 1987.

[41] M. C. Marchetti, J. F. Joanny, S. Ramaswamy, T. B. Liverpool, J. Prost, M. Rao, and R. A. Simha, "Hydrodynamics of soft active matter," *Reviews of Modern Physics*, vol. 85, no. 3, 2013.

[42] M. E. Cates and J. Tailleur, "Motility-induced phase separation," *Annual Review of Condensed Matter Physics*, vol. 6, no. 1, 2015.

[43] N. Ruiz and T. J. Silhavy, "How Escherichia coli Became the Flagship Bacterium of Molecular Biology," *Journal of Bacteriology*, vol. 204, no. 9, 2022.

[44] D. A. Brown and H. C. Berg, "Temporal stimulation of chemotaxis in Escherichia coli," *Proceedings of the National Academy of Sciences of the United States of America*, vol. 71, no. 4, 1974.

[45] K. M. Taute, S. Gude, S. J. Tans, and T. S. Shimizu, "High-throughput 3D tracking of bacteria on a standard phase contrast microscope," *Nature Communications*, vol. 6, 2015.

[46] H. E. Kubitschek, "Cell volume increase in Escherichia coli after shifts to richer media," *Journal of Bacteriology*, vol. 172, no. 1, 1990.

[47] R. Xue, Q. Ma, M. A. Baker, and F. Bai, "A Delicate Nanoscale Motor Made by Nature—The Bacterial Flagellar Motor," *Advanced Science*, vol. 2, no. 9, 2015.

[48] R. M. Berry and J. P. Armitage, "The bacterial flagella motor," *Advances in Microbial Physiology*, vol. 41, 1999.

[49] B. L. Carroll and J. Liu, "Structural conservation and adaptation of the bacterial flagella motor," *Biomolecules*, vol. 10, no. 11, 2020.

[50] W. J. Zhang and L. F. Wu, "Flagella and swimming behavior of marine magnetotactic bacteria," *Biomolecules*, vol. 10, no. 3, 2020.

[51] M. Tian, Z. Wu, R. Zhang, and J. Yuan, "A new mode of swimming in singly flagellated Pseudomonas aeruginosa," *Proceedings of the National Academy of Sciences of the United States of America*, vol. 119, no. 14, 2022.

[52] C. Qian, C. Ching Wong, S. Swarup, and K. H. Chiama, "Bacterial tethering analysis reveals a "run-reverse-turn" mechanism for pseudomonas species motility," *Applied and Environmental Microbiology*, vol. 79, no. 15, 2013.

[53] M. Grognot, A. Mittal, M. Mah'moud, and K. M. Taute, "Vibrio cholerae Motility in Aquatic and Mucus-Mimicking Environments," *Applied and Environmental Microbiology*, vol. 87, no. 20, 2021.

[54] T. Pilizota, M. T. Brown, M. C. Leake, R. W. Branch, R. M. Berry, and J. P. Armitage, "A molecular brake, not a clutch, stops the Rhodobacter sphaeroides flagellar motor," *Proceedings of the National Academy of Sciences of the United States of America*, vol. 106, no. 28, 2009.

[55] G. Rosser, R. E. Baker, J. P. Armitage, and A. G. Fletcher, "Modelling and analysis of bacterial tracks suggest an active reorientation mechanism in Rhodobacter sphaeroides," *Journal of the Royal Society Interface*, vol. 11, no. 97, 2014.

[56] J. G. Mitchell, L. Pearson, S. Dillon, and K. Kantalis, "Natural assemblages of marine bacteria exhibiting high-speed motility and large accelerations," *Applied and Environmental Microbiology*, vol. 61, no. 12, 1995.

[57] G. M. Barbara and J. G. Mitchell, "Bacterial tracking of motile algae," *FEMS Microbiology Ecology*, vol. 44, no. 1, 2006.

[58] R. Stocker, "Reverse and flick: Hybrid locomotion in bacteria," *Proceedings of the National Academy of Sciences of the United States of America*, vol. 108, no. 7, 2011.

[59] M. Jabbarzadeh and H. C. Fu, "Dynamic instability in the hook-flagellum system that triggers bacterial flicks," *Physical Review E*, vol. 97, no. 1, 2018.

[60] J. Adler, "Chemotaxis in bacteria," *Journal of Supramolecular and Cellular Biochemistry*, vol. 4, no. 3, 1976.

[61] G. Arumugam and J. Tyagi, "Keller-Segel Chemotaxis Models: A Review," *Acta Applicandae Mathematicae*, vol. 171, no. 1, 2021.

[62] M. Grognot and K. M. Taute, "A multiscale 3D chemotaxis assay reveals bacterial navigation mechanisms," *Communications Biology*, vol. 4, no. 1, 2021.

[63] S. L. Porter, G. H. Wadhams, and J. P. Armitage, "Signal processing in complex chemotaxis pathways," *Nature Reviews Microbiology*, vol. 9, no. 3, 2011.

[64] A. Celani and M. Vergassola, "Bacterial strategies for chemotaxis response," *Proceedings of the National Academy of Sciences of the United States of America*, vol. 107, no. 4, 2010.

[65] B. L. Taylor, "How do bacteria find the optimal concentration of oxygen?," *Trends in Biochemical Sciences*, vol. 8, no. 12, 1983.

[66] M. Elmas, V. Alexiades, L. O'neal, and G. Alexandre, "Modeling aerotaxis band formation in Azospirillum brasilense," *BMC Microbiology*, vol. 19, no. 1, 2019.

[67] Y. Zhang, D. Wei, X. Wang, B. Wang, M. Li, H. Fang, Y. Peng, Q. Fan, and F. Ye, "Run-and-Tumble Dynamics and Mechanotaxis Discovered in Microglial Migration," *Research*, vol. 6, 2023.

[68] J. Arrieta, A. Barreira, M. Chioccioli, M. Polin, and I. Tuval, "Phototaxis beyond turning: Persistent accumulation and response acclimation of the microalga Chlamydomonas reinhardtii," *Scientific Reports*, vol. 7, no. 1, 2017.

[69] H. Shirai, C. Ito, and K. Tsukada, "pH-taxis drives aerobic bacteria in duodenum to migrate into the pancreas with tumors," *Scientific Reports*, vol. 12, no. 1, 2022.

[70] K. Ozasa, H. Kang, S. Song, S. Kato, T. Shinomura, and M. Maeda, "Temporal evolution of the gravitaxis of euglena gracilis from a single cell," *Plants*, vol. 10, no. 7, 2021.

[71] C. T. Lefèvre and D. A. Bazylinski, "Ecology, Diversity, and Evolution of Magnetotactic Bacteria," *Microbiology and Molecular Biology Reviews*, vol. 77, no. 3, 2013.

[72] M. Amor, V. Busigny, M. Durand-Dubief, M. Tharaud, G. Ona-Nguema, A. Gélabert, E. Alphandéry, N. Menguy, M. F. Benedetti, I. Chebbi, and F. Guyot, "Chemical signature of magnetotactic bacteria," *Proceedings of the National Academy of Sciences of the United States of America*, vol. 112, no. 6, 2015.

[73] D. A. Bazylinski and C. T. Lefèvre, "Magnetotactic bacteria from extreme environments," *Life*, vol. 3, no. 2, 2013.

[74] G. De Magistris and D. Marenduzzo, "An introduction to the physics of active matter," *Physica A: Statistical Mechanics and its Applications*, vol. 418, 2015.

[75] J. Hu, M. Yang, G. Gompper, and R. G. Winkler, "Modelling the mechanics and hydrodynamics of swimming E. coli," *Soft Matter*, vol. 11, no. 40, 2015.

[76] U. Danis, R. Rasooli, C. Y. Chen, O. Dur, M. Sitti, and K. Pekkan, "Thrust and hydrodynamic efficiency of the bundled flagella," *Micromachines*, vol. 10, no. 7, 2019.

[77] J. F. Staropoli and U. Alon, "Computerized analysis of chemotaxis at different stages of bacterial growth," *Biophysical Journal*, vol. 78, no. 1, 2000.

[78] V. A. Martinez, J. Schwarz-Linek, M. Reufer, L. G. Wilson, A. N. Morozov, and W. C. Poon, "Flagellated bacterial motility in polymer solutions," *Proceedings of the National Academy of Sciences of the United States of America*, vol. 111, no. 50, 2014.

[79] D. Saintillan, "Rheology of Active Fluids," *Annual Review of Fluid Mechanics*, vol. 50, no. 1, 2018.

[80] G. L. Miño, M. Baabour, R. Chertcoff, G. Gutkind, E. Clément, H. Auradou, and I. Ippolito, "E. coli Accumulation behind an Obstacle," *Advances in Microbiology*, vol. 08, no. 06, 2018.

[81] M. Lee, C. Lohrmann, K. Szuttor, H. Auradou, and C. Holm, "The influence of motility on bacterial accumulation in a microporous channel," *Soft Matter*, vol. 17, no. 4, 2021.

[82] J. Taktikos, H. Stark, and V. Zaburdaev, "How the motility pattern of bacteria affects their dispersal and chemotaxis," *PLoS ONE*, vol. 8, no. 12, 2013.

[83] M. Polin, I. Tuval, K. Drescher, J. P. Gollub, and R. E. Goldstein, "Chlamydomonas swims with two "gears" in a eukaryotic version of run-and-tumble locomotion," *Science*, vol. 325, no. 5939, 2009.

[84] W. Hu, G. Z. Lum, M. Mastrangeli, and M. Sitti, "Small-scale soft-bodied robot with multimodal locomotion," *Nature*, vol. 554, no. 7690, 2018.

[85] M. R. Shaebani, Z. Sadjadi, I. M. Sokolov, H. Rieger, and L. Santen, "Anomalous diffusion of self-propelled particles in directed random environments," *Physical Review E - Statistical, Nonlinear, and Soft Matter Physics*, vol. 90, no. 3, 2014.

[86] A. E. Hafner, L. Santen, H. Rieger, and M. R. Shaebani, "Run-and-pause dynamics of cytoskeletal motor proteins," *Scientific Reports*, vol. 6, 2016.

[87] G. Volpe and G. Volpe, "The topography of the environment alters the optimal search strategy for active particles," *Proceedings of the National Academy of Sciences of the United States of America*, vol. 114, no. 43, 2017.

[88] F. Ginot, A. Solon, Y. Kafri, C. Ybert, J. Tailleur, and C. Cottin-Bizonne, "Sedimentation of self-propelled Janus colloids: Polarization and pressure," *New Journal of Physics*, vol. 20, no. 11, 2018.

[89] J. Saragosti, P. Silberzan, and A. Buguin, "Modeling E. coli tumbles by rotational diffusion. implications for chemotaxis," *PLoS ONE*, vol. 7, no. 4, 2012.

[90] F. Detcheverry, "Generalized run-and-turn motions: From bacteria to Lévy walks," *Physical Review E*, vol. 96, no. 1, 2017.

[91] M. Theves, J. Taktikos, V. Zaburdaev, H. Stark, and C. Beta, "A bacterial swimmer with two alternating speeds of propagation," *Biophysical Journal*, vol. 105, no. 8, 2013.

[92] K. Malakar, V. Jemseena, A. Kundu, K. Vijay Kumar, S. Sabhapandit, S. N. Majumdar, S. Redner, and A. Dhar, "Steady state, relaxation and first-passage properties of a run-and-tumble particle in one-dimension," *Journal of Statistical Mechanics: Theory and Experiment*, vol. 2018, no. 4, 2018.

[93] F. Mori, P. Le Doussal, S. N. Majumdar, and G. Schehr, "Universal Survival Probability for a d-Dimensional Run-and-Tumble Particle," *Physical Review Letters*, vol. 124, no. 9, 2020.

[94] B. De Bruyne, S. N. Majumdar, and G. Schehr, "Survival probability of a run-and-tumble particle in the presence of a drift," *Journal of Statistical Mechanics: Theory and Experiment*, vol. 2021, no. 4, 2021.

[95] L. Angelani, R. Di Leonardo, and M. Paoluzzi, "First-passage time of run-and-tumble particles," *European Physical Journal E*, vol. 37, no. 7, 2014.

[96] P. Singh and A. Kundu, "Local time for run and tumble particle," *Physical Review E*, vol. 103, no. 4, 2021.

[97] D. Frydel, "Intuitive view of entropy production of ideal run-and-tumble particles," *Physical Review E*, vol. 105, no. 3, 2022.

[98] M. Guéneau, S. N. Majumdar, and G. Schehr, "Optimal mean first-passage time of a run-and-tumble particle in a class of one-dimensional confining potentials," *EPL*, vol. 145, no. 6, 2024.

[99] R. R. Bennett and R. Golestanian, "Emergent run-and-tumble behavior in a simple model of Chlamydomonas with intrinsic noise," *Physical Review Letters*, vol. 110, no. 14, 2013.

[100] H. Minagawa, Y. Nishikawa, I. Ikeda, K. Miyazaki, N. Takahara, Y. Sakamoto, T. Komai, and H. Nairta, "Characterization of sand sediment by pore size distribution and permeability using proton nuclear magnetic resonance measurement," *Journal of Geophysical Research: Solid Earth*, vol. 113, no. 7, 2008.

[101] A. Dathe, A. M. Tarquis, and E. Perrier, "Multifractal analysis of the pore- and solid-phases in binary two-dimensional images of natural porous structures," *Geoderma*, vol. 134, no. 3-4, 2006.

[102] L. Petrini and F. Migliavacca, "Biomedical Applications of Shape Memory Alloys," *Journal of Metallurgy*, vol. 2011, 2011.

[103] W. Dawid, "Biology and global distribution of myxobacteria in soils," *FEMS Microbiology Reviews*, vol. 24, no. 4, 2000.

[104] V. Tavakoli, "Microscopic Heterogeneity," in *SpringerBriefs in Petroleum Geoscience and Engineering*, Springer Nature, 2020.

[105] T. R. Ginn, B. D. Wood, K. E. Nelson, T. D. Scheibe, E. M. Murphy, and T. P. Clement, "Processes in microbial transport in the natural subsurface," *Advances in Water Resources*, vol. 25, no. 8-12, 2002.

[106] J. P. Celli, B. S. Turner, N. H. Afdhal, S. Keates, I. Ghiran, C. P. Kelly, R. H. Ewoldt, G. H. McKinley, P. So, S. Erramilli, and R. Bansil, "Helicobacter pylori moves through mucus by reducing mucin viscoelasticity," *Proceedings of the National Academy of Sciences of the United States of America*, vol. 106, no. 34, 2009.

[107] L. Zhang, B. Zhang, R. Liang, H. Ran, D. Zhu, J. Ren, L. Liu, A. Ma, and L. Cai, "A Dual-Biomineralized Yeast Micro-/Nanorobot with Self-Driving Penetration for Gastritis Therapy and Motility Recovery," *ACS Nano*, vol. 17, no. 7, 2023.

[108] Z. Sun, T. Wang, J. Wang, J. Xu, T. Shen, T. Zhang, B. Zhang, S. Gao, C. Zhao, M. Yang, F. Sheng, J. Yu, and Y. Hou, "Self-Propelled Janus Nanocatalytic Robots Guided by Magnetic Resonance Imaging for Enhanced Tumor Penetration and Therapy," *Journal of the American Chemical Society*, vol. 145, no. 20, 2023.

[109] H. H. Tuson and D. B. Weibel, "Bacteria-surface interactions," *Soft Matter*, vol. 9, no. 17, 2013.

[110] E. Lauga, W. R. DiLuzio, G. M. Whitesides, and H. A. Stone, "Swimming in circles: Motion of bacteria near solid boundaries," *Biophysical Journal*, vol. 90, no. 2, 2006.

[111] J. A. Geoghegan and Y. F. Dufrêne, "Mechanomicrobiology: How Mechanical Forces Activate Staphylococcus aureus Adhesion," *Trends in Microbiology*, vol. 26, no. 8, 2018.

[112] A. V. Singh, V. Kishore, G. Santomauro, O. Yasa, J. Bill, and M. Sitti, "Mechanical Coupling of Puller and Pusher Active Microswimmers Influences Motility," *Langmuir*, vol. 36, no. 19, 2020.

[113] M. Contino, E. Lushi, I. Tuval, V. Kantsler, and M. Polin, "Microalgae Scatter off Solid Surfaces by Hydrodynamic and Contact Forces," *Physical Review Letters*, vol. 115, no. 25, 2015.

[114] M. Souzy, A. Allard, J. F. Louf, M. Contino, I. Tuval, and M. Polin, "Microbial narrow-escape is facilitated by wall interactions," *Physical Review Research*, vol. 4, no. 2, 2022.

[115] D. Giacché, T. Ishikawa, and T. Yamaguchi, "Hydrodynamic entrapment of bacteria swimming near a solid surface," *Physical Review E - Statistical, Nonlinear, and Soft Matter Physics*, vol. 82, no. 5, 2010.

[116] D. Takagi, J. Palacci, A. B. Braunschweig, M. J. Shelley, and J. Zhang, "Hydrodynamic capture of microswimmers into sphere-bound orbits," *Soft Matter*, vol. 10, no. 11, 2014.

[117] O. Sipos, K. Nagy, R. Di Leonardo, and P. Galajda, "Hydrodynamic Trapping of Swimming Bacteria by Convex Walls," *Physical Review Letters*, vol. 114, no. 25, 2015.

[118] T. Jakuszeit and O. A. Croze, "Role of tumbling in bacterial scattering at convex obstacles," *Phys. Rev. E*, vol. 109, p. 044405, Apr 2024.

[119] E. Perez Ipiña, S. Otte, R. Pontier-Bres, D. Czerucka, and F. Peruani, "Bacteria display optimal transport near surfaces," *Nature Physics*, vol. 15, no. 6, 2019.

[120] D. Takagi, A. B. Braunschweig, J. Zhang, and M. J. Shelley, "Dispersion of self-propelled rods undergoing fluctuation-driven flips," *Physical Review Letters*, vol. 110, no. 3, 2013.

[121] E. Lauga and T. R. Powers, "The hydrodynamics of swimming microorganisms," *Reports on Progress in Physics*, vol. 72, no. 9, 2009.

[122] S. E. Spagnolie, G. R. Moreno-Flores, D. Bartolo, and E. Lauga, "Geometric capture and escape of a microswimmer colliding with an obstacle," *Soft Matter*, vol. 11, no. 17, 2015.

[123] E. Secchi, A. Vitale, G. L. Miño, V. Kantsler, L. Eberl, R. Rusconi, and R. Stocker, "The effect of flow on swimming bacteria controls the initial colonization of curved surfaces," *Nature Communications*, vol. 11, no. 1, 2020.

[124] R. Mok, J. Dunkel, and V. Kantsler, "Geometric control of bacterial surface accumulation," *Physical Review E*, vol. 99, no. 5, 2019.

[125] J. Elgeti and G. Gompper, "Wall accumulation of self-propelled spheres," *EPL*, vol. 101, no. 4, 2013.

[126] Z. Sadjadi and H. Rieger, "Topotaxis of active particles induced by spatially heterogeneous sliding along obstacles," *ArXiv*, 2023.

[127] T. Jakuszeit, O. A. Croze, and S. Bell, "Diffusion of active particles in a complex environment: Role of surface scattering," *Physical Review E*, vol. 99, no. 1, 2019.

[128] C. Lohrmann and C. Holm, "Optimal motility strategies for self-propelled agents to explore porous media," *Physical Review E*, vol. 108, Nov. 2023.

[129] P. Rizkallah, A. Sarracino, O. Bénichou, and P. Illien, "Microscopic Theory for the Diffusion of an Active Particle in a Crowded Environment," *Physical Review Letters*, vol. 128, no. 3, 2022.

[130] D. Saintillan, "Dispersion of run-and-tumble microswimmers through disordered media," *ArXiv*, 2023.

[131] H. H. Mattingly, "Bacterial diffusion in disordered media, by forgetting the media," *ArXiv*, 2023.

[132] A. Chamolly, T. Ishikawa, and E. Lauga, "Active particles in periodic lattices," *New Journal of Physics*, vol. 19, no. 11, 2017.

[133] T. Bhattacharjee and S. S. Datta, "Confinement and activity regulate bacterial motion in porous media," *Soft Matter*, vol. 15, no. 48, 2019.

[134] L. Angelani, "Confined run-and-tumble swimmers in one dimension," *Journal of Physics A: Mathematical and Theoretical*, vol. 50, no. 32, 2017.

[135] D. Frydel, "The run-and-tumble particle model with four-states: Exact solution at zero temperature," *Physics of Fluids*, vol. 34, no. 2, 2022.

[136] C. Roberts and G. Pruessner, "Exact solution of a boundary tumbling particle system in one dimension," *Physical Review Research*, vol. 4, no. 3, 2022.

[137] A. Duzgun and J. V. Selinger, "Active Brownian particles near straight or curved walls: Pressure and boundary layers," *Physical Review E*, vol. 97, no. 3, 2018.

[138] B. Ezhilan, R. Alonso-Matilla, and D. Saintillan, "On the distribution and swim pressure of run-and-tumble particles in confinement," *Journal of Fluid Mechanics*, vol. 781, 2015.

[139] A. Morin, D. Lopes Cardozo, V. Chikkadi, and D. Bartolo, "Diffusion, subdiffusion, and localization of active colloids in random post lattices," *Physical Review E*, vol. 96, no. 4, 2017.

[140] L. Shen and Z. Chen, "Critical review of the impact of tortuosity on diffusion," *Chemical Engineering Science*, vol. 62, no. 14, 2007.

[141] M. Binz, A. P. Lee, C. Edwards, and D. V. Nicolau, "Motility of bacteria in microfluidic structures," *Microelectronic Engineering*, vol. 87, no. 5-8, 2010.

[142] M. Zeitz, K. Wolff, and H. Stark, "Active Brownian particles moving in a random Lorentz gas," *European Physical Journal E*, vol. 40, no. 2, 2017.

[143] T. Pietrangeli, C. Ybert, C. Cottin-Bizonne, and F. Detcheverry, "Optimal run-and-tumble in slit-like confinement," *Physical Review Research*, vol. 6, p. 023028, Apr 2024.

[144] C. F. Lee, "Active particles under confinement: Aggregation at the wall and gradient formation inside a channel," *New Journal of Physics*, vol. 15, 2013.

[145] C. G. Wagner, M. F. Hagan, and A. Baskaran, "Steady states of active Brownian particles interacting with boundaries," *Journal of Statistical Mechanics: Theory and Experiment*, vol. 2022, no. 1, 2022.

[146] E. Q. Z. Moen, K. S. Olsen, J. Rønning, and L. Angheluta, "Trapping of active Brownian and run-and-tumble particles: A first-passage time approach," *Physical Review Research*, vol. 4, no. 4, 2022.

[147] V. A. Shaik, Z. Peng, J. F. Brady, and G. J. Elfring, "Confined active matter in external fields," *Soft Matter*, vol. 19, no. 7, 2023.

[148] L. Angelani, "Orthogonal run-and-tumble walks," *Journal of Statistical Mechanics: Theory and Experiment*, vol. 2022, no. 12, 2022.

[149] F. Cinque and E. Orsingher, "Stochastic Dynamics of Generalized Planar Random Motions with Orthogonal Directions," *Journal of Theoretical Probability*, vol. 36, no. 4, 2023.

[150] R. Mallikarjun and A. Pal, "Chiral run-and-tumble walker: Transport and optimizing search," *Physica A: Statistical Mechanics and its Applications*, vol. 622, 2023.

[151] S. Goldstein, "On diffusion by discontinuous movements, and on the telegraph equation," *Quarterly Journal of Mechanics and Applied Mathematics*, vol. 4, no. 2, 1951.

[152] M. Kac, "A stochastic model related to the telegrapher's equation," *Rocky Mountain Journal of Mathematics*, vol. 4, no. 3, 1974.

[153] G. H. Weiss, "Some applications of persistent random walks and the telegrapher's equation," *Physica A: Statistical Mechanics and its Applications*, vol. 311, no. 3-4, 2002.

[154] K. Gustafson and T. Abe, "The third boundary condition - Was it Robin's?," *Mathematical Intelligencer*, vol. 20, no. 1, 1998.

[155] M. Molaei, M. Barry, R. Stocker, and J. Sheng, "Failed escape: Solid surfaces prevent tumbling of Escherichia coli," *Physical Review Letters*, vol. 113, no. 6, 2014.

[156] Y. Kinosita, Y. Kikuchi, N. Mikami, D. Nakane, and T. Nishizaka, "Unforeseen swimming and gliding mode of an insect gut symbiont, Burkholderia sp. RPE64, with wrapping of the flagella around its cell body," *ISME Journal*, vol. 12, no. 3, 2018.

[157] M. J. Kühn, F. K. Schmidt, B. Eckhardt, and K. M. Thormann, "Bacteria exploit a polymorphic instability of the flagellar filament to escape from traps," *Proceedings of the National Academy of Sciences of the United States of America*, vol. 114, no. 24, 2017.

[158] K. Ishimoto, "Bacterial spinning top," *Journal of Fluid Mechanics*, vol. 880, 2019.

[159] F. Detcheverry, "Non-Poissonian run-and-turn motions," *EPL*, vol. 111, no. 6, 2015.

[160] C. Kurzthaler, Y. Zhao, N. Zhou, J. Schwarz-Linek, C. Devailly, J. Arlt, J. D. Huang, W. C. Poon, T. Franosch, J. Tailleur, and V. A. Martinez, "Characterization and Control of the Run-and-Tumble Dynamics of Escherichia Coli," *Physical Review Letters*, vol. 132, no. 3, 2024.

[161] A. F. Rosenthal, J. S. Griffin, M. Wagner, A. I. Packman, O. Balogun, and G. F. Wells, "Morphological analysis of pore size and connectivity in a thick mixed-culture biofilm," *Biotechnology and Bioengineering*, vol. 115, no. 9, 2018.

[162] N. R. Lang, S. Münster, C. Metzner, P. Krauss, S. Schürmann, J. Lange, K. E. Aifantis, O. Friedrich, and B. Fabry, "Estimating the 3D pore size distribution of biopolymer networks from directionally biased data," *Biophysical Journal*, vol. 105, no. 9, 2013.

[163] L. Bosgraaf and P. J. Van Haastert, "The Ordered Extension of Pseudopodia by Amoeboid Cells in the Absence of External Cues," *PLoS ONE*, vol. 4, no. 4, 2009.

[164] Z. Eidi, "Discrete Modeling of Amoeboid Locomotion and Chemotaxis in Dictyostelium discoideum by Tracking Pseudopodium Growth Direction," *Scientific Reports*, vol. 7, no. 1, 2017.

[165] A. A. Potdar, J. Jeon, A. M. Weaver, V. Quaranta, and P. T. Cummings, "Human mammary epithelial cells exhibit a bimodal correlated random walk pattern," *PLoS ONE*, vol. 5, no. 3, 2010.

[166] J. D'alessandro, A. P. Solon, Y. Hayakawa, C. Anjard, F. Detcheverry, J. P. Rieu, and C. Rivière, "Contact enhancement of locomotion in spreading cell colonies," *Nature Physics*, vol. 13, no. 10, 2017.

[167] G. Vizsnyiczai, G. Frangipane, S. Bianchi, F. Saglimbeni, D. Dell'Arciprete, and R. Di Leonardo, "A transition to stable one-dimensional swimming enhances E. coli motility through narrow channels," *Nature Communications*, vol. 11, no. 1, 2020.

[168] A. V. Chechkin, I. M. Zaid, M. A. Lomholt, I. M. Sokolov, and R. Metzler, "Bulk-mediated diffusion on a planar surface: Full solution," *Physical Review E - Statistical, Nonlinear, and Soft Matter Physics*, vol. 86, no. 4, 2012.

[169] A. Alexandre, M. Mangeat, T. Guérin, and D. S. Dean, "How Stickiness Can Speed Up Diffusion in Confined Systems," *Physical Review Letters*, vol. 128, no. 21, 2022.

[170] O. Bénichou, D. Grebenkov, P. Levitz, C. Loverdo, and R. Voituriez, "Optimal reaction time for surface-mediated diffusion," *Physical Review Letters*, vol. 105, no. 15, 2010.

[171] C. Jin and A. Sengupta, "Microbes in porous environments: from active interactions to emergent feedback," *Biophysical Reviews*, vol. 16, p. 173–188, Apr. 2024.

[172] M. Brun-Cosme-Bruny, A. Förtsch, W. Zimmermann, E. Bertin, P. Peyla, and S. Rafaï, "Deflection of phototactic microswimmers through obstacle arrays," *Physical Review Fluids*, vol. 5, no. 9, 2020.

[173] A. Dehkharghani, N. Waisbord, and J. S. Guasto, "Self-transport of swimming bacteria is impaired by porous microstructure," *Communications Physics*, vol. 6, no. 1, 2023.

[174] E. Irani, Z. Mokhtari, and A. Zippelius, "Dynamics of Bacteria Scanning a Porous Environment," *Physical Review Letters*, vol. 128, no. 14, 2022.

[175] J. N. Bardsley and A. Dubi, "Average transport path length in scattering media," *SIAM Journal on Applied Mathematics*, vol. 40, no. 1, 1981.

[176] S. Blanco and R. Fournier, "An invariance property of diffusive random walks," *Europhysics Letters*, vol. 61, no. 2, 2003.

[177] R. Artuso and D. J. Zamora, "Cauchy universality and random billiards," 2024.

[178] P. Shukla and D. Thongjaomayum, "Surprising variants of Cauchy's formula for mean chord length," *Phys. Rev. E*, vol. 100, no. 5, p. 050103(R), 2019.

[179] A. Santaló, *Introduction to integral geometry.* Hermann, 1953.

[180] N. Chernov, "Entropy, Lyapunov exponents, and mean free path for billiards," *J. Stat. Phys.*, vol. 88, pp. 1–29, July 1997.

[181] S. Torquato, *Random heterogeneous materials*. New York: Springer, 2002.

[182] A. Mazzolo, C. de Mulatier, and A. Zoia, "Cauchy's formulas for random walks in bounded domains," *J. Math. Phys.*, vol. 55, no. 8, p. 083308, 2014.

[183] M. Mangeat, T. Guérin, and D. S. Dean, "Effective diffusivity of Brownian particles in a two dimensional square lattice of hard disks," *J. Chem. Phys.*, vol. 152, no. 23, p. 234109, 2020.

[184] I. L. Novak, P. Kraikivski, and B. M. Slepchenko, "Diffusion in cytoplasm: Effects of excluded volume due to internal membranes and cytoskeletal structures," *Biophys. J.*, vol. 97, no. 3, pp. 758–767, 2009.

[185] I. L. Novak, F. Gao, P. Kraikivski, and B. M. Slepchenko, "Diffusion amid random overlapping obstacles: Similarities, invariants, approximations," *J. Chem. Phys.*, vol. 134, no. 15, p. 154104, 2011.

[186] R. Pierrat, P. Ambichl, S. Gigan, A. Haber, R. Carminati, and S. Rotter, "Invariance property of wave scattering through disordered media," *Proc. Natl. Acad. Sci. USA*, vol. 111, no. 50, pp. 17765–17770, 2014.

[187] R. Savo, R. Pierrat, U. Najar, R. Carminati, S. Rotter, and S. Gigan, "Observation of mean path length invariance in light-scattering media," *Science*, vol. 358, no. 6364, pp. 765–768, 2017.

[188] G. Frangipane, G. Vizsnyiczai, C. Maggi, R. Savo, A. Sciortino, S. Gigan, and R. Di Leonardo, "Invariance properties of bacterial random walks in complex structures," *Nat. Commun.*, vol. 10, no. 1, pp. 1–6, 2019.

[189] P. De Anna, A. A. Pahlavan, Y. Yawata, R. Stocker, and R. Juanes, "Chemotaxis under flow disorder shapes microbial dispersion in porous media," *Nat. Phys.*, vol. 17, pp. 68–73, Jan. 2021.

[190] C. T. Lefèvre, N. Viloria, M. L. Schmidt, M. Pósfai, R. B. Frankel, and D. A. Bazylinski, "Novel magnetite-producing magnetotactic bacteria belonging to the Gammaproteobacteria," *ISME Journal*, vol. 6, no. 2, 2012.

[191] X. Liu, Y. Zhang, Y. Wang, W. Zhu, G. Li, X. Ma, Y. Zhang, S. Chen, S. Tiwari, K. Shi, S. Zhang, H. M. Fan, Y. X. Zhao, and X. J. Liang, "Comprehensive understanding of magnetic hyperthermia for improving antitumor therapeutic efficacy," *Theranostics*, vol. 10, no. 8, 2020.

[192] Y. Park, Z. Eyal, P. Pekker, D. M. Chevrier, C. T. Lefèvre, P. Arnoux, J. Armengaud, C. L. Monteil, A. Gal, M. Pósfai, and D. Faivre, "Periplasmic Bacterial Biomineralization of Copper Sulfide Nanoparticles," *Advanced Science*, vol. 9, no. 28, 2022.

[193] D. Kuzajewska, A. Wszołek, W. Żwierełło, L. Kirczuk, and A. Maruszewska, "Magnetotactic bacteria and magnetosomes as smart drug delivery systems: A new weapon on the battlefield with cancer?," *Biology*, vol. 9, no. 5, 2020.

[194] Z. A. Nima, F. Watanabe, A. Jamshidi-Parsian, M. Sarimollaoglu, D. A. Nedosekin, M. Han, J. A. Watts, A. S. Biris, V. P. Zharov, and E. I. Galanzha, "Bioinspired magnetic nanoparticles as multimodal photoacoustic, photothermal and photomechanical contrast agents," *Scientific Reports*, vol. 9, no. 1, 2019.

[195] A. S. Mathuriya, "Magnetotactic bacteria for cancer therapy," *Biotechnology Letters*, vol. 37, no. 3, 2015.

[196] D. De Lanauze, O. Felfoul, J. P. Turcot, M. Mohammadi, and S. Martel, "Three-dimensional remote aggregation and steering of magnetotactic bacteria microrobots for drug delivery applications," *International Journal of Robotics Research*, vol. 33, no. 3, 2014.

[197] N. Mirkhani, M. G. Christiansen, and S. Schuerle, "Living, Self-Replicating Ferrofluids for Fluidic Transport," *Advanced Functional Materials*, vol. 30, no. 40, 2020.

[198] S. J. Kemp, R. M. Ferguson, A. P. Khandhar, and K. M. Krishnan, "Monodisperse magnetite nanoparticles with nearly ideal saturation magnetization," *RSC Advances*, vol. 6, no. 81, 2016.

[199] S. Klumpp and D. Faivre, "Magnetotactic bacteria: Magnetic navigation on the microscale," *European Physical Journal: Special Topics*, vol. 225, no. 11-12, 2016.

[200] N. Waisbord, C. T. Lefèvre, L. Bocquet, C. Ybert, and C. Cottin-Bizonne, "Destabilization of a flow focused suspension of magnetotactic bacteria," *Physical Review Fluids*, vol. 1, no. 5, 2016.

[201] C. J. Pierce, E. Mumper, E. E. Brown, J. T. Brangham, B. H. Lower, S. K. Lower, F. Y. Yang, and R. Sooryakumar, "Tuning bacterial hydrodynamics with magnetic fields," *Physical Review E*, vol. 95, no. 6, 2017.

[202] M. Birjukovs, K. Bente, D. Faivre, G. Kitenbergs, and A. Cebers, "Magnetic control of magnetotactic bacteria swarms," 2024.

[203] S. Rismani Yazdi, R. Nosrati, C. A. Stevens, D. Vogel, P. L. Davies, and C. Escobedo, "Magnetotaxis Enables Magnetotactic Bacteria to Navigate in Flow," *Small*, vol. 14, no. 5, 2018.

[204] S. Rismani Yazi, R. Nosrati, C. A. Stevens, D. Vogel, and C. Escobedo, "Migration of magnetotactic bacteria in porous media," *Biomicrofluidics*, vol. 12, no. 1, 2018.

[205] H. J. Buck, "Understanding inaction in confronting ecosystem collapse: Community perspectives from California's Salton Sea," *Ecology and Society*, vol. 25, no. 1, 2020.

[206] D. Trubitsyn, C. L. Monteil, C. Geurink, V. Morillo-Lopez, L. Gonzaga Paula de Almeida, A. T. Ribeiro de Vasconcelos, F. Abreu, D. A. Bazylinski, and C. T. Lefevre, "Complete Genome Sequence of Strain SS-5, a Magnetotactic Gammaproteobacterium Isolated from the Salton Sea, a Shallow, Saline, Endorheic Rift Lake Located on the San Andreas Fault in California," *Microbiology Resource Announcements*, vol. 10, no. 1, 2021.

[207] R. Nadkarni, S. Barkley, and C. Fradin, "A Comparison of Methods to Measure the Magnetic Moment of Magnetotactic Bacteria through Analysis of Their Trajectories in External Magnetic Fields," *PLoS ONE*, vol. 8, no. 12, pp. e82064 – 12, 2013.

[208] M. A. Islam, "Einstein-Smoluchowski diffusion equation: A discussion," *Physica Scripta*, vol. 70, no. 2-3, 2004.

[209] R. Nadkarni, S. Barkley, and C. Fradin, "A comparison of methods to measure the magnetic moment of magnetotactic bacteria through analysis of their trajectories in external magnetic fields," *PLoS ONE*, vol. 8, no. 12, 2013.

[210] E. Lauga, *The fluid dynamics of cell motility*. Cambridge University Press, 2020.

[211] G. Sinibaldi, V. Iebba, and M. Chinappi, "Swimming and rafting of E.coli microcolonies at air–liquid interfaces," *MicrobiologyOpen*, vol. 7, no. 1, 2018.

[212] K. Maeda, Y. Imae, J. I. Shioi, and F. Oosawa, "Effect of temperature on motility and chemotaxis of Escherichia coli," *Journal of Bacteriology*, vol. 127, no. 3, 1976.

[213] Y. Magariyama, M. Ichiba, K. Nakata, K. Baba, T. Ohtani, S. Kudo, and T. Goto, "Difference in bacterial motion between forward and backward swimming caused by the wall effect," *Biophysical Journal*, vol. 88, no. 5, 2005.

[214] S. Bianchi, F. Saglimbeni, and R. Di Leonardo, "Holographic imaging reveals the mechanism of wall entrapment in swimming bacteria," *Physical Review X*, vol. 7, no. 1, 2017.

[215] F. Saglimbeni, S. Bianchi, A. Lepore, and R. Di Leonardo, "Three-axis digital holographic microscopy for high speed volumetric imaging," *Optics Express*, vol. 22, no. 11, 2014.

[216] M. Rojas-Vega, P. d. Castro, and R. Soto, "Wetting dynamics by mixtures of fast and slow self-propelled particles," *ArXiv*, 01 2023.

[217] M. Rojas-Vega, P. d. Castro, and R. Soto, "Fast and slow self-propelled particles interacting with asymmetric obstacles: Wetting, segregation, rectification, and vorticity," *ArXiv*, 11 2021.

[218] S. K. Kumar, V. Ganesan, and R. A. Riggleman, "Perspective: Outstanding theoretical questions in polymer-nanoparticle hybrids," *J. Chem. Phys.*, vol. 147, no. 2, p. 020901, 2017.

[219] J. Jancar, J. Douglas, F. Starr, S. Kumar, P. Cassagnau, A. Lesser, S. Sternstein, and M. Buehler, "Current issues in research on structure–property relationships in polymer nanocomposites," *Polymer*, vol. 51, no. 15, pp. 3321–3343, 2010.

[220] Q. Zeng, A. Yu, and G. Lu, "Multiscale modeling and simulation of polymer nanocomposites," *Prog. Polym. Sci.*, vol. 33, no. 2, pp. 191–269, 2008.